



Universidade do Estado do Rio de Janeiro
Centro de Tecnologia e Ciências
Instituto Politécnico



Lucas Correia da Silva Jardim

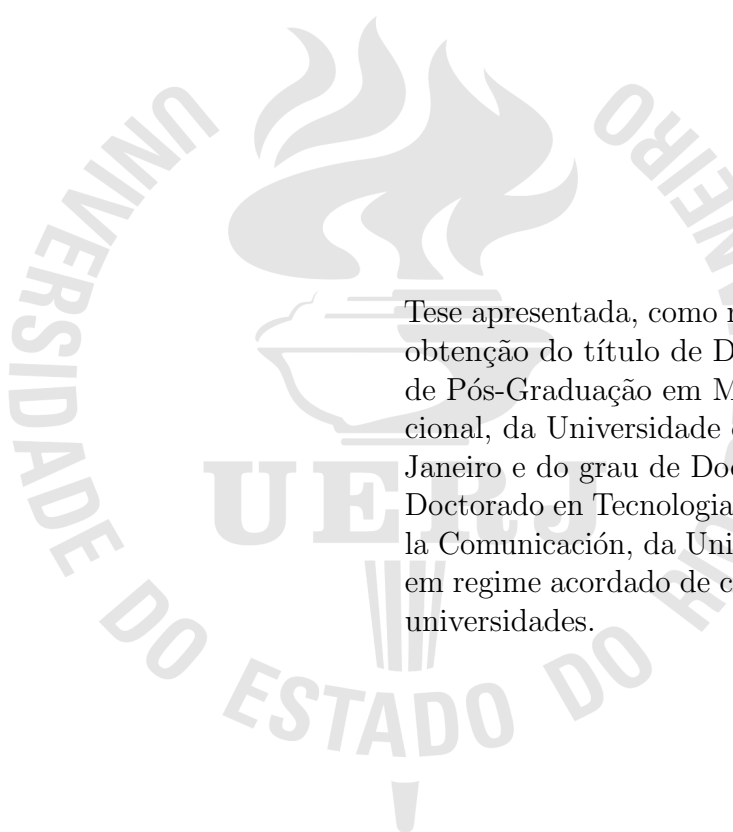
**Application of computational intelligence techniques in
optimization and inverse heat transfer problems**

Nova Friburgo

2023

Lucas Correia da Silva Jardim

**Application of computational intelligence techniques in optimization and
inverse heat transfer problems**



Tese apresentada, como requisito parcial para obtenção do título de Doutor, ao Programa de Pós-Graduação em Modelagem Computacional, da Universidade do Estado do Rio de Janeiro e do grau de Doctor do Programa de Doctorado en Tecnologías de la Información y la Comunicación, da Universidad de Granada em regime acordado de cotutela entre as duas universidades.

Orientadores: Prof. Dr. Antônio José da Silva Neto
Prof. Dr. Diego Campos Knupp
Prof. Dr. Carlos Alberto Cruz Corona

Nova Friburgo

2023

CATALOGAÇÃO NA FONTE
UERJ / REDE SIRIUS / BIBLIOTECA CTC/E

J37 Jardim, Lucas Correia da Silva.
Application of Computational Intelligence Techniques in
Optimization and Inverse Heat Transfer Problems / Lucas Correia da
Silva Jardim. - 2023.
154 f. : il.

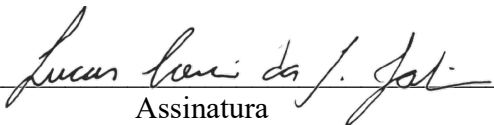
Orientador: Antônio José da Silva Neto.
Orientador: Diego Campos Knupp
Tese (doutorado) – Universidade do Estado do Rio de Janeiro,
Instituto Politécnico.

1. Problemas inversos (Equações diferenciais) – Teses. 2. Calor
- Transmissão – Teses. 3. Inteligência computacional – Teses. I.
Silva Neto, Antônio José da. II. Knupp, Diego Campos. III.
Universidade do Estado do Rio de Janeiro. Instituto Politécnico. IV.
Título.

CDU 517.972.7

Bibliotecária Pâmela Lisboa CRB7/ 5965

Autorizo, apenas para fins acadêmicos e científicos, a reprodução total ou parcial desta
dissertação, desde que citada a fonte.


Assinatura

26/09/2023
Data

Lucas Correia da Silva Jardim

**Application of Computational Intelligence Techniques in Optimization and
Inverse Heat Transfer Problems**

Tese apresentada, como requisito parcial para obtenção do título de Doutor, ao Programa de Pós-Graduação em Modelagem Computacional, da Universidade do Estado do Rio de Janeiro e do grau de Doctor do Programa de Doctorado en Tecnologías de la Información y la Comunicación, da Universidad de Granada em regime acordado de cotutela entre as duas universidades.

Aprovado em: 05 de julho de 2023

Banca Examinadora:

Prof. Dr. Antônio José da Silva Neto (Orientador)
Instituto Politécnico - UERJ

Prof. Dr. Diego Campos Knupp (Orientador)
Instituto Politécnico - UERJ

Prof. Dr.^a. Camila Martins Saporetti
Instituto Politécnico - UERJ

Prof. Dr. David Alejandro Pelta Mochcovsky
Universidad de Granada - UGR

Prof. Dr. Carlos Alberto Cruz Corona
Universidad de Granada - UGR

Prof. Dr. Davidson Martins Moreira
CIMATEC - SENAI

Nova Friburgo

2023

DEDICATION

To Danyelle, Alexandre, Jane, and Daniel.

ACKNOWLEDGEMENTS

First of all, I express my gratitude to my beloved wife Danyelle de Souza, my parents, Alexandre Jardim and Jane Correia, and my brother, Daniel Jardim, for their constant love and encouragement.

I am also grateful to my advisors from UERJ, Dr. Diego Campos Knupp, for the friendship, the confidence deposited in me, and the teachings since the very early stages of my academic career; and Antônio José da Silva Neto, Ph.D., for the friendship, innumerable professional advices, and the many doors opened that will forever positively impact my life.

To my UGR advisor, Dr. Carlos Cruz Corona, for the enormous help and attention given to me in my stay in Spain (twice), and the patience in advising this mechanical engineer with complex Computational Intelligence concepts.

To professors Dr. Luiz A. S. Abreu, Dr. Orestes Llanes-Santiago, Dr. Roberto P. Domingos, Dr. David A. Pelta, and Dr. Wagner F. Sacco, for the friendship, partnership and assistance in the tasks and ideas that make up this entire thesis. Without them, this work would simply not exist as herein presented.

To UGR professors, Dr. José Luis Verdegay Galdeano, Dr. María Teresa Lamata Jiménez, Marcelino Jose Cabrera Cuevas, Dr. Pavel Novoa Hernández, and everyone from the MODO investigation group, for the heartwarming welcome given in my 2022 Toledo/ES and Granada/ES stay.

To Sandra Guimarães, for the effort in making the cotutelle agreement a reality, and to Maria Marselle V. de Lemos, for the countless assistances with day-to-day administrative issues.

To my friends: Dr. Christian H. P. Beltrán, for the Mexican-Spanish lessons; Dr. Sergio A. B. Lins, for insisting in the use of Python; Dr. Bruno C. Lugão and Dr. Taciano M. S. M. Barros, for the shared knowledge in applied mathematics and inverse problems; Dr. Alexandre M. Barboza, for the friendship, from undergrad to doctorate.

I acknowledge the financial support provided by CAPES - Coordenação de Aperfeiçoamento de Pessoal de Nível Superior (Finance Code 001), CNPq - Conselho Nacional de Desenvolvimento Científico e Tecnológico, and FAPERJ - Fundação Carlos Chagas Filho de Amparo à Pesquisa do Estado do Rio de Janeiro.

I also acknowledge CAPES for the scholarship for my 2020 stay in the University

of Granada (Grant CAPES/PrInt No. 88887.469279/2019-00).

This thesis has been also partially funded by the projects PID2020-112754 GB-I00 (Spanish Ministry of Economy and Competitiveness and funds from the European Regional Development Fund, ERDF) and B-TIC-640-UGR20 (Regional Govern of Andalusia, Spain).

I would like to also acknowledge the financial support provided by FAPERJ - Fundação Carlos Chagas Filho de Amparo à Pesquisa do Estado do Rio de Janeiro, and CNPq - Conselho Nacional de Desenvolvimento Científico e Tecnológico.



Geometric patterns have always had a particular appeal for Muslim designers and craftsmen. They convey a certain aura of spirituality, or at least otherworldliness, without relating to any specific doctrine. In an Islamic context they are also quite free of any symbolic meaning. Above all they provide craftsmen with the opportunity to demonstrate his skill and subtlety of workmanship, and often to dazzle and intrigue with its sheer complexity.

Wichmann, B. and Wade, D. (1)

Geometric pattern photographed by the author, at the Alhambra palace - July 2020.

ABSTRACT

JARDIM, L. C. S. *Application of computational intelligence techniques in optimization and inverse heat transfer problems*. 2023. 170 f. Tese (Doutorado em Modelagem Computacional) - Programa de Pós-Graduação, em regime de associação da Universidade do Estado do Rio de Janeiro e da Universidad de Granada, Nova Friburgo, 2023.

Computational Intelligence can be defined as a collection of methods that solve problems by means of intelligence, reasoning, and tolerance to imprecision. In this thesis, Computational Intelligence techniques such as optimization metaheuristics, neural networks, fuzzy logic, and bayesian inference are applied to solve inverse heat transfer problems. To achieve this, five case studies with that aim are presented. The first study deals with the problem of identification of contact failures in the bonding of different materials. This is formulated as an Inverse Heat Conduction Problem and solved with an Artificial Neural Network. The second one employs the Fuzzy Levenberg-Marquardt method with Tikhonov Regularization in order to solve a combined conduction-radiation inverse problem. In the third, the performance of the Topographical Global Optimization algorithm is compared when initialized with two different point generators and finalized with two different local search methods for the solutions of inverse heat transfer problems. The fourth study presents a method to predict the optimal value of the Tikhonov's regularization parameter by solving simplified versions of the inverse problems considered, where tests are performed on three function estimation inverse heat transfer problems. In the fifth study, the formulation and solution of a bioheat transfer model of the brain containing a Deep Brain Stimulation (DBS) lead is presented and, furthermore, this solution is used for solving an inverse problem of determining the thermal and electrical conductivities of the brain tissue using measurements supposedly obtained with a sensor inside the DBS lead. In conclusion, this thesis shows the capabilities of various Computational Intelligence techniques in solving inverse heat transfer problems. The results presented contribute to two main categories: the field of inverse heat transfer, its applications in science and engineering; and the development of efficient computational procedures based on Computational Intelligence techniques.

Keywords: Inverse heat transfer problem. Computational intelligence. Optimization. Neural networks. Bayesian inference. Fuzzy logic.

RESUMO

JARDIM, L. C. S. *Aplicação de técnicas de inteligência computacional em problemas de otimização e inversos em transferência de calor*. 2023. 170 f. Tese (Doutorado em Modelagem Computacional) - Programa de Pós-Graduação, em regime de associação da Universidade do Estado do Rio de Janeiro e da Universidad de Granada, Nova Friburgo, 2023.

Inteligência Computacional pode ser definida como uma coleção de métodos que resolvem problemas por meio de inteligência, raciocínio e tolerância à imprecisão. Nesta tese, técnicas de Inteligência Computacional, como metaheurísticas de otimização, redes neurais, lógica fuzzy e inferência bayesiana são utilizadas para resolver problemas inversos de transferência de calor. Para isso, são apresentados cinco estudos de caso. O primeiro estudo trata do problema de identificação de falhas de contato na união de diferentes materiais. Isso é formulado como um Problema Inverso de Condução de Calor e resolvido com uma Rede Neural Artificial. O segundo emprega o método Fuzzy Levenberg-Marquardt com Regularização de Tikhonov para resolver um problema inverso combinado de condução-radiação. No terceiro, o desempenho do método Otimização Global Topográfica é comparado quando inicializado com dois geradores de pontos diferentes e finalizado com dois métodos de busca local diferentes para as soluções de problemas inversos de transferência de calor. O quarto estudo apresenta um método para prever o valor ótimo do parâmetro de regularização de Tikhonov, resolvendo versões reduzidas dos problemas inversos considerados, onde testes são realizados em três problemas inversos de estimativa de função. No quinto estudo, é apresentada a formulação e solução de um modelo de bio-transferência de calor do cérebro contendo um eletrodo de Estimulação Profunda do Cérebro (DBS) e, além disso, essa solução é usada para resolver um problema inverso de determinação das condutividades térmica e elétrica do tecido cerebral usando medidas supostamente obtidas com um sensor dentro do DBS. Concluindo, esta tese mostra as capacidades de diversas técnicas de Inteligência Computacional na resolução de problemas inversos de transferência de calor. Os resultados apresentados contribuem para duas principais áreas: o campo dos problemas inversos em transferência de calor, suas aplicações em ciência e engenharia; e o desenvolvimento de procedimentos computacionais eficientes baseados em técnicas de Inteligência Computacional.

Palavras-chave: Problema inverso em transferência de calor. Inteligência computacional. Otimização. Redes neurais. Inferência bayesiana. Lógica difusa.

RESUMEN

JARDIM, L. C. S. *Aplicación de técnicas de inteligencia computacional en problemas de optimización y inversos en transferencia de calor..* 2023. 170 f. Tese (Doutorado em Modelagem Computacional) - Programa de Pós-Graduação, em regime de associação da Universidade do Estado do Rio de Janeiro e da Universidad de Granada, Nova Friburgo, 2023.

La Inteligencia Computacional se puede definir como una colección de métodos que resuelven problemas mediante la inteligencia, el razonamiento y la tolerancia a la imprecisión. En esta tesis, se aplican técnicas de Inteligencia Computacional, como metaheurísticas de optimización, redes neuronales, lógica difusa e inferencia bayesiana, para resolver problemas inversos de transferencia de calor. Para esto, se presentan cinco estudios de caso con ese objetivo. El primer estudio se ocupa del problema de identificación de fallas de contacto en la unión de diferentes materiales. Esto se formula como un problema inverso de conducción de calor y se resuelve con una Red Neuronal Artificial. El segundo emplea el método difuso de Levenberg-Marquardt con regularización de Tikhonov para resolver un problema inverso combinado de conducción-radiación. En el tercero, se compara el rendimiento del algoritmo de optimización global topográfico cuando se inicializa con dos generadores de puntos diferentes y se finaliza con dos métodos de búsqueda local diferentes para las soluciones de problemas inversos de transferencia de calor. El cuarto estudio presenta un método para predecir el valor óptimo del parámetro de regularización de Tikhonov resolviendo versiones simplificadas de los problemas inversos considerados, donde se realizan pruebas en tres problemas inversos de estimación de funciones. En el quinto estudio, se presenta la formulación y solución de un modelo de transferencia de calor biológico del cerebro que contiene un electrodo de Estimulación Cerebral Profunda (DBS) y, además, esta solución se utiliza para resolver un problema inverso de determinación de las conductividades térmicas y eléctricas del tejido cerebral utilizando mediciones supuestamente obtenidas con un sensor dentro del electrodo DBS. En conclusión, esta tesis muestra las capacidades de varias técnicas de Inteligencia Computacional en la resolución de problemas inversos de transferencia de calor. Los resultados presentados contribuyen a dos categorías principales: el campo de la transferencia de calor inversa, sus aplicaciones en ciencia e ingeniería; y el desarrollo de procedimientos computacionales eficientes basados en técnicas de Inteligencia Computacional.

Palavras-chave: Problema inverso en transferencia de calor. Inteligencia computacional. Optimización. Inferencia bayesiana. Lógica difusa.

LIST OF FIGURES

Figure 1	Schematic representation of a direct problem.	25
Figure 2	Schematic representation of an inverse problem.	26
Figure 3	Schematic representation of Computational Intelligence concepts.....	27
Figure 4	Schematic representation of the multilayered medium.	33
Figure 5	Schematic representation of the Temperature Denoising Autoencoder....	36
Figure 6	Schematic representation of the Adhesive Layer Properties Autoencoder using the Auxiliary Function $\gamma(x)$	37
Figure 7	Schematic representation of the complete network model.....	38
Figure 8	T-AE output (a) and $\gamma(x)$ estimation (b) for one small contact failure configuration.....	49
Figure 9	T-AE output (a) and $\gamma(x)$ estimation (b) for one large contact failure configuration.....	50
Figure 10	T-AE output (a) and $\gamma(x)$ estimation (b) for two small contact failures configuration.....	51
Figure 11	T-AE output (a) and $\gamma(x)$ estimation (b) for one small and one large contact failures configuration.....	52
Figure 12	T-AE output (a) and $\gamma(x)$ estimation (b) for three small contact failures configuration.....	53
Figure 13	T-AE output (a) and $\gamma(x)$ estimation (b) for one large and two small contact failures configuration.....	54
Figure 14	Schematic representation of the medium subjected to the coupled conduction-radiation heat transfer phenomenon (2, 3).	60
Figure 15	Memberships of the fuzzy system input PE.	67
Figure 16	Memberships of the fuzzy system output λ	67
Figure 17	Complete PE input vs. λ output of the fuzzy system.	69
Figure 18	Comparison among values of the Radiation Intensity, Temperature, and their experimental data obtained for Exec. #5 (Case 2A).....	73
Figure 19	Comparison of estimated ω for (a) Exec. #5 and (b) Exec #4.....	74

Figure 20	Comparison among values of the Radiation Intensity, Temperature, and their experimental data obtained for Exec. #5 (Case 2B).....	75
Figure 21	Comparison of estimated ω for (a) Exec. #5 and (b) Exec #1.....	75
Figure 22	Comparison among values of the Radiation Intensity, Temperature, and their experimental data obtained for Exec. #5 (Case 2C).....	77
Figure 23	Comparison of estimated ω for (a) Exec. #5 and (b) Exec #1.....	77
Figure 24	Example of 400 points with MT and SS.....	83
Figure 25	Schematic representation of the medium subjected to the coupled conduction-radiation heat transfer phenomena (2, 3).	91
Figure 26	Schematic representation of the system plate-resistance-plate. (4).....	93
Figure 27	Schematic representation of the parallel plates system showing the height dependence of the fluid velocity with the transversal coordinate.	95
Figure 28	Exact solution and experimental data for DP-1, obtained with $N = 0.05$, $\omega = 0.3$, $\tau_0 = 1.0$ and $\sigma_1 = 0.01$	99
Figure 29	Exact solution and experimental data for the temperature in DP-2, obtained with $k = 0.22$ W/mK, $c_p = 1680$ J/kgK and $\sigma_2 = 0.5$ °C.....	101
Figure 30	Exact solution and experimental data for the temperature in DP-3, obtained with the inlet temperature profile (a) and $\sigma_3 = 0.5$ °C.	102
Figure 31	Comparison of solutions obtained with $H = 100$ and $K = 10$ configuration for IP-1 and the respective simulated experimental data.	106
Figure 32	Comparison of solutions obtained with $H = 100$ and $K = 10$ configuration for IP-2 and the respective simulated experimental data.	108
Figure 33	Comparison of solutions obtained with $H = 100$ and $K = 5$ configuration for IP-3 and the respective simulated experimental data.....	110
Figure 34	Schematic representation of the heterogenous biological tissue.	121
Figure 35	Schematic representation of the two parallel plates channel showing the transversal coordinate spatially dependent fluid velocity.	122
Figure 36	Schematic representation of a radiative transfer participating medium. Here Y represents the exit radiation intensity at both boundaries of the medium.	123

Figure 37	Evolution of the sequence R_i for the low dimension model with $n = 7$ showing the divergent sequence for $\sqrt{\phi} = 1.0$, and the convergent sequence of the found $\sqrt{\phi} = 0.7595$	126
Figure 38	Solutions for IP-1 with the low dimension model (a) that generated the estimative for the regularization parameter of the high dimension model (b).....	127
Figure 39	Simulated experimental data and temperature profile obtained with the solution of IP-1 with $n = 21$	128
Figure 40	Evolution of the solution obtained for different values of λ as the FP series converges.....	130
Figure 41	Simulated experimental data and temperature profile obtained with the solution of IP-2 with $n = 21$	131
Figure 42	Solutions for IP-3: (a) low dimension model with $n = 7$, and (b) the high dimension model with $n = 21$, obtained with the estimated value for λ_{high}	132
Figure 43	Evolution of the sequence R_i for the low dimension model with $n = 7$ showing the divergent sequence of $\sqrt{\phi} = 1.0$ (solid dots), and the convergent sequence of the found value $\sqrt{\phi} = 0.8988$ (solid triangles)	132
Figure 44	Simulated experimental data and radiation intensity profile obtained with the solution of IP-3 with $n = 21$	133
Figure 45	Representation of the DBS system with detail on the lead inside the brain.	134
Figure 46	Schematic representation of Medtronic's Model 3389 and Model 3387 showing the geometrical configuration of the electrodes.....	136
Figure 47	Schematic representation of the computational axisymmetric domain. ...	137
Figure 48	Solution of both the temperature and the electrical problem for Model 3389 with activity on electrodes 1 and 4.	141
Figure 49	Experimental data along with exact solution for Model 3389 with activity on electrodes 1 and 4 for two noise levels: $\epsilon = 0.025$ °C and $\epsilon = 0.05$ °C in Eq. 6.7, respectively.....	142

LIST OF TABLES

Table 1	Thermal Properties for the Multilayered Medium	39
Table 2	Time Instants and number of temperature data used.	41
Table 3	Temperature Autoencoder (T-AE) MSE results for 3 time instants and different Autoencoder (AE) dimensions	42
Table 4	T-AE MSE results for 5 time instants and different AE dimensions	43
Table 5	T-AE MSE results for 7 time instants and different AE dimensions	43
Table 6	MSE for $M = 3$, 80-dim AE, and different MLP sizes	46
Table 7	MSE for $M = 5$, 160-dim AE, and different MLP sizes	46
Table 8	MSE for $M = 7$, 120-dim AE, and different MLP sizes	46
Table 9	Summary of the parameters to simulate the experimental data set	70
Table 10	Results for Test Case 1	72
Table 11	Results for Test Case 2A	73
Table 12	Results for Test Case 2b.....	75
Table 13	Results for Test Case 2c.....	76
Table 14	Exact values of the parameters for DP-1 and IP-1.	99
Table 15	Exact values of the parameters of DP-2 and IP-2.	100
Table 16	Exact values of the parameters of DP-3 and IP-3.	101
Table 17	Search intervals and exact values for IP-1, IP-2 and IP-3	104
Table 18	Average results for 10 independent executions of IP-1 with comparisons of Sobol Sequence (SS), Mersenne Twister (MT), Levenberg-Marquardt (LM) and Nelder-Mead (NM).	105
Table 19	Average results for 50 independent executions of IP-2 with comparisons of Sobol Sequence (SS), Mersenne Twister (MT), Levenberg-Marquardt (LM) and Nelder-Mead (NM).	107
Table 20	Average results for 30 independent executions of IP-3 with comparisons of Sobol Sequence (SS), Mersenne Twister (MT), Levenberg-Marquardt (LM) and Nelder-Mead (NM).	109
Table 21	Critical values T_w for the Wilcoxon Signed-Rank Test.	110
Table 22	Wilcoxon Signed Rank Test for IP-1	111

Table 23	Wilcoxon Signed Rank Test for IP-2	112
Table 24	Wilcoxon Signed Rank Test for IP-3	112
Table 25	Exact values of the parameters for the Direct Problem 1 (DP-1).	126
Table 26	Results obtained for several values for the low dimension model λ , and their respective λ_{high} estimates for IP-2.	129
Table 27	Exact values of the parameters of the direct problem.	140
Table 28	Results obtained using DBS lead Model 3389 with electrode pair 1-2 active and experimental noise levels of $\epsilon = 0.025$ °C and $\epsilon = 0.050$ °C ...	144
Table 29	Results obtained using DBS lead Model 3389 with electrode pair 1-4 active and experimental noise levels of $\epsilon = 0.025$ °C and $\epsilon = 0.050$ °C. ..	145
Table 30	Results obtained using DBS lead Model 3387 with electrode pair 1-2 active and experimental noise levels of $\epsilon = 0.025$ °C and $\epsilon = 0.050$ °C. ..	146
Table 31	Results obtained using DBS lead Model 3387 with electrode pair 1-4 active and experimental noise levels of $\epsilon = 0.025$ °C and $\epsilon = 0.050$ °C. ..	147

CONTENTS

	INTRODUCTION	19
1	THEORETICAL BACKGROUND	25
1.1	Direct and inverse heat transfer problems	25
1.2	Computational Intelligence concepts	26
1.2.1	<u>Neural Networks</u>	27
1.2.2	<u>Fuzzy Logic</u>	28
1.2.3	<u>Metaheuristics for optimization</u>	28
1.2.4	<u>Probabilistic Models - Bayesian Inference</u>	29
2	CONTACT FAILURE IDENTIFICATION IN MULTILAYERED MEDIUM VIA SINGLE DOMAIN FORMULATION AND AR- TIFICIAL NEURAL NETWORKS	30
2.1	Introduction and background	30
2.2	Direct Problem Formulation and Solution	32
2.3	Inverse Problem Formulation	34
2.4	Inverse Problem Solution with Artificial Neural Networks	35
2.4.1	<u>Autoencoders</u>	35
2.4.2	<u>Final Artificial Neural Network Model</u>	37
2.4.3	<u>General Aspects of the Artificial Neural Network</u>	38
2.5	Results and discussion	39
2.5.1	<u>Direct Problem Solution</u>	39
2.5.2	<u>Training, Validation and Testing Sets Generation</u>	40
2.5.3	<u>Temperature Autoencoder Results</u>	41
2.5.4	<u>MLP Results</u>	43
2.5.5	<u>Detection of Contact Failures</u>	47
2.6	Conclusions	55

3	FUZZY LEVENBERG-MARQUARDT DAMPING FACTOR UPDATE STRATEGY AND TIKHONOV REGULARIZATION APPLIED TO A COUPLED CONDUCTION-RADIATION INVERSE HEAT TRANSFER PROBLEM	57
3.1	Introduction	57
3.2	Direct problem formulation and solution	59
3.3	Inverse problem formulation and solution	62
3.3.1	<u>Classical Levenberg-Marquardt with Tikhonov Regularization</u>	64
3.3.2	<u>Fuzzy Levenberg-Marquardt</u>	65
3.4	Results and discussion	68
3.4.1	<u>Test Case 1</u>	70
3.4.2	<u>Test Case 2</u>	71
3.5	Conclusions	78
4	PERFORMANCE ANALYSIS OF THE TOPOGRAPHICAL GLOBAL OPTIMIZATION IN INVERSE HEAT TRANSFER PROBLEMS	79
4.1	Introduction and background	79
4.2	The Topographical Global Optimization (TGO)	81
4.2.1	<u>Step 1: Search space sampling</u>	82
4.2.2	<u>Step 2: Construction of the topography</u>	82
4.2.3	<u>Step 3: Local search</u>	86
4.3	Formulation and solution of the Heat Transfer Problems	90
4.3.1	<u>Direct Problem 1 (DP-1): Heat transfer by simultaneous conduction and radiation in a semi-transparent medium</u>	90
4.3.2	<u>Direct Problem 2 (DP-2): Heat conduction in a thermally thin plate</u>	92
4.3.3	<u>Direct Problem 3 (DP-3): Heat transfer in a thermally developing fluid flow inside parallel plates</u>	94
4.4	Inverse Problems Formulation	95
4.4.1	<u>Inverse Problem 1 (IP-1):</u>	96
4.4.2	<u>Inverse Problem 2 (IP-2):</u>	97
4.4.3	<u>Inverse Problem 3 (IP-3):</u>	97
4.5	Results and discussion	98

4.5.1	<u>Direct problems solutions and experimental data</u>	98
4.5.2	<u>Computational Experiments</u>	102
4.5.3	<u>Wilcoxon signed ranks test</u>	109
4.6	Conclusions	112
5	COMPUTATIONAL INTELLIGENCE AND TIKHONOV REGULARIZATION WITH REDUCED DIMENSION MODEL: APPLICATIONS IN HEALTH, RENEWABLE ENERGY AND CLIMATE HEAT TRANSFER INVERSE PROBLEMS	114
5.1	Introduction	114
5.2	Fixed Point Iteration method with reduced model	116
5.2.1	<u>The Fixed Point Iteration method (FP)</u>	117
5.2.2	<u>The Reduced Dimension Model approach</u>	118
5.3	Direct Problems	119
5.3.1	<u>Direct Problem 1: Spatially varying thermal conductivity of a biological tissue</u>	120
5.3.2	<u>Direct Problem 2: Inlet temperature profile in a parallel plates channel</u>	120
5.3.3	<u>Direct Problem 3: Radiative transfer with variable space dependent scattering albedo</u>	122
5.4	Inverse Problems	123
5.5	Results and Discussion	124
5.5.1	<u>Results for the Inverse Problem 1 (IP-1)</u>	125
5.5.2	<u>Results for the Inverse Problem 2 (IP-2)</u>	127
5.5.3	<u>Results for the Inverse Problem 3 (IP-3)</u>	129
5.6	Conclusions	131
6	BRAIN THERMAL AND ELECTRICAL PROPERTIES ESTIMATION USING EXPERIMENTAL DATA FROM DEEP BRAIN STIMULATION LEAD	134
6.1	Introduction	134
6.2	Formulation and solution of the dbs heating problem	135
6.3	Inverse problem formulation and solution	137
6.4	Results and discussion	139
6.4.1	<u>Direct problem solution and results</u>	139

6.4.2	<u>Inverse problem solution and results</u>	140
6.5	Conclusions	148
	FINAL CONSIDERATIONS	149
	CONSIDERAÇÕES FINAIS	151
	CONSIDERACIONES FINALES	153
	REFERENCES	155
	APPENDIX - Works produced from this thesis	169

INTRODUCTION

Motivation

Heat transfer is a fundamental mechanism of energy diffusion in several engineering systems. This mechanism has already been studied for decades and has a strong theoretical basis today. It represents a body of knowledge largely considered in the process of manufacturing, design of equipment, cost effective operations in industries and even in biotechnology, just to name a few.

The physical phenomena involved in heat transfer problems can be analyzed directly or inversely. That is, when all causes and conditions are known, the temperature field in the domain considered can be obtained by solving the mathematical model. This is the so called direct analysis. On the other hand, when some conditions or properties of the medium are unknown, such as thermophysical properties, boundary and initial conditions, but experimental temperature data are available, it is possible to obtain estimates of these unknown parameters and conditions through the formulation and solution of an inverse problem (5, 6).

To obtain the solution of direct problems, many numerical and hybrid techniques have emerged along the years, such as finite differences (7), finite elements (8), finite volumes (9), hybrid integral transforms (10) and so on. On the other hand, obtaining the solution of inverse heat transfer problems can present an increased computational challenging due to some inherent complexities of this class of problems. One of the primary challenges stems from the requirement of a high number of evaluations of the direct model, rendering the problem computationally intensive. Additionally, inverse heat transfer problems are often ill-posed, meaning that the solution may not be unique and stable. To address this issue, regularization techniques are employed to introduce constraints and stabilize the solution. Among many others, the techniques used to solve inverse problems have also evolved throughout the last 60 decades, highlighting the advancements in stochastic optimization methods, bayesian inference techniques, monte carlo simulations, and others. In this context, a particular group of techniques known as Computational Intelligence has been increasingly used in science and engineering.

The most common used definition of Computational Intelligence is described by

Zadeh in 1994 (11), which states that the main objective of such group of techniques is to explore the tolerance for imprecision and uncertainty of a given problem in order to obtain low cost solutions within reasonable feasibility. Aligned with Zadeh, Verdegay et al. (12) described this field as a family of problem-resolution techniques and methods guided by the idea that real situations can be dealt as the same way as human beings deal with them, i.e., “on the basis of intelligence, common sense, consideration of analogies, approaches, etc”.

Another definition of Computational Intelligence is given by Li et al. in 1998 (13), which states the following: “Every computing process that purposely includes imprecision into the calculation on one or more levels and allows this imprecision either to change (decrease) the granularity of the problem, or to “soften” the goal of optimisation at some stage, is defined as to belonging to the field of Computational Intelligence.”.

As it is possible to see, the definition of Computational Intelligence is not crisply determined. Nevertheless, many commonalities can be found in the definitions given by different authors over time, such as: The ability to treat, include, and deal with errors; The criterium for what is the “best solution” may be intelligently loose; The feasibility, tractability, and efficiency in the process of obtaining this solution as an objective of the approach itself.

Objectives

Main objectives

With those concepts in mind, the main objective of this work is to use Computational Intelligence concepts such as fuzzy logic, optimization metaheuristics, neural networks and bayesian inference in order to find computational efficient solutions for heat transfer problems, aiming at the solution of optimization and inverse problems, which often require computationally intensive iterative procedures.

To do this, a collection of case studies are presented. These studies involve the development of new techniques as well as the use of methods never before tested in inverse heat transfer problems. Each one of these studies are briefly described in the following subsection, where each specific objective is presented, along with a short motivation and highlights of the results obtained.

Specific objectives

Artificial Neural Networks. In this case study, the estimation of defects positioning occurring in the interface between two materials is performed by using an Artificial Neural Network modeled as an Inverse Heat Conduction Problem. Identifying contact failures in the bonding process of two materials is crucial in many engineering applications, ranging from manufacturing, preventive inspection and even failure diagnosis. This can be modeled as an Inverse Heat Conduction Problem in Multilayered media, where thermography temperature measurements from an exposed surface of the media are available. This study solves this inverse problem with an Artificial Neural Network that receives these experimental data as input and outputs the thermalphysical properties of the adhesive layer, where defects can occur. An Autoencoder is used to reduce the dimension of the transient 1D thermography data, where its latent space represents the experimental data in a lower dimension, then these reduced data is used as input to a fully connected multilayer perceptron network. Results indicate that this is a promising approach due to the good accuracy and low computational cost observed. In addition, by including different noise levels within a defined range in the training process, the ANN can generalize the experimental data input and estimate the positioning of defects with similar quality.

Fuzzy Logic. The recently proposed Fuzzy Levenberg-Marquardt Damping Factor Updating Strategy (FLM) is used along with Tikhonov Regularization (TR) in order to solve a coupled conduction-radiation function estimation inverse problem. FLM consists of updating the Levenberg-Marquardt (LM) damping factor with the assist of Fuzzy Logic. To test the FLM algorithm combined with TR, a conduction-radiation problem is addressed, and it serves as test bed to the numerical experiments, where the objective is to obtain estimatives of parameters, such as the spatially variable scattering albedo, the thermal conductivity and the optical thickness, simultaneously, which is often performed separately. Two main test cases are presented in this investigation, one considering only the radiation problem, used as benchmark, in order to investigate noise levels and hyperparameters. The second main test case deals with the coupled conduction-radiation heat transfer problem for different functional forms of the spatially variable scattering albedo. For all presented numerical experiments, good estimates were achieved for the sought functions and parameters. These results demonstrate that the methodology presented, through

the combination of the Fuzzy LM damping factor updating strategy and the Tikhonov regularization scheme, may provide valuable tools for inverse heat transfer problems.

Metaheuristics for Optimization I. In this investigation, the performance of the Topographical Global Optimization (TGO) method is compared when initialized with two different point generators and finalized with two different local search methods. Three inverse heat transfer problems are the testbed for this comparison, where the number of function evaluations necessary to reach a certain goal is the criterion used. In this context, the main objective of this study is to address which combination is the most efficient. To initialize TGO, points must be distributed in a search space, so we compared the pseudo-random routine Mersenne Twister against the quasi-random Sobol Sequence. Then, from these distributed points, TGO selects topographical minima to start a local search, performed here with the Nelder-Mead and the Levenberg-Marquadt methods. Therefore, four different combinations of TGO are tested, and the Wilcoxon Test is performed for a more reliable and insightful comparison among them.

Metaheuristics for Optimization II. This case study presents a method to predict the optimal value of the Tikhonov's regularization parameter by solving simplified versions of the inverse problems considered. This can be of great benefit since methods such as the L-curve and the Fixed Point Iteration require the inverse problem to be solved several times in order to determine the optimal value for the regularization parameter. The main idea that supports the proposed approach is to solve the problem of interest using a low set of dimensions to represent the function to be estimated and, then, this solution is used to obtain an estimate for the regularization parameter of the complete model, based on the Fixed Point Iteration method. Tests are performed on three inverse heat transfer problems: estimation of the variable thermal conductivity of a biological tissue, estimation of the inlet temperature in parallel plates channel, and the estimation of the variable scattering albedo of a radiative transfer participating medium. The results obtained demonstrate the feasibility of the technic in three problems with potential practical applications in bioengineering, renewable energy and climate in alignment with the Sustainable Development Goals (SDG) 3, 4, 7, 9, 13, and 17 of the United Nations 2030 Agenda established in 2015.

Bayesian Inference. The case study reported here intends to formulate and solve a bioheat transfer model of the brain containing a Deep Brain Stimulation (DBS) lead and,

furthermore, to use this solution for solving an inverse problem of determining the thermal and electrical conductivities of the brain tissue using measurements supposedly obtained with a sensor inside the DBS lead. Deep Brain Stimulation (DBS) is a well-established neurosurgery that alleviates the symptoms of several movement disorders and other brain related conditions. It works by placing a small lead containing electrodes inside the patient's brain and using them to electrically stimulate that area. Although this procedure is very common, little is known about its physiological effects on the brain and, on top of that, injuries caused from burning have been reported. The results revealed that it is possible to estimate the both parameters especially when the measurements uncertainties are relatively small.

Text organization

Initially, Chapter 1 presents a theoretical background related to themes of this thesis, containing a brief description of direct problems, inverse problems, and Computational Intelligence concepts.

The five case studies described in the previous subsection are presented as individual Chapters in this thesis. Therefore, from Chapter 2 to 6, a work containing its own introduction, methodology, results, and conclusions is presented.

Chapter 2 presents the estimation of defects positioning occurring in the interface between two materials. In Chapter 3, the Fuzzy Levenberg-Marquardt is used to solve a combined conduction-radiation problem. In Chapter 4, the Topographical Global Optimization method is tested with three inverse heat transfer problems. Chapter 5 presents a technique to efficiently predict the optimal Tikhonov parameter with tests in three also inverse heat transfer problems. Chapter 6 shows the formulation and solution of a inverse bioheat transfer problem, where a Deep Brain Stimulation electrical heating is studied.

Finally, conclusions and overall considerations are made in the last Chapter, where some suggestions for future works are also presented. These final considerations are pertinent to the thesis as a whole. The conclusions for the individual case studies are presented in each respective Chapter.

Figures, tables and algorithms are numbered sequentially in the whole text, whereas equations are numbered specifically within each Chapter, *e.g.*, the third equation of

the fifth Chapter is Equation 5.3. Moreover, variables, symbols and acronyms are used independently in each chapter. Even knowing that terms such as thermal conductivity k , temperature T , and many others, appear to have the same meaning, it is important to consider them individually in each one of the chapters.

It is important to highlight another text organization aspect. As the reader progresses through the text, it is possible notice that each case studies presented can be briefly classified into two main categories:

- Chapters 3, 4 and 5: testing and development of efficient methods based on computational intelligence, where the focus is on performing tests, comparisons and improvements to computational methods;
- Chapters 2 and 6: development and enhancement of heat transfer scientific and engineering applications.

This classification intends to loosely separate in subgroups the contributions and advancements provided by this thesis.

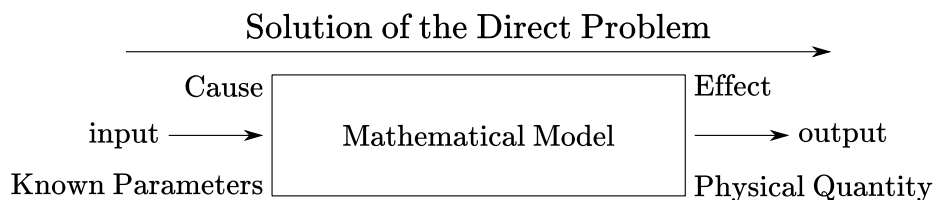
1 THEORETICAL BACKGROUND

1.1 Direct and inverse heat transfer problems

There are three different modes of heat transfer: conduction, convection and radiation. In conduction, the atomic and molecular activities of a medium is the source of energy transfer. Higher temperatures are associated with higher molecular energies. This energy is transferred from one molecule to its neighborhood via collisions and magnetic forces and, in this scenario, a transfer of energy must occur from the more energetic molecules to the less energetic ones. In convection, transfer takes place between a surface and a fluid in motion, when both are at different temperatures. The last mode of heat transfer is thermal radiation: energy emitted by matter at a temperature other than absolute zero. This energy is carried by electromagnetic waves and, unlike conduction and convection, it does not need a material medium to propagate (14).

When parameters of a medium of interest and its initial and boundary conditions are known and, in addition, a mathematical model describing the system considering the different forms of heat transfer or a combination of them is available, then it is possible to determine the temperature field of this medium for a given time or position. This kind of analysis is called a direct problem, where parameters and conditions are the input of a model and the output is the physical quantity of interest, *e.g.*, temperature, pressure, radiation intensity, and so on. Figure 1 presents a schematic representation of a direct problem. In this type of problem, the cause is known and its leads to the effect of the problem by the solution of the mathematical model (5).

Figure 1 – Schematic representation of a direct problem.

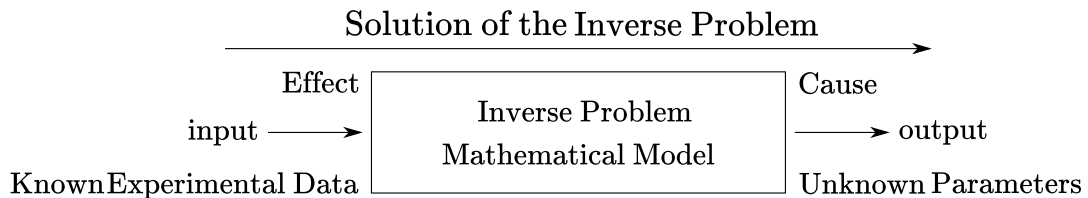


Source: The author, 2023.

Inverse problems involve estimating the cause from knowledge of the effect. If some properties of a material – or parameters of a model in general – are unknown, but experimental data of the response of this model are available, then the unknown parameters

can be estimated through the formulation and solution of an inverse problem (5, 6, 15). In Figure 2 a schematic representation of inverse problems is presented. In this kind of problem, the input (known information) is the experimental data of the physical quantity of interest, such as pressure, temperature, etc.

Figure 2 – Schematic representation of an inverse problem.



Source: The author, 2023.

They can be formulated explicitly or implicitly. In inverse problems with explicit formulation, the unknown parameters are estimated through a completely determined expression. One example of such approach can be found in the work of Knupp and Abreu (16), where they obtained a completely determined expression that yielded the sought thermal flux. Nevertheless, it is not always possible to mathematically manipulate the expressions in order to obtain the explicit solution, in fact, this can be considered rare in problems dealing with partial differential equations. On the other hand, implicit formulations are the most common approach and they can consider prior information (*priori*) or not. For example, in the Bayesian approach, an attempt is made to use all the information that is previously available for the unknown parameters and experimental data, thus leading to a better evaluation of the estimated parameters uncertainty. However, due to this need of prior information, which are not always available, a more traditional approach can be used: the maximum likelihood approach, which results in the formulation of an objective function to be minimized. This objective function is given by the sum of the square of the residuals between the experimental data and the corresponding physical quantity calculated by the direct model - the classical least squares functional.

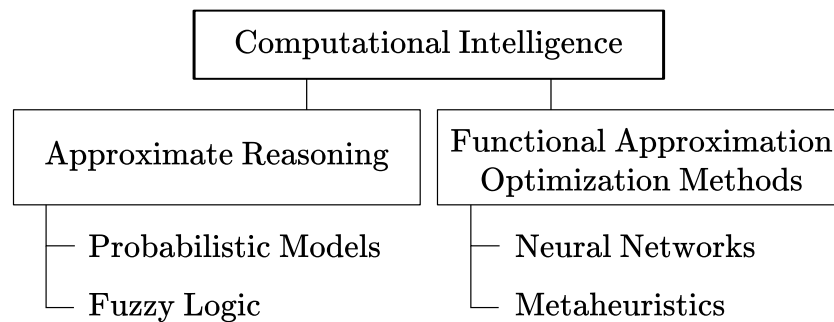
1.2 Computational Intelligence concepts

In all these different types of inverse problems, one important factors is always present: experimental data are imprecise, *i.e.*, errors of measurements are always present in the input. Therefore, the application of Computational Intelligence techniques is a

viable way to deal with inverse problems due to its nature of dealing with errors. The employment of efficient computational procedures to solve inverse problems must keep two objectives in mind: to minimize the amplification of measurements errors and also minimize the computational cost to obtain the sought solution - more often than not these two objectives are not simultaneously achieved.

At this point, a more detailed description of the components that make up the range of tools of Computational Intelligence must be presented. The field can be readily divided in two main categories: Approximate Reasoning and Functional Approximation. These are antagonistic concepts to the ones of Hard Computing of Logical Symbolic Reasoning and Classical Optimization. Figure 3 presents a scheme of what fields are present in this Computational Intelligence division (12). The components of Approximate Reasoning reaches Probabilistic Models and Fuzzy Logic. The ones of Functional Approximations and Optimization Methods covers Neural Networks and Metaheuristics, as portrayed in Figure 3.

Figure 3 – Schematic representation of Computational Intelligence concepts



Source: The author, 2023.

1.2.1 Neural Networks

Artificial Neural Networks (ANN) are computational processing structures inspired by how brains work. The so called neurons are arranged in layers and, generally, there are input, hidden, and output layers. In classical feed forward ANN's, the information flows from the input to the output, where linear and non-linear modifications are performed (17).

Today, the success of such Machine Learning algorithm is outstanding. It has become one of the most used algorithms used for classification, clustering, pattern recognition and more, permeating the most diverse fields and disciplines and prediction in many disciplines

(18). Accordingly to Dave and Dutta (19), 5 key criteria must be taken into account for the proper use justification of a neural network:

- some kind of association has to be established within a set of patterns;
- the dataset is very large and diverse;
- number of variables is high;
- the relationships between variables need to be understood; or,
- the relationships are difficult to describe adequately with conventional approaches.

From these items, it is possible to conclude that the best use for neural networks occurs in complex problems where there is some relationship between input and output data. For this reason, the acquisition of training data with diversity and quantity must be adequate for the non-linearity of the problem addressed.

1.2.2 Fuzzy Logic

Introduced in 1960's by Zadeh (20), Fuzzy Logic and reasoning is a way of making calculations considering degrees of truth. In other words, instead of using boolean operations – yes or no, one or zero, etc – this kind of logic uses values between zero and one in order to associate some classification (11).

One of the main characteristics of fuzzy techniques is the great ability to deal with problems smoothly. That is, when a system requires decisions that are based on a certain set of input parameters, these decisions can often become abrupt in its mathematical space (21).

1.2.3 Metaheuristics for optimization

Metaheuristics methods to solve optimization problems have been around for roughly forty years. According to Osman and Laporte (22), metaheuristics can be defined as a process “which guides a subordinate heuristic by combining intelligently different concepts for exploring and exploiting the search space”. This definition holds two important aspects: a script provided for methods to act together with a common goal and the intelligent combination of features to reach this goal.

This class of methods have increased in popularity and is now a well established approach to solve efficiently many hard optimization problems (23). For example, three of the most well known global optimization algorithms are the Differential Evolution (24), the Particle Swarm Optimization (25), and the Simmulated Annealing (26) - which are employed in the most diverse types of problems.

1.2.4 Probabilistic Models - Bayesian Inference

Probabilistic Models can be defined as any process that incorporate probability as a calculation feature. For instance, in inverse problems, a Bayesian approach can be classified as a type of probabilistic model.

In the Bayesian approach, all the available priori information for solving the inverse problem must be used. This includes the modeling of the experimental error, the priori likelihood distribution of the parameters of interest, among others (27).

In cases where the the parameters priori information can be modeled as a normal distribution, an objective function to be minimized is defined. This approach is known as Maximum a Posteriori. The posterior distribution can be exactly obtained for linear problems, but for non-linear ones, an approximation can be efficiently calculated with the Gauss-Newton method (28).

2 CONTACT FAILURE IDENTIFICATION IN MULTILAYERED MEDIUM VIA SINGLE DOMAIN FORMULATION AND ARTIFICIAL NEURAL NETWORKS

2.1 Introduction and background

Heat transfer in multilayered media is a phenomenon that can be fundamentally important in different applications of science and engineering, such as manufacturing of composite materials (29), oil and gas industry (30), thermal based health treatments (31), aerospace engineering (32) and many others. More specifically, defect identification in the process of bonding among different materials can be formulated as a multilayered media and solved as an Inverse Heat Conduction Problem (IHCP), where estimating the positioning of air gaps, oil bubbles, and cracks, usually is performed by estimating thermophysical properties of the adhesive layer. Therefore, estimating heterogeneity in this layer may be crucial to evaluate the bonding quality (33, 34, 35).

In classical approaches, IHCPs can be treated as optimization problems, where a least squares functional must be minimized (5, 36), or as bayesian inference problems, such as the Maximum a Posteriori and the Markov Chain Monte Carlo methods (37, 38). Since these types of IHCPs formulations require intensive iterative procedures, many efforts of the scientific community are focused on reducing the computational costs related to techniques, algorithms and mathematical formulations (39, 40). Parallel to these efforts, the use of computational intelligence emerged as a possible approach for solving IHCPs, such as Genetic Algorithms (41, 42) and Artificial Neural Networks (ANN) (43, 44, 45, 46), which are considered soft computing approaches, as opposed to classical ones.

The use of ANNs has been permeating the most eclectic types of applications, such as engineering, financial analysis, image and speech recognition, medicine, among many others. This success can be credited to several factors, one of them being the notable improvements and developments of different ANN architectures, such as Autoencoders (AE), Recurrent Neural Networks (RNN), Convolutional Neural Networks (CNN), Extreme Learning Machines (ELM), and so on. The use of any of these architectures must take into consideration its specific features along with characteristics of the problem being solved.

Recently, several of these architectures emerged as viable techniques for defect characterization using IHCPs with infrared thermography. In 2019, Hu et al. (47) employed

a long short term memory RNN for automatically classifying different types of common defects occurring in honeycomb materials. Later, in 2020, Fang & Maldague (48) used a Gated Recurrent Units (GRU) for depth prediction in composite material samples. Kaur et al. (49) introduced a novel Constrained Autoencoder in order to reduce the dimensionality of temporal thermographic images for defect depth estimation in steel plates in 2021. Also in 2021, Marani et al. (50) used step-heating thermography combined with CNN in order to describe defects in composite laminates. In 2021 again, Xu & Hu (51) performed defect depth identification by using a method based also on GRUs.

Besides the cited innovation in networks architectures, the most widely used in the field of heat transfer engineering is the simple feed-forward back propagation Multilayer Perceptron (MLP). Indeed, this network has been proved to be a great general purpose approximator in countless applications, but it lacks some advantages that a specific deep neural network, such as CNNs, AEs, RNN and others may give.

In this context, AEs (or Replicator networks) are great tools designed for reducing the dimension of any given data (17, 52). Such network have the input equal to the output, but its main aspect is a bottleneck-like hidden layer (latent space) which is smaller in dimension than the input-output. When properly trained, the original data can be encoded into this smaller dimension latent space, then the information in this space can be decoded back into the original information size. Furthermore, AEs can be specially designed as a noise reduction network, also known as Denoising Autoencoders (DAE). This can be performed by giving a noisy data as input, passing it through the latent space, then outputting a noiseless version of that same data. If well trained, the information stored in the latent space is an almost-noiseless representation of the original data.

In this work the IHCP of estimating the spatially varying thermal properties of multilayered media is solved via an ANN, where the input data are temperature measurements of an exposed surface and the output is a set of discrete points representing the thermal properties of different materials. More specifically, we used an encode-decode architecture, where the normalized experimental temperature and the thermal properties are encoded separately with respective AEs, then the latent space of each one of them are used as input and output, respectively, for the multi layer perceptron (MLP) neural network. Although this approach imposes the training of three ANN (two AEs and one MLP), which yields an extra computational cost when compared to a simple MLP, the use

of the AE shows advantages such as the robustness to different architectures, as presented in the obtained results.

In order to test this approach, the problem of contact failures identification was chosen, where two materials are joined with an adhesive layer. Gaps of air can form in this layer, meaning that the adhesion process is not perfect (33, 34, 35). Identifying the thermal properties of this layer containing gaps is crucial to access the adhesion quality in manufacturing and preventive maintenance.

In this work, the training data set is generated by solving the direct problem, i.e., the temperature profiles are simulated and obtained for different configurations of failures. Furthermore, the temperature data containing simulated noise is used to train a DAE, where its output is the noise free version of the same data. Due to its dimensionality and noise reduction, this approach can greatly benefit the use of increasingly larger data, as presented in the results. Also, some effort goes into fine tuning the parameters of the ANN itself, such as transfer function, layer sizes, number of neurons, and so on. As mentioned, this is where the encoded-decoded approach shows its promising characteristics, by yielding robust results for different types of configurations.

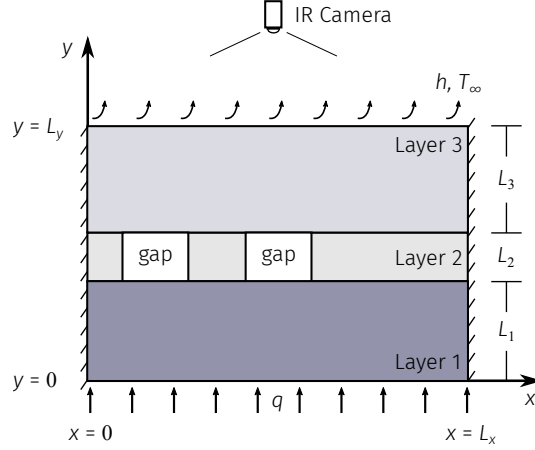
2.2 Direct Problem Formulation and Solution

Consider the $L_x \times L_y$ multilayered rectangular medium presented in Figure 4 composed by three different layers. Such representation can model the bonding of two materials, where Layer 1 and 3 are joined by an adhesive layer shown as Layer 2. In the configuration of Figure 4, two defects are illustrated in the adhesive layer. Both left and right boundaries are considered adiabatic, the constant heat flux q is prescribed at the bottom boundary, and the top one is considered exposed, with ambient temperature of T_∞ and natural convection heat transfer coefficient h . Temperature measurements \mathbf{T}^{exp} are acquired at the exposed boundary, i.e., $y = L_y$.

Using a single-domain formulation (35) and taking in consideration the mentioned assumptions, the heat conduction problem can be written as

$$\frac{\partial}{\partial x} \left(k(x, y) \frac{\partial T(x, y, t)}{\partial x} \right) + \frac{\partial}{\partial y} \left(k(x, y) \frac{\partial T(x, y, t)}{\partial x} \right) = \rho(x, y) c_p(x, y) \frac{\partial T(x, y, t)}{\partial t} \quad (2.1a)$$

Figure 4 – Schematic representation of the multilayered medium.



Source: Jardim et al., 2022 (53).

$$\left. \frac{\partial T(x, y, t)}{\partial x} \right|_{x=0} = 0 \quad \left. \frac{\partial T(x, y, t)}{\partial x} \right|_{x=L_x} = 0 \quad (2.1b,c)$$

$$-k(x, y) \left. \frac{\partial T(x, y, t)}{\partial y} \right|_{y=0} = q \quad k(x, y) \left. \frac{\partial T(x, y, t)}{\partial y} \right|_{y=L_y} + hT(x, L_y, t) = hT_\infty \quad (2.1d,e)$$

$$T(x, y, 0) = T_\infty \quad (2.1f)$$

where h is the convection heat transfer coefficient at the top boundary, and q is the prescribed heat flux at the bottom boundary. The materials properties $k(x, y)$, $\rho(x, y)$, and $c_p(x, y)$ are the thermal conductivity, specific mass, and specific heat, respectively. These spatially dependent properties are modeled in such way to represent the different materials of the multilayered medium. Furthermore, the initial temperature is considered equal to the ambient temperature T_∞ .

If all the thermophysical properties and all the conditions and contact failures geometries are known, the problem described by Eq. 2.1 can be solved yielding the temperature profile $T(x, y, t)$. In this work this solution is obtained by using the built-in “NDSolve” routine of the Wolfram Mathematica 11.0 software. This routine is executed with the Finite Element Method option and the mesh is generated with rectangular user defined uniform cell size. This routine returns an interpolated temperature profile $T(x, y, t)$ for the whole $L_x \times L_y$ medium and for times ranging from $t = 0$ to $t = t_{\max}$, which is a

prescribed maximum time instant.

2.3 Inverse Problem Formulation

Consider that the materials of the multilayered medium presented in Figure 4 are known, but the existence and position of possible defects in Layer 2 are unknown. In this case, the inverse problem is formulated based on the assumption that Layer 2 is composed entirely by adhesive or by adhesive with air gaps (defects). This leads to the definition of an auxiliary function $\gamma(x)$ which represents the thermal properties $k(x, y)$ and $\rho(x, y)c_p(x, y)$ of Layer 2, defined as

$$\gamma(x) = \frac{\phi(x) - \phi_{\text{gap}}}{\phi_{\text{layer}} - \phi_{\text{gap}}} \quad (2.2)$$

where $\phi(x)$ is the related thermophysical property, that is, the thermal conductivity $k(x, y)$ or the volumetric heat capacity $\rho(x, y)c_p(x, y)$, of Layer 2 materials. Assuming that there is no variation in the y direction within the materials of Layer 2, $\gamma(x)$ is considered only as an x variable function. Also, the subscripts “gap” and “layer” represent the related material thermal properties. The function γ is used algorithmically as a way to translate the thermal properties to the spatial dependent boolean function “gap, no-gap”, “0” or “1”, respectively. Furthermore, γ can be reversely translated to the thermal properties $k(x, y)$ and $\rho(x, y)c_p(x, y)$ of Layer 2, since the values ϕ_{gap} and ϕ_{layer} are known.

In order to obtain estimates of the gaps positioning in Layer 2, an ANN is used to represent the inverse model, i.e. the network receives temperature experimental data as input and outputs a vector representing discrete points of the auxiliary function $\gamma(x)$.

Experimental Data. In order to simulate real measurements of temperature, the experimental data is computationally generated, where random numbers r drawn from a normal distribution centered at zero with known standard deviation σ_{exp} are added to solution of the direct problem, i.e.,

$$T_{i,j} = T(x_i, L_y, t_j) \text{ with } i = 1, 2, \dots, N, j = 1, 2, \dots, M \quad (2.3a)$$

$$T_{i,j}^{\text{exp}} = T_{i,j} + r, r \sim \text{N}(0, \sigma_{\text{exp}}^2), \text{ with } i = 1, 2, \dots, N, j = 1, 2, \dots, M \quad (2.3b)$$

where x_i represents the positioning of temperature acquisition along the x coordinate with the total number of N points, and t_j the time instants with total number of M levels. Therefore, the total number of experimental data considered is $N_{\text{exp}} = N \times M$.

2.4 Inverse Problem Solution with Artificial Neural Networks

As previously mentioned, the IHTP of this work has the objective of estimating the positioning of gaps that can occur in Layer 2 of the medium (see Figure 4). This task is performed by estimating discrete points of the auxiliary function $\gamma(x)$: this is the ANN output. The input consists of transient temperature measurements that are encoded into a latent space of an AE, which is used with the purpose of reducing the dimension and noise on the experimental data. This latent space serves as the input to a fully connected MLP network that yields another latent space of the same size of the first one. This last latent space is then decoded to a full representation of the auxiliary function γ . With this approach, both latent spaces are used as input and output, respectively, to the fully connected MLP neural network.

In the following subsections, the two AEs and MLP construction are explained and detailed. Firstly, the temperature and γ AE are presented. Next, the complete network architecture is showcased. Lastly, general aspects necessary to build the network and the simulated data set are shown.

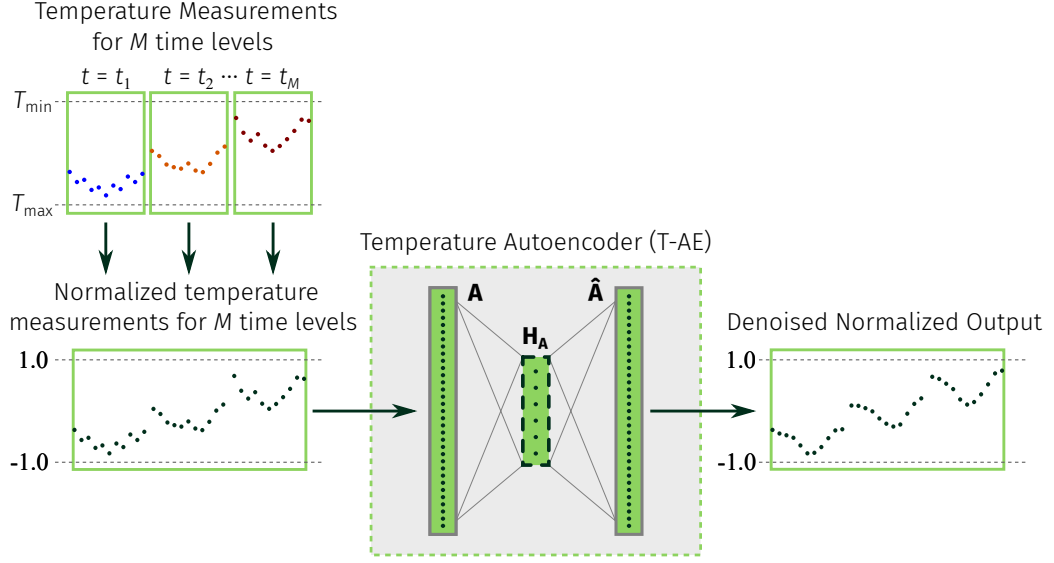
2.4.1 Autoencoders

2.4.1.1 Temperature Autoencoder (T-AE).

Consider the AE structure presented in Figure 5. The input \mathbf{A} is fully connected to one hidden layer, represented by $\mathbf{H}_{\mathbf{A}}$, which is the latent space. Then $\mathbf{H}_{\mathbf{A}}$ is fully connected to the output $\hat{\mathbf{A}}$. These connections are all modified by weights, biases, and activation functions.

As presented in Figure 5, the AE input \mathbf{A} and output $\hat{\mathbf{A}}$ are normalized versions of \mathbf{T}^{exp} and \mathbf{T} , respectively (see Eq. 2.3). The components of \mathbf{A} are the normalized version of \mathbf{T}^{exp} , and the ones for $\hat{\mathbf{A}}$ are the normalized version of \mathbf{T} , both ranging between -1 and 1 . These linear normalizations are performed with limits of T_{min} and T_{max} , which are the minimum and maximum exact temperature values of the entire training set (see

Figure 5 – Schematic representation of the Temperature Denoising Autoencoder.



Source: Jardim et al., 2022 (53).

subsection entitled *General Aspects of the Artificial Neural Network* for details).

The T-AE implemented in this work has only one hidden layer, which is the latent space itself, but in some cases, AE's can have many hidden layers as the problem requires. Using the architecture with the single hidden layer, tests with different simulated experimental data led to good approximations, making the increased network with more layers unnecessary.

Choosing the latent space \mathbf{H}_A dimension is crucial to a good performance of the AE. If too small, some information will be lost, leading to a poor representation of the temperature data. On the other hand, if its dimension is too large, training requires more examples and the problem can become less efficient overall. Therefore a comparison of different \mathbf{H}_A dimensions is performed in this work.

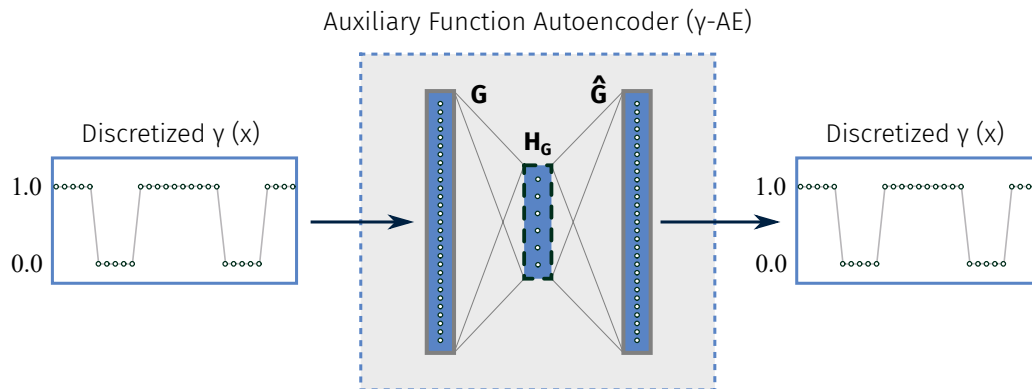
2.4.1.2 Adhesive Layer Properties Autoencoder (γ -AE).

The adhesive layer thermophysical properties is represented by the auxiliary function $\gamma(x)$, which ranges from 0 to 1. The profile of this function represents different material properties and its behavior indicates where there are gaps in the layer.

As presented in Figure 6, this second AE is used to represent γ and has input \mathbf{G} , output $\hat{\mathbf{G}}$ and latent space \mathbf{H}_G . The input \mathbf{G} is composed by discrete points used to

represent γ across the x direction. $\hat{\mathbf{G}}$ is the exact representation of \mathbf{G} , therefore, they are trained to be equal. The latent space $\mathbf{H}_{\mathbf{G}}$ dimension is chosen to be equivalent as $\mathbf{H}_{\mathbf{A}}$, i.e., equal to the T-AE latent space dimension.

Figure 6 – Schematic representation of the Adhesive Layer Properties Autoencoder using the Auxiliary Function $\gamma(x)$.



Source: Jardim et al., 2022 (53).

It is important to note that this Adhesive Layer Properties AE has to encode less information than the T-AE presented, since it has only to output 0 or 1, so tests with dimensions smaller than the T-AE size yielded good results, which is expected. Nevertheless, in this work the choice of maintaining both latent space sizes equal is kept.

2.4.2 Final Artificial Neural Network Model

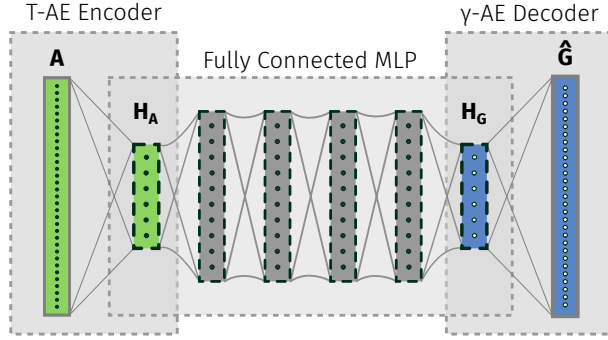
In order to transform $\mathbf{H}_{\mathbf{A}}$ into $\mathbf{H}_{\mathbf{G}}$, a fully connected MLP is used, i.e., this network model has to translate latent spaces information from temperature measurements to the adhesive layer properties in terms of $\gamma(x)$. Therefore, $\mathbf{H}_{\mathbf{A}}$ and $\mathbf{H}_{\mathbf{G}}$ are the input and output to the MLP, respectively, where hidden layers are connected and the information passing is modified by weight, biases and activation functions.

The final ANN architecture is displayed in Figure 7, where it is possible to see the normalized experimental temperature input \mathbf{A} . This input is encoded into $\mathbf{H}_{\mathbf{a}}$, which is then passed and transformed into $\mathbf{H}_{\mathbf{G}}$ to finally be decoded as $\hat{\mathbf{G}}$. With this approach the actual $\gamma(x)$ estimation process utilizes only machine information, which is an advantage to obtain more robust models. Also, it is important to note that such network model allows to an increased dimension of the temperature input data, which is desirable with a transient problem. To illustrate this aspect of the ANN model, different time instants are

considered and compared in this work.

The training of the Fully Connected MLP in Figure 7 is performed by using the same training set that trained all the other models. To perform this task, firstly, the two AE's must have been properly trained. Then, all the experimental temperature of the training set is encoded into \mathbf{H}_A and all the respective discretized $\gamma(x)$ profiles are encoded into \mathbf{H}_G . With this, the pairs $\mathbf{H}_A \rightarrow \mathbf{H}_G$ are assembled and the model can be trained.

Figure 7 – Schematic representation of the complete network model.



Source: Jardim et al., 2022 (53).

2.4.3 General Aspects of the Artificial Neural Network

To build the training data set for the three ANN, a list of input-output pairs is necessary. One training pair for the T-AE is composed by the rule $\mathbf{A} \rightarrow \hat{\mathbf{A}}$, which are the normalized versions of the experimental data \mathbf{T}^{exp} and the exact temperature data \mathbf{T} , respectively. Similarly, the material property AE uses the pair $\mathbf{G} \rightarrow \hat{\mathbf{G}}$, which is the discrete representation of the exact γ used to generate that particular \mathbf{T} and \mathbf{T}^{exp} . After completing the training of both AE's, the set for the MLP can be build with input \mathbf{H}_A and output \mathbf{H}_G by using the two AE's to translate the original training set into the related latent space.

To build this training data set, the direct problem is solved with a given random thermophysical properties profile for Layer 2 containing gaps, which is represented as the auxiliary function γ . Furthermore, it is important to follow some criteria that represents the physics of the problem in order to avoid unnecessary computations (46). In this work, the training data set is built by assuming that:

- There is a maximum number of gaps in Layer 2, i.e. $N_{\text{gap}} = 1, 2, \dots, M_{\text{gap}}$;

- There is a minimum gap size, namely L_{\min} ;
- The gaps only occur in the region of $x_{\min} \leq x \leq x_{\max}$, where x_{\min} and x_{\max} are chosen to avoid gaps being too close to the boundaries.
- The T-AE and final MLP dataset are composed of multiple copies of the original set, with each one containing different level of noise for \mathbf{T}^{exp} .

These rules are a way to generate meaningful information to the ANN model. For example, if the gap is too narrow, it will not influence the temperature on the exposed surface of the medium, specially considering experimental noise. Furthermore, the last rule is included in order to generalize the noise reduction aspect of the T-AE, by giving different noise levels in the data set.

2.5 Results and discussion

2.5.1 Direct Problem Solution

Considering a steel plate for Layer 1, adhesive for Layer 2, composite protection for Layer 3 and air as the inclusions in the possible defects (gaps), the respective thermophysical properties used are displayed in Table 1.

Table 1 – Thermal Properties for the Multilayered Medium

Layer	k [W/mK]	ρc_p [MJ/m ³ K]
1	13.400	3.860
2	0.700	1.750
3	1.171	2.650
Gaps	0.0263	1.170

Source: Jardim et al., 2022 (53).

Furthermore, to obtain the results of the direct problem, the prescribed heat flux, the natural convection coefficient, and the ambient temperature are defined as $q = 10000$ W/m², $h = 15.0$ W/m²K, and $T_{\infty} = 20.0$ °C, respectively. The medium dimensions are defined as $L_x = 0.2$ m and $L_y = 0.071$ m, and Layer 2 is vertically positioned in the range $0.05 \leq y \leq 0.051$ m.

2.5.2 Training, Validation and Testing Sets Generation

All the training and validation data are generated with 1, 2 or 3 gaps in Layer 2, i.e. $M_{\text{gap}} = 3$. For each particular number of gaps, 2000 randomly positioned gaps configurations are used to obtain the respective transient temperature profile, yielding a total of 6000 direct problem evaluations. The training and validation data are then split into a 90% to 10% relation, respectively. Therefore, from this total set, 5400 are used for training and 600 for validation.

To build the simulated experimental data used for the training process of the T-AE and the MLP, four levels of random noise are considered for σ_{exp} , they are 0.05 °C, 0.1 °C, 0.15 °C and 0.20 °C (see Eq. 2.3b). This type of measurement is typically obtained via infrared thermography techniques (54). Hence, four sets of 6000 input-output pairs compose the final training data, yielding 24000 examples (21600 for training and 2400 for validation). It is important to notice that the γ -AE training is performed with the original 6000 auxiliary function profiles.

The testing data is generated similarly to the training and validation set. It is composed of 150 random positioned defects (50 for 1, 2, and 3 simultaneous failures). The same noise levels are considered, therefore the original 150 data is copied yielding 600 examples for the T-AE and MLP testing - the γ AE keeps the original 150.

In order to illustrate how efficiently the AE can store information in its latent space, the results of this work compares three problems with different time instants for the measured experimental data. For $M = 3$ time instants, 600 s, 800 s, and 1000 s are considered, for $M = 5$, 600 s, 800 s, 1000 s, 1200 s and 1400 s, and lastly, for $M = 7$, the instants range from 600 s to 1800 s in steps of 200 s. For every instant, $N = 321$ points in the x coordinate are considered. So, for problems with 3, 5 and 7 time levels, the ANN must deal with a input of 963, 1605 and 2247 data, respectively. These time instants and total amount of input data are displayed in Table 2.

It is important to notice that the model proposed in this work considers increasingly time levels of physical experiment. In other words, for $M = 3$, $M = 5$ and $M = 7$, the final time of temperature acquisition is 1000 s, 1400 s and 1800 s, respectively. Therefore there is a trade off between amount of data and temporal information available. At the lower spectrum, for $M = 3$, less temperature readings are used, making the model training and configuration more efficient. On the other hand, for $M = 7$, the larger data set can

Table 2 – Time Instants and number of temperature data used.

M	Time Instants	Data Size
$M = 3$	600 s, 800 s, 1000 s	963
$M = 5$	600 s, 800 s, 1000 s, 1200 s, 1400 s	1605
$M = 7$	600 s, 800 s, 1000 s, 1200 s, 1400 s, 1600, 1800 s	2247

Source: Jardim et al., 2022 (53).

contain useful transient information of the problem, in exchange of training and model configuration efficiency. Hence, $M = 5$ can be considered as the middle point of the two mentioned.

The exact maximum temperature values necessary to normalize the training data set between -1 and 1 are different for the sets with 3, 5 and 7 time instants, they are: 35.5718 °C, 47.8281 °C and 60.5670 °C, respectively. The minimum temperature obtained is equal for the three sets, with value of 21.1653 °C, which occurs for $t = 600$ s.

2.5.3 Temperature Autoencoder Results

The T-AE implementation is performed using the Keras library, from Python 3.9 programming language. The Logistic Sigmoid activation function is selected for the hidden layer and the output layer is kept as linear. The Adam optimizer is selected as implemented within the Keras library and the Logarithmic Hyperbolic Cosine (log-cosh) is chosen as the loss function. Such function has the advantage of being totally differentiable, with a L_2 norm behavior for small values of its argument, and as L_1 for larger values (55).

Early Stopping is selected as the stopping criterion. When the minimum loss function value found during training for the validation set does not change for 200 epochs, the iterative procedure is stopped. Then, the weights and biases obtained for the best epoch are used. This approach avoids over fitting of the training data (56). Furthermore, the maximum number of epochs is set to 6400, but none of the configurations tested reached that value. Finally, the batch size selected is 256, which is a relatively large size, but results have shown to be a good compromise between quality and speed of training.

In Table 3 the results obtained for the T-AE with $M = 3$ time instants are displayed for different latent spaces dimensions, namely “AE dim” column. The table displays the

Validation and Testing Mean Squared Errors obtained (MSE), along with the number of Training Epochs needed for that particular result. The result displayed as “Max. error” represents the maximum relative temperature error. This error is obtained with the following expression

$$\text{Max. error} = \max \left(\left| \frac{\hat{T}_{i,j,k} - T_{i,j,k}}{T_{i,j,k}} \right| \right) \times 100 \quad (2.4)$$

where \hat{T} and T are the denormalized T-AE output and exact temperatures, respectively, both obtained for each testing data k , time level j and point in space i .

Table 3 – Temperature Autoencoder (T-AE) MSE results for 3 time instants and different Autoencoder (AE) dimensions

AE dim.	Val. MSE (10^6)	Test MSE (10^6)	Max. error %	Epochs
20	25.170385	24.700969	1.021519	1314
40	14.667914	14.616520	0.881631	1126
60	10.545812	10.572952	0.673743	1021
80	7.853343	7.673714	0.543680	1875
100	8.831671	8.996550	0.544467	1217
120	8.089550	8.317249	0.594848	1295
140	7.684247	7.809486	0.542980	1583
160	8.395999	8.263888	0.516542	1027

Source: Jardim et al., 2022 (53).

As it is possible to see in Table 3, the AE dimensions such as 20, 40 and 60 generated the worst MSE results for the validation and testing set. Nevertheless, it is possible to notice that, with the exception of the AE with 20 dimensions, every configuration yielded a maximum error lower than 1%. Here is also possible to see that, in general, the epochs necessary to reach the stopping criterion ranges from 1021 to 1875, which can be considered a relatively low discrepancy. From the Test MSE criterion, the best configuration was the 80-dim AE. Here it is important to note that the MSE metric tends to increase larger errors, due to its squared argument. This is a desirable feature for comparing different ANN configurations, the best networks tend to have small and low discrepancy among them, whereas the worst configurations will generate larger values with higher discrepancy among themselves.

The T-AE results for $M = 5$ and $M = 7$ time instants are presented in Table 4 and Table 5, respectively. For both results it is possible to see that the validation and

testing MSE tends to decrease as the AE dimension increases. For $M = 5$, the maximum error values are also lower than 1% with exception of the 20-dim AE, which is not true for $M = 7$, since only the dimensions 120, 140 and 160 generated lower than 1% maximum relative errors. This can be explained in the light of the amount of data considered for 7 time instants and their range, i.e., since all the data is normalized between -1 and 1, the more information one fits inside this range, the more difficult becomes to the network train with efficiency. Nevertheless, the lowest validation and testing MSE generated the lowest maximum relative error for $M = 7$ (120-dim: 4.08, 3.97 and 0.63%).

Table 4 – T-AE MSE results for 5 time instants and different AE dimensions

AE dim.	Val. MSE (10^6)	Test MSE (10^6)	Max error %	Epochs
20	31.454491	30.781830	2.285817	1182
40	9.214962	9.460896	0.984900	2242
60	5.495272	5.311201	0.602837	1664
80	5.777369	5.447388	0.769883	1185
100	5.811261	5.820386	0.725761	774
120	4.109372	4.142637	0.532461	1481
140	4.518737	4.532548	0.600322	1157
160	3.567894	3.335813	0.564507	1095

Source: Jardim et al., 2022 (53).

Table 5 – T-AE MSE results for 7 time instants and different AE dimensions

AE dim.	Val. MSE (10^6)	Test MSE (10^6)	Max error %	Epochs
20	32.861363	32.541317	2.374726	2217
40	9.426475	9.157836	1.144972	2459
60	10.696455	9.888308	1.453967	921
80	8.383932	8.169459	1.184161	892
100	6.024927	6.137550	1.347719	659
120	4.084239	3.969270	0.632970	938
140	4.491201	4.456416	0.728079	932
160	4.480562	4.385102	0.735544	732

Source: Jardim et al., 2022 (53).

2.5.4 MLP Results

To construct the complete ANN architecture, it is necessary to specify the elements for the MLP and γ -AE. Firstly, the activation functions for γ -AE latent space and output

layer are the ReLU and Logistic Sigmoid functions, respectively. Since γ -AE outputs the auxiliary function, which ranges between 0 and 1, the Logistic Sigmoid is a reasonable choice that acts similar to a filter, limiting the output values inside that range and, furthermore, results with a linear output yielded undesired oscillations around the exact value. Regarding the loss function for training, the Binary Cross Entropy was selected, which have a good behavior for optimizing values that can be either 0 or 1. Secondly, the MLP is composed of four hidden layers, with the Hyperbolic Tangent (tanh) activation function for each and linear output layer. It is important to note that the MLP input and output sizes are equal as the latent spaces of both AE's, as previously mentioned. The output layer activation is linear and the loss is calculated using the log-cosh functional. Other activation functions such as ReLu, Leaky ReLU and Logistic Sigmoid were tested for the hidden layers, but the best result (including faster training) were obtained with the tanh function. The stopping criterion for training for both γ -AE and MLP is similar as the T-AE, after 200 epochs with no improvements on the validation set loss function ADAM optimizer iterative process stops.

Table 6, Table 7 and Table 8 present the MSE between the exact discretized γ profile and the respective ANN final output for different MLP sizes (number of neurons per hidden layer). Therefore these “Test MSE” results compares the decoded γ -AE output obtained from the MLP output, which MSE error is displayed as “Test $\mathbf{H_G}$ ”.

In Table 6 the results for $M = 3$ time instants are displayed, which were obtained with the 80-dim T-AE (therefore the γ -AE is also used with 80 dimensions). Similarly, Table 7 and Table 8 show the results for 5 and 7 time instants, with T-AE of 160-dim and 12-dim, respectively.

In Table 6, for $M = 3$, the MLP size that yielded the lowest γ MSE was the one with 200 neurons per hidden layer. Nevertheless, the 80 MLP size, which is equal as the used T-AE and γ -AE for this problem, generated the second best result. As it is possible to see, the epochs used for training decreases as the MLP size increases, which is indication that overfitting was avoided. Another important aspect to observe is that the best $\mathbf{H_G}$ MSE was not observed for the same MLP size as the best γ MSE, which indicates that the γ -AE accepts small differences in the latent spaces elements in order to decode it into the same output.

For $M = 5$ and $M = 7$ in Table 7 and Table 8, the best found MLP size was the

one with 40 neurons per hidden layer. Similarly to the results in Table 6, the training epochs needed also decreases when the MLP size increases, and the best \mathbf{H}_G MSE was not observed for the best γ MSE. It is worth noting the the respective best γ output MSE for 3, 5 and 7 time instants were 0.01396935, 0.01423047 and 0.01425704, respectively, indicating that the problem considering 3 instants generated the lowest error. Nevertheless, the three results are relatively similar.

Table 6 – MSE for $M = 3$, 80-dim AE, and different MLP sizes

MLP size	Test MSE (10^2)	Test \mathbf{H}_G MSE (10^2)	Epochs
40	1.497972	0.108321	1947.0
80	1.421108	0.090003	1442.0
120	1.533937	0.108943	1107.0
160	1.492982	0.104258	828.0
200	1.396935	0.102659	723.0

Source: Jardim et al., 2022 (53).

Table 7 – MSE for $M = 5$, 160-dim AE, and different MLP sizes

MLP size	Test MSE (10^2)	Test \mathbf{H}_G MSE (10^2)	Epochs
40	1.423047	0.069287	3382.0
80	1.569511	0.068726	993.0
120	1.490072	0.070474	720.0
160	1.462179	0.068498	612.0
200	1.513545	0.070189	549.0

Source: Jardim et al., 2022 (53).

Table 8 – MSE for $M = 7$, 120-dim AE, and different MLP sizes

MLP size	Test MSE (10^2)	Test \mathbf{H}_G MSE (10^2)	Epochs
40	1.425704	0.119196	2818
80	1.486218	0.117148	904
120	1.647438	0.129891	667
160	1.595111	0.129822	628
200	1.539906	0.125107	558

Source: Jardim et al., 2022 (53).

2.5.5 Detection of Contact Failures

The auxiliary function γ estimation using the best ANN obtained in Table 6, Table 7, and Table 8 are presented in this subsection. To illustrate how the model can generalize the input data with different noise levels, the results are considered for σ_{exp} of 0.1 °C and 0.2 °C.

In order to illustrate the T-AE noise reduction capability, the comparison among simulated experimental temperature data, the denormalized T-AE output, and the exact temperature is displayed in Figure 8a, Figure 9a, Figure 10a, Figure 11a, Figure 12a, and Figure 13a for different contact failures configurations. The simulated experimental temperature is generated with noise level of $\sigma_{\text{exp}} = 0.2$ °C and $M = 3$ (three time instants). The T-AE output is obtained with the 20-dim latent space configuration. In such figures, the $\gamma(x)$ presented indicates the exact auxiliary function profile used to obtain the temperature displayed above each one. For the sake of visualization, the results with T-AE's of 5 and 7 time instants are not displayed.

Although the noise level of $\sigma_{\text{exp}} = 0.2$ °C was the largest used in training, the approximation between the exact temperature profiles and the denormalized T-AE output is excellent, as it is possible to see for every configuration with one (Figure 8a and Figure 9a), two (Figure 10a and Figure 11a), and three (Figure 12a and Figure 13a) contact failures. This indicates that the AE has good dimensionality reduction qualities and it can, indeed, be used as a feature extractor tool, which stores the most important information necessary to reconstruct the temperature data without noise in the latent space.

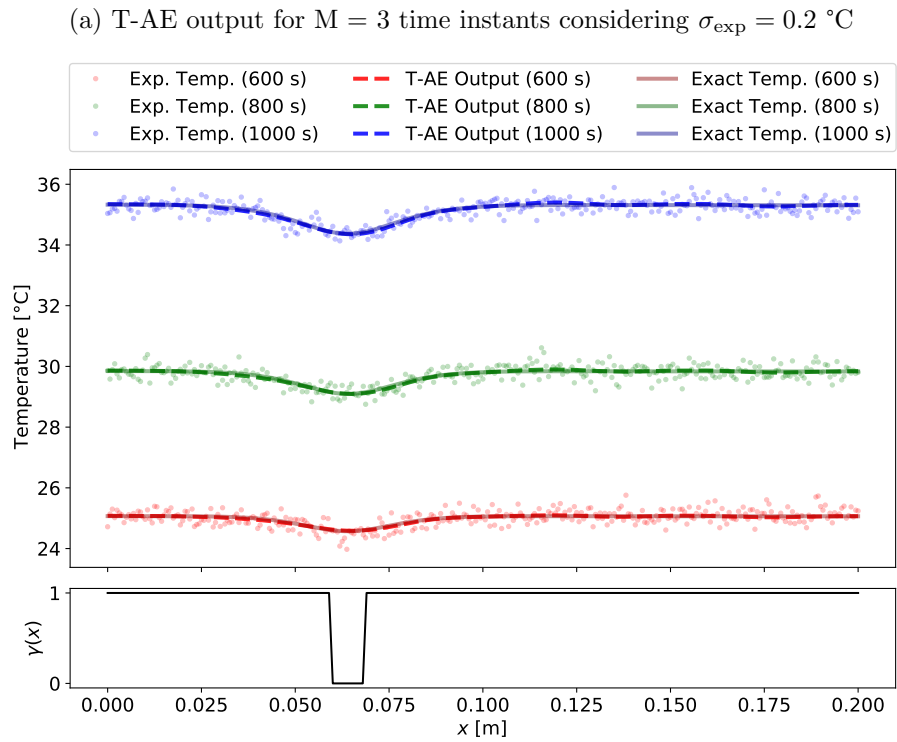
Figure 8b and Figure 9b presents the results for 1 single contact failure, being one small and one large, respectively. Both results shows a good approximation of the estimated γ profile with the exact one. The small gap in Figure 8b has 10 mm, which should be the hardest to detect due to lack of sensitivity, and shows very reasonable fit for all time instants considered. Therefore, this configuration with only one gap can be considered the easiest to estimate.

Now considering two defects in Layer 2, the results are presented in Figure 10b and Figure 11b for two small gaps and for one small and one large gap, respectively. Results in Figure 10b shows two small gaps of 10 mm length and separated by another 10 mm. This configuration show very good results for $M = 5$ and $M = 7$ time instants, for both noise level considered. Although the results for $M = 3$ are good, some undesired oscillation in

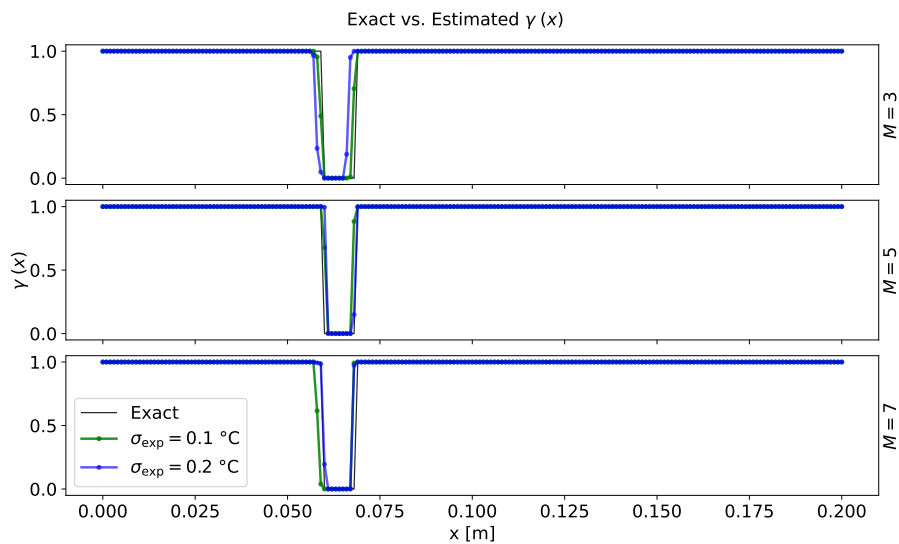
the second gap is found. For one small and one large gaps, the results presented in Figure 11b shows very good agreement to the exact values, considering that they are more far apart from each other. The large gap has 30 mm in length and the small 10 mm.

Finally, the results considering three gaps in Figure 12b and Figure 13b. The former is composed of three small gaps, and the latter with two small and one large. These configuration are the most difficult to estimate, due to the increase non-linearity of the problem: it makes the AE's work harder to extract more information from the temperature data. All the gaps in Figure 12b have 10 mm of length and are separated by 20 mm intervals. Here the agreements of results with exact values are not exactly centered, but, nevertheless, the three gaps positioning is well identified. Specially considering the result with $M = 5$ and 7, which generated less oscillations. For two small and one large gaps, the results showed some difficult in estimation. The best agreement is obtained for $M = 3$ for both noise levels, as indicated by results in the subsection entitled *MLP Results*. In this configuration, the model for $M = 5$ presented some oscillations. Results with $M = 7$ found the correct positioning of the two small gaps, but not the right size of them by estimating larger defects than the exact ones.

Figure 8 – T-AE output (a) and $\gamma(x)$ estimation (b) for one small contact failure configuration.

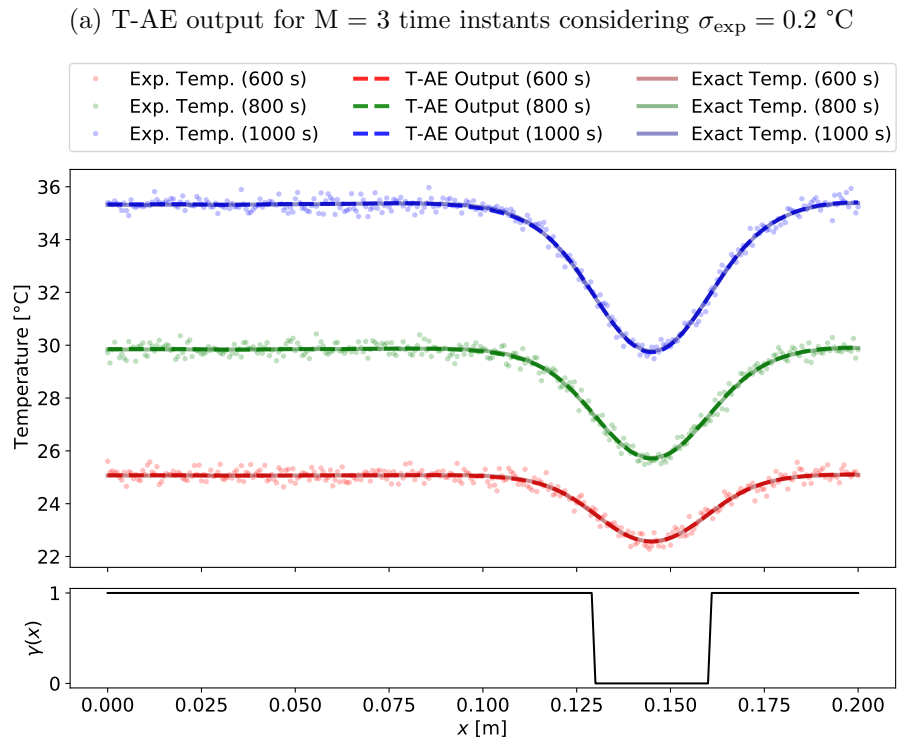


(b) Estimated $\gamma(x)$ comparison for one small contact failure considering $M = 3$, 5, and 7 and noise levels of $\sigma_{\text{exp}} = 0.1 \text{ } ^\circ\text{C}$ and $0.2 \text{ } ^\circ\text{C}$.

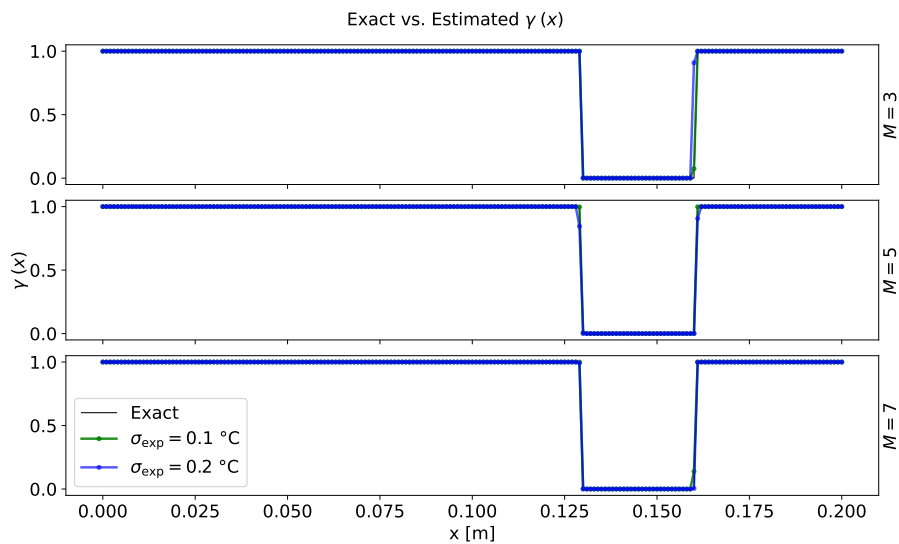


Source: Jardim et al., 2022 (53).

Figure 9 – T-AE output (a) and $\gamma(x)$ estimation (b) for one large contact failure configuration.

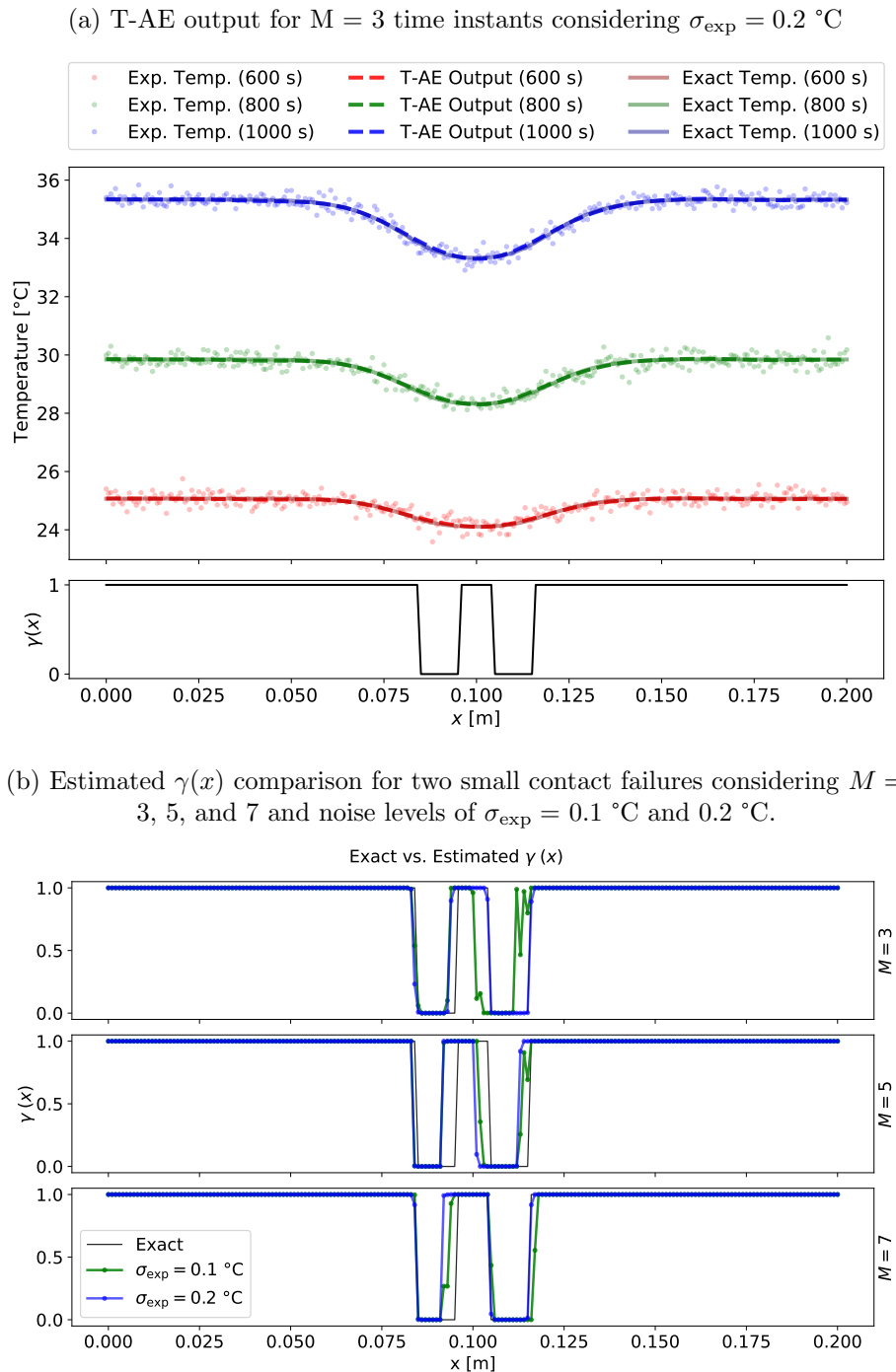


(b) Estimated $\gamma(x)$ comparison for one large contact failure considering $M = 3, 5,$ and 7 and noise levels of $\sigma_{\text{exp}} = 0.1 \text{ } ^\circ\text{C}$ and $0.2 \text{ } ^\circ\text{C}$.



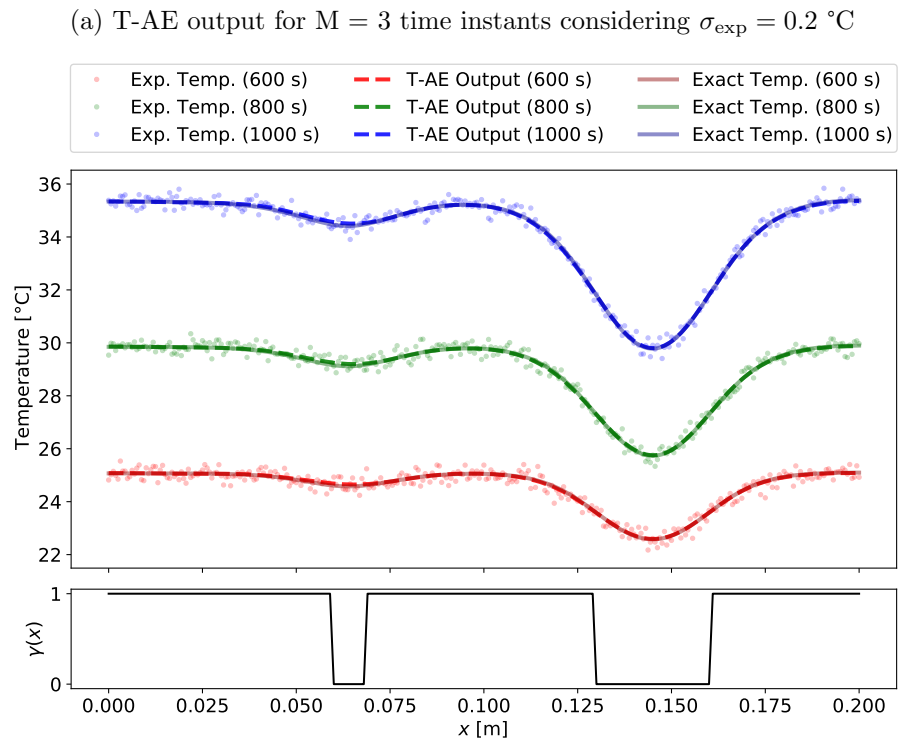
Source: Jardim et al., 2022 (53).

Figure 10 – T-AE output (a) and $\gamma(x)$ estimation (b) for two small contact failures configuration.

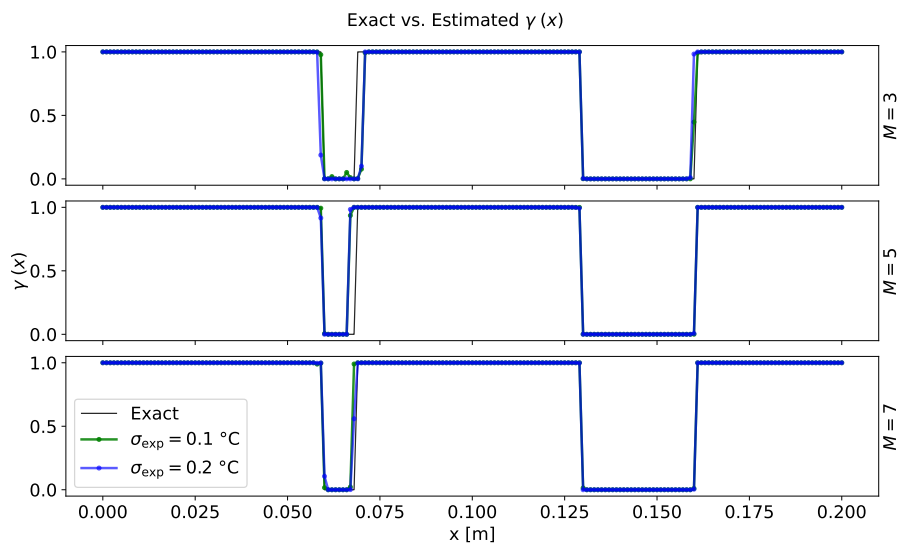


Source: Jardim et al., 2022 (53).

Figure 11 – T-AE output (a) and $\gamma(x)$ estimation (b) for one small and one large contact failures configuration.

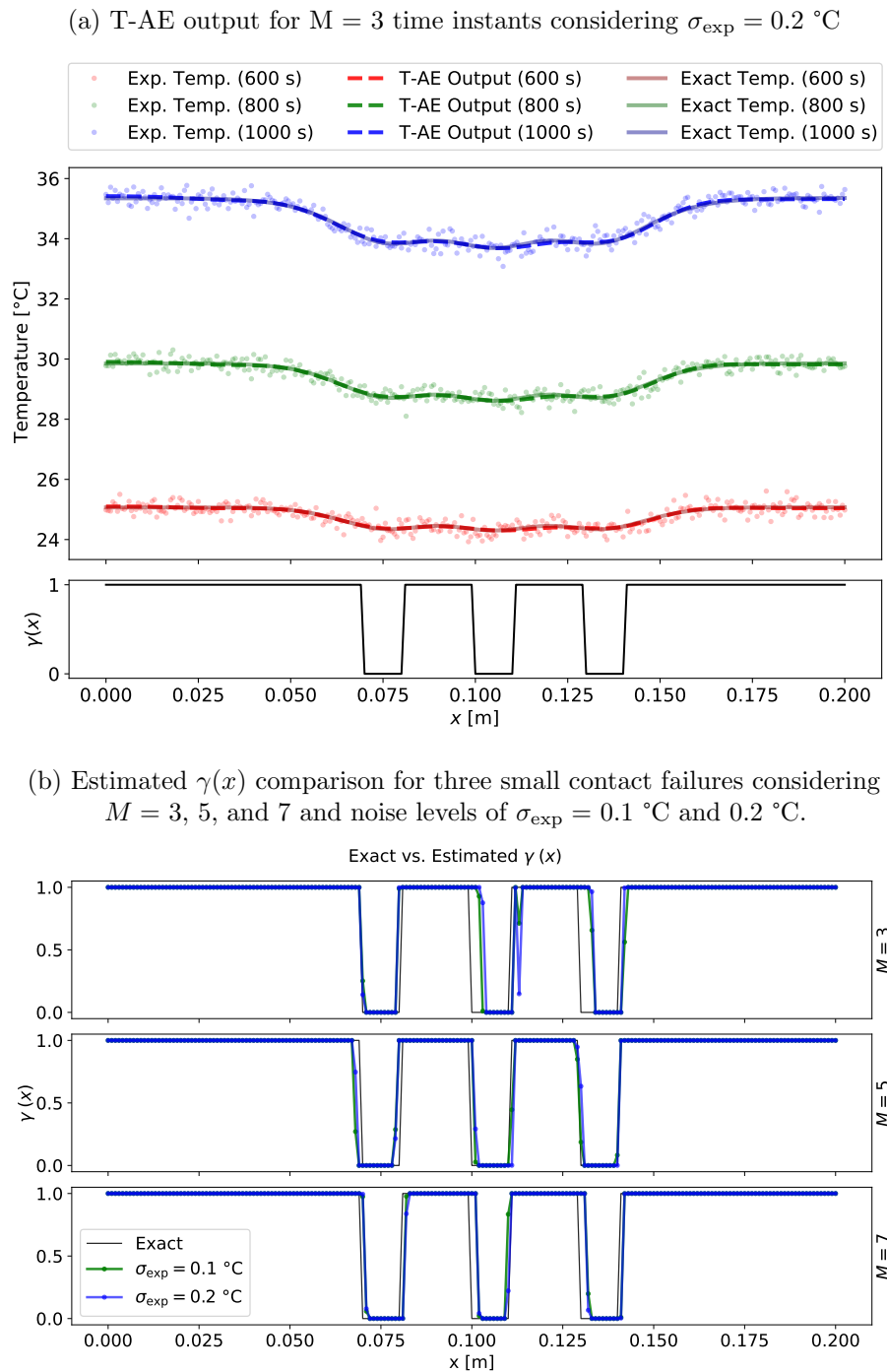


(b) Estimated $\gamma(x)$ comparison for one small and one large contact failures considering $M = 3, 5,$ and 7 and noise levels of $\sigma_{\text{exp}} = 0.1 \text{ } ^\circ\text{C}$ and $0.2 \text{ } ^\circ\text{C}$.



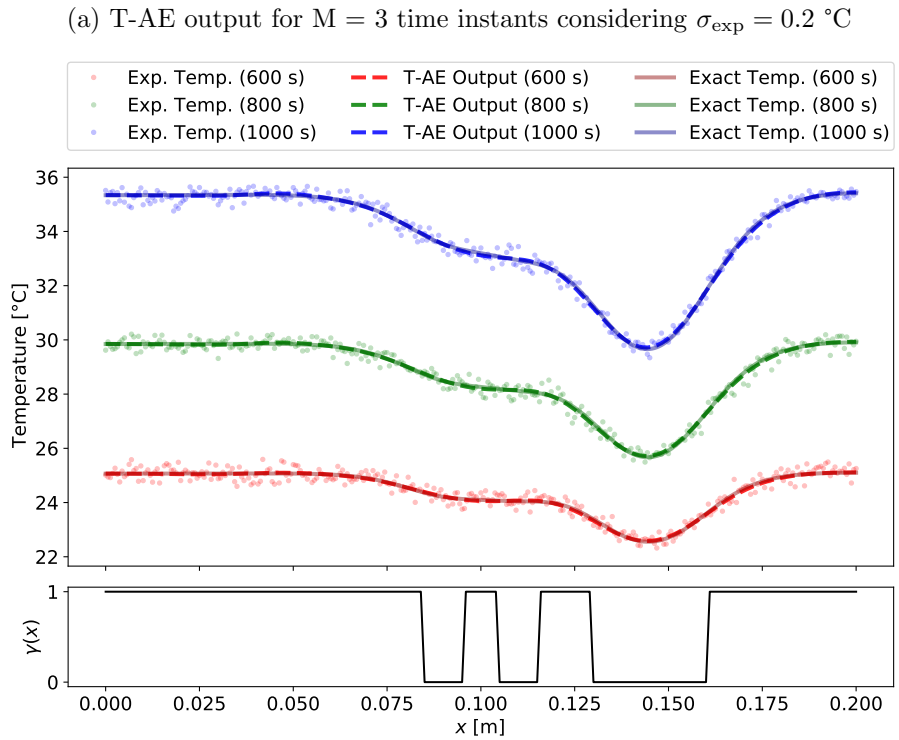
Source: Jardim et al., 2022 (53).

Figure 12 – T-AE output (a) and $\gamma(x)$ estimation (b) for three small contact failures configuration.

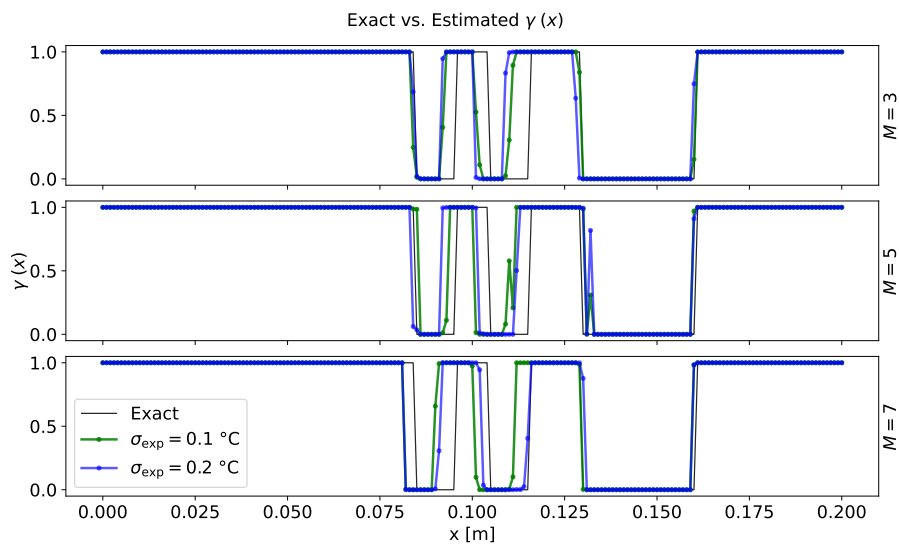


Source: Jardim et al., 2022 (53).

Figure 13 – T-AE output (a) and $\gamma(x)$ estimation (b) for one large and two small contact failures configuration.



(b) Estimated $\gamma(x)$ comparison for one large and two small contact failures considering $M = 3, 5,$ and 7 and noise levels of $\sigma_{\text{exp}} = 0.1 \text{ } ^\circ\text{C}$ and $0.2 \text{ } ^\circ\text{C}$.



Source: Jardim et al., 2022 (53).

The computational times necessary for this investigation can be divided into three categories: training data generation, training of the models, and activation of the neural network. The system used to perform all executions is equipped with a AMD Ryzen™ 5 4600H processor, GeForce® GTX 1650 graphics processor, 8GB of RAM, and Microsoft Windows 10 operational system. Some aspects of computational times for each of the mentioned categories are the following:

- The training data generation is the most intensive computational task of this work. The time necessary to evaluate sequentially the 6000 different direct problem solutions, as described in the subsection *General Aspects of the Artificial Neural Network*, was 15.6 hours. Although this task was performed sequentially, it has a fixed number of iterations and can be easily parallelized in order to reduce this computational time.
- The computational times spent to train the neural networks are varied, given the different architectures and networks types. For the sake of illustration, the training of MLP's with 160 and 200 neurons per layer of $M = 7$ time instants took 3 minutes and 22 seconds, and 2 minutes and 57 seconds, respectively, with both using 628 and 558 epochs to reach the stopping criterion - see Table 8.
- The computational cost of performing the final estimation of $\gamma(x)$ with the three networks is the main motivation for using the approach proposed. For instance, the estimation for $M = 7$ and $\sigma_{\text{exp}} = 0.1$ °C, as presented in Figure 9, takes an average of 0.113 seconds.

2.6 Conclusions

The present work used an ANN in order to estimate the positioning of defects that can occur in the bonding between two materials. To reduce the dimension of the 1D transient thermography experimental data, an AE was used. Different configurations of AE were tested considering data from 3, 5 and 7 time instants, which corresponds to 963, 1605 and 2247 temperature readings, respectively. The main aspects of the proposed approach for solving the defect positioning estimation problem may be summarized as the following items:

- *Speed of estimation.* When compared to classical approaches such as Maximum Likelihood or Bayesian Methods, the use of ANN's for estimating parameters of

the physical problem has a great advantage in computational efficiency. Usually, such classical methods have cumbersome iterative processes that are not practical in some real scenarios. On the other hand, the estimation with ANN's can instantly be obtained.

- *Reduced dimensions of temperature data.* Since the problem solved in this work is transient, several time instants must be included as the ANN input. This work deals with this problem by encoding such transient temperature profiles in order to facilitate the work of estimating failures. Thus, the reduction in dimension was necessary to extract important features of the noisy data and work with a manageable ANN.
- *Increased estimation resolution* Since an AE is also used to reduce the dimension of the output, a larger amount of points can be used to represent the varying thermophysical properties of the adhesive layer.
- *Fixed computational cost for training data generation.* Each training data is generated by solving the direct problem once. Therefore, the amount of examples needed to train the model is generated only once. For every result presented in this work, the same 6000 direct problem solutions were used.

Moreover, further investigations must continue in two main subdivisions: Validation of the proposed ANN model with real experimental data, and construction of a ANN model that considers the complete 2D transient thermography image as experimental data.

3 FUZZY LEVENBERG-MARQUARDT DAMPING FACTOR UPDATE STRATEGY AND TIKHONOV REGULARIZATION APPLIED TO A COUPLED CONDUCTION-RADIATION INVERSE HEAT TRANSFER PROBLEM

3.1 Introduction

Theoretical and experimental studies of participating media that interact with thermal radiation have a considerable range of investigations and applications in science and engineering. For instance, areas such as fire safety (57), dispersed media materials characterization (58, 59), oceanography (60), astronomy (61), are examples of works that consider this type of phenomenon. These are examples of studies that consider radiative transfer as the main form of energy transfer, which may be satisfactory, but sometimes, depending on the problem, conduction and convection mechanisms must be considered.

Physical models that consider combined conduction and radiation heat transfer have also a wide range of applications in science and engineering. For example, considering a solar energy engineering application, Mohan et al. (62) have shown that a conduction-radiation model was sufficient to describe the heat loss in Linear Fresnel Reactors. In bioengineering, Sukumar and Kar (63) used a coupled conduction-radiation model to study the freezing process in biological tissues. Kaemmerlen et al. (64) studied the properties of wood wool with potential applications in thermal insulation and cooling of buildings. Baillis and Sacadura (65) used the coupled conduction-radiation model to study the effect of temperature on the calculated emittance in order to test if the isothermal assumption was valid for an experimental set-up developed then.

In general, these technological applications involve research advances in three main different fronts: computational modeling techniques for the solution of the physical-mathematical problem; inverse problems formulation, solution methods, and analysis; and experimental data acquisition, analysis and manipulation. More often than not, these areas show a strong intercommunication, where an advance in one technique or technology leads to the development of the other.

Considering the progress in the field of computational techniques and solution methods applied to coupled conduction-radiation heat transfer inverse problems, the literature shows a variety of contributions. To name a few, in 1983 Sacadura and Al Abed

(66) used a Finite Element Monte Carlo method in order to solve a coupled conduction-radiation for both steady and transient states. Later, in 1993, Silva Neto and Özişik (3) solved an inverse problem of estimating the optical thickness, constant single scattering albedo and thermal conductivity. In 1996, Ruperti et al. (67) proposed an algorithm based on a space-marching method in order to solve an inverse conduction-radiation problem. In 1999, Li (68) solved a conduction-radiation problem and obtained estimates for the single scattering albedo, the optical thickness, the conduction-radiation parameter, and the scattering phase function. In 2007, Verma and Balaji (69) estimated the conduction-radiation parameter, the optical thickness and the boundary emissivity. They used Genetic Algorithms in order to solve the inverse problem, which are treated as a minimization problem. Two years later, Lobato et al. (70) used the Differential Evolution method to solve an inverse conduction-radiation problem employing a multi-objective function approach. Recently, in 2020, Jardim et al. (2) used the so called Topographical Global Optimization method to estimate thermal conductivity, single scattering albedo and optical thickness of a medium. The inverse conduction-radiation problem in question was studied with a sensitivity analysis and seven different cases with different noise levels, sensor positioning, and parameters values were presented.

Often, inverse radiative problems that estimate a space dependent scattering albedo do not consider the optical thickness as unknown. This is somewhat artificial, because as the scattering and absorption coefficients are unknown, the scattering albedo and the optical thickness should also be considered unknown (71). Stephany et al. (72) estimated the space dependant scattering albedo considering a radiative transfer problem, where they used the Ant Colony optimization method with a pre-regularization scheme. This method intended to assist the Ant Colony algorithm in order to only accept smooth solutions. Even though they did not consider the estimation of the optical thickness, the results obtained were robust and indicated the necessity to perform some regularization on the optimization search.

The main objective of the present study is to extend the work of Stephany et al. (72) by solving an inverse problem that deals with the simultaneous estimation of the space-dependant scattering albedo, conduction-radiation parameter and optical thickness. To perform this task, the classical least square minimization Levenberg-Marquardt (LM) method (73, 74) is used with the recently proposed fuzzy damping factor updating strategy.

This technique, proposed by Sajedi et al. (75), intends to assist the LM algorithm by using a Fuzzy Logic method that updates the LM damping factor based on the evolution of the objective function. With such method, these authors solved an inverse heat transfer problem addressed at a one-dimensional transient conduction problem, where different time dependent heat fluxes were estimated. Using this problem, they also investigated the convergence rate, stability and robustness of the Fuzzy LM algorithm (FLM).

Moreover, due to the variable scattering albedo function estimation problem, a strong ill-posedness in the solution is found, so a regularization technique must be employed. To overcome this problem, the Tikhonov Regularization (TR) (76) is used within the LM method in order to avoid oscillations on the sought function. As a secondary objective, this work presents, for the first time, the combined use of the Fuzzy LM Damping Factor Update Strategy and Tikhonov Regularization techniques.

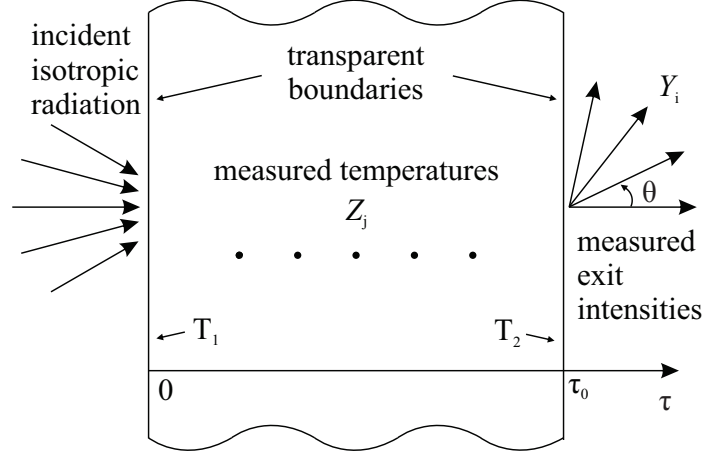
Two main test cases are presented, the first addresses an inverse problem involving only radiative transfer, as presented by Lobato et al. and Stephany et al. (71, 72). In this case only the single scattering albedo is estimated and the objective is to set a benchmark for the technique when used for different noise levels and TR parameters configurations. The second case addresses the complete inverse problem, combining radiation and conduction, for the estimation of the variable scattering albedo, the thermal conductivity and the optical thickness. In this case, the results obtained show how promising is the combination of the Fuzzy Method with the Tikhonov Regularization, demonstrating that with a few iterations and a reasonable initial guess, the method may be able to achieve good estimates for all sought unknowns.

3.2 Direct problem formulation and solution

Consider the one-dimensional medium represented in Figure 14. This medium is subjected to heat transfer by conduction and radiation, simultaneously. Moreover, this medium absorbs, emits and scatters isotropically the radiation, having a spatial coordinate $\tau = \int_0^x \beta dx$ and optical thickness $\tau_0 = \int_0^L \beta dx$, where β is the extinction coefficient, and L is the physical length of the medium, which has transparent boundaries and incident radiation at $\tau = 0$. At the boundaries $\tau = 0$ and $\tau = \tau_0$, temperatures are kept constant as T_1 and T_2 , respectively, as shown in Figure 14.

The mathematical formulation for the combined conduction-radiation heat transfer

Figure 14 – Schematic representation of the medium subjected to the coupled conduction-radiation heat transfer phenomenon (2, 3).



Source: Adapted from Silva Neto and Ozisik, 1993 (3).

problem is given by the Poisson Equation (77)

$$\frac{d^2\Theta}{d\tau^2} - \frac{[1 - \omega(\tau)]}{N} [\Theta^4 - G^*(\tau)] = 0, \text{ in } 0 < \tau < \tau_0 \quad (3.1a)$$

$$\Theta = \Theta_1 \text{ at } \tau = 0 \quad (3.1b)$$

$$\Theta = \Theta_2 \text{ at } \tau = \tau_0 \quad (3.1c)$$

where the dimensionless form of the spatially dependent temperature $T(\tau)$ is defined as

$$\Theta(\tau) = \frac{T(\tau)}{T_1} \quad (3.2)$$

and, moreover, $\omega(\tau)$ is the spatially dependent single scattering albedo, with dimensionless parameters defined as

$$G^*(\tau) = \frac{1}{2} \int_{-1}^1 I(\tau, \mu) d\mu \quad (3.3a)$$

$$N = \frac{k\beta}{4\psi^2\bar{\sigma}T_1^3} \quad (3.3b)$$

where G^* is the dimensionless incident radiation, N the conduction-radiation parameter, k is the thermal conductivity, ψ is the refraction index and $\bar{\sigma}$ is the Stefan-Boltzmann constant.

Neglecting the diffuse reflectivities at both the inner part of the boundary surfaces, and considering azimuthal symmetry, the interaction of the dimensionless radiation

intensity, $I(\tau, \mu)$, with the participating medium is formulated as the radiative transfer problem (77)

$$\mu \frac{\partial I(\tau, \mu)}{\partial \tau} + I(\tau, \mu) = R(\Theta) + \frac{\omega(\tau)}{2} \int_{-1}^1 I(\tau, \mu') d\mu' \text{ in } 0 < \tau < \tau_0, \quad -1 \leq \mu \leq 1 \quad (3.4a)$$

$$I(0, \mu) = A_1 \text{ with } \mu > 0 \quad (3.4b)$$

$$I(\tau_0, -\mu) = A_2 \text{ with } \mu > 0 \quad (3.4c)$$

where μ is the cosine of the polar angle θ , which is the angle between the τ coordinate with the radiation beam, and A_1 and A_2 are the external incident radiation at both boundaries. $R(\Theta)$ is the radiative emission term, which depends on the temperature of the medium and is formulated as

$$R(\Theta) = [1 - \omega(\tau)] \Theta^4(\tau) \quad (3.5)$$

The simultaneous conduction and radiation heat transfer direct problem is described by Eqs. 3.1 and 3.4. Its solution is obtained using Chandrasekhar's (78) discrete ordinates method where the angular domain is discretized and the integrals replaced by Gauss-Legendre quadratures, as performed by Jardim et al. (2) and Knupp et al. (79).

The built-in ‘‘NDSolve’’ routine of the Wolfram Mathematica 11.0 software (80) is used to solve the system of coupled differential equations generated by the discretization of the polar angle in Eq. 3.4a. This routine is performed under automatic absolute and relative error control, therefore the mesh used is automatically selected by the routine. The conduction problem given by Eq. 3.1a is also solved with ‘‘NDSolve’’ routine, with the same automatic error and mesh control, but for the sake of stability, a pseudo-transient regime is employed.

A similar solution approach was presented by Knupp et al. (81), where a radiative transfer problem was solved. Differently, in the present work, the heat conduction phenomenon is also considered and the iterative process is constructed around these coupled equations: the conduction problem uses information of the radiation intensity through the term G^* and the radiation problem requires information of the temperature in the dimensionless quantity R . The iterative process is constructed by giving an initial

solution to the radiation intensity so the quantity G^* can be calculated. Next, it is possible to obtain the temperature profile and calculate R . That ends the iteration because this R generates a new radiation intensity profile and the process restarts. This method is considered converged when the maximum absolute error between two radiation intensity profiles in consecutive iterations is below some pre-defined tolerance.

3.3 Inverse problem formulation and solution

Consider that some thermal and radiative properties of the medium are unknown. The inverse problem consists of obtaining estimates of these properties based on experimental data of temperature and radiation acquired at different positions and polar angles. In this work the thermal conductivity k , the space dependent single scattering albedo $\omega(\tau)$ and the optical thickness τ_0 are considered unknowns, leading to the following vector of unknowns:

$$\mathbf{P} = \{\omega_1, \omega_2, \dots, \omega_K, N, \tau_0\}^T \quad (3.6)$$

where the thermal conductivity k is included in the formulation of the conduction-radiation dimensionless parameter N - see Eq. 3.3b. The single scattering albedo is formulated with discrete points $\omega_1, \omega_2, \dots, \omega_K$ with a linear interpolation in order to generate the continuous function $\omega(\tau)$, where K is the total number of points used.

In this work the experimental data are simulated using the solution of the direct problem itself. This solution yields two physical observable quantities, the radiation intensity I and the dimensionless temperature Θ , and, in order to generate the simulated experimental data, random noise drawn from a normal distribution are added to the exact solution, as follows

$$Y_i = I_i(\mathbf{P}_{\text{exact}}) + e_i, \quad e_i \sim \mathcal{N}(0, \sigma_{\text{exp}}^2), \quad i = 1, 2, \dots, D_{\text{Rad}} \quad (3.7a)$$

$$Z_j = \Theta_j(\mathbf{P}_{\text{exact}}) + r_j, \quad r_j \sim \mathcal{N}(0, \sigma_{\text{exp}}^2), \quad j = 1, 2, \dots, D_{\text{Temp}} \quad (3.7b)$$

where D_{Rad} and D_{Temp} are the total number of radiation intensity and temperature experimental data, respectively. It is possible to notice that the variance has the same

value for the radiation intensity and for the temperature. This choice was based on the fact that both quantities are dimensionless, and their magnitude lies within a similar range.

Considering the maximum likelihood approach, the inverse problem may be formulated as an optimization problem, where the following least square objective function must be minimized (3):

$$Q(\mathbf{P}) = \sum_{i=1}^{D_{\text{Rad}}} [Y_i - I_i(\mathbf{P})]^2 + \sum_{j=1}^{D_{\text{Temp}}} [Z_j - \Theta_j(\mathbf{P})]^2 = \mathbf{R}_I^T \mathbf{R}_I + \mathbf{R}_\Theta^T \mathbf{R}_\Theta \quad (3.8)$$

where \mathbf{R}_I and \mathbf{R}_Θ are residue vectors, which contain the difference between experimental and calculated data, for both the D_{Rad} radiation and D_{Rad} temperature measurements, respectively.

The solution of the objective function proposed by Eq. 3.8 may lead to an ill-posed problem, specially when one intends to estimate intrinsic functions of the model in question, which is the case of the present work with the spatially dependent single scattering albedo $\omega(\tau)$. This ill-posedness yields heavy oscillations in the obtained solutions, generating no useful information on the sought function.

The Tikhonov Regularization (TR) technique is often used to overcome this problem by adding a term to the objective function Q that penalizes oscillating solutions of \mathbf{P} . The modified Eq. 3.8 with the regularization term is written as

$$Q_{\text{TR}}(\mathbf{P}) = \mathbf{R}_I^T \mathbf{R}_I + \mathbf{R}_\Theta^T \mathbf{R}_\Theta + \alpha \|\mathbf{L}\mathbf{P}\|^2 \quad (3.9)$$

where $\|\cdot\|$ is the l_2 Euclidean norm, α is the regularization parameters that controls the amount of regularization necessary to solve the problem, and \mathbf{L} is a derivative operator matrix.

The matrix \mathbf{L} can be of zero, first or second order, which is a choice made considering aspects of the problem. The regularization parameter α is critical to obtain a useful solution \mathbf{P} : if α is too large, too much regularization is present leading to a constant solution, on the other hand, if α is small, no regularization is performed, and the solution oscillates. Different methods were proposed in order to obtain the optimal value of α , such as the L-curve (82, 83), Fixed Point Iteration (84), Morozov Discrepancy Principle (85), and others. Besides that, since the choice of α is not the focus of this work, its value is obtained

through trials and tests, and then kept fixed for every result presented. It is necessary to stress that the use of a proven method to choose α is always preferred in order to avoid bias.

3.3.1 Classical Levenberg-Marquardt with Tikhonov Regularization

The classical Levenberg-Marquardt algorithm is a gradient based optimization method intended to minimize least squares functionals. It was first proposed by Levenberg (73) later being rediscovered by Marquardt (74), which contributed to increase the chances of convergence of the method.

Considering the TR functional presented in Eq. 3.9, the iterative process to minimize such objective function is built with steps in the direction of $\Delta\mathbf{P}$, that is

$$\mathbf{P}_{\text{new}} = \mathbf{P}_{\text{old}} + \Delta\mathbf{P} \quad (3.10)$$

where the subscripts “new” and “old” mean the next and present iteration, respectively. The direction $\Delta\mathbf{P}$ is obtained with (86)

$$\Delta\mathbf{P} = - [\mathbf{J}_I^T \mathbf{J}_I + \mathbf{J}_\Theta^T \mathbf{J}_\Theta + \lambda \mathbf{I} + \alpha (\mathbf{L}^T \mathbf{L})]^{-1} \times [(\mathbf{J}_I^T \mathbf{R}_I + \mathbf{J}_\Theta^T \mathbf{R}_\Theta) + \alpha (\mathbf{L}^T \mathbf{L}) (\mathbf{P} - \mathbf{P}_0)] \quad (3.11)$$

where λ is the LM damping factor, \mathbf{I} is an identity matrix with the same dimension of \mathbf{P} , α and \mathbf{L} are the already defined TR parameter and derivative matrix, respectively, \mathbf{P}_0 is the best known *a priori* information of the solution \mathbf{P} , and \mathbf{J}_I and \mathbf{J}_Θ are the Jacobian matrices for the radiation intensity and temperature, respectively, with respect to the unknown parameters \mathbf{P} , i.e.

$$J_{I(i,j)} = \frac{\partial I_i}{\partial P_j} \text{ with } i = 1, 2, \dots, D_{\text{Rad}} \text{ and } j = 1, 2, \dots, N_P \quad (3.12a)$$

$$J_{\Theta(i,j)} = \frac{\partial \Theta_i}{\partial P_j} \text{ with } i = 1, 2, \dots, D_{\text{Temp}} \text{ and } j = 1, 2, \dots, N_P \quad (3.12b)$$

where N_P is the total number of unknown parameters \mathbf{P} . The derivatives of Eq. 3.12 are obtained with a central finite difference approximation, where a three-point formulation is

Algorithm 1: Levenberg-Marquardt Algorithm for minimization

choose: initial point \mathbf{P}_{old} , initial μ and stopping criterion

$S_{\text{old}} \leftarrow Q_{\text{TR}}(\mathbf{P}_{\text{old}})$

While Stopping Criterion = False **do:**

Evaluate \mathbf{J}_I and \mathbf{J}_Θ , for \mathbf{P}_{old}

Evaluate $\Delta\mathbf{P}$ with Eq. 3.11

$\mathbf{P}_{\text{new}} \leftarrow \mathbf{P}_{\text{old}} + \Delta\mathbf{P}$

$S_{\text{new}} \leftarrow Q_{\text{TR}}(\mathbf{P}_{\text{new}})$

If $S_{\text{new}} < S_{\text{old}}$ **Then** $\lambda \leftarrow \lambda/10$ **Else** $\lambda \leftarrow \lambda \times 10$

$S_{\text{old}} \leftarrow S_{\text{new}}$

$\mathbf{P}_{\text{old}} \leftarrow \mathbf{P}_{\text{new}}$

end While

\mathbf{P}_{new} is the solution

used and a fixed increment is chosen for every derivative.

The LM damping factor parameter λ controls how much “refined” is the search in the direction $\Delta\mathbf{P}$: if its value is relatively high, the search has smaller steps, which is acceptable for poor values of \mathbf{P} , but if its value tends to zero, the search will favor convergence, which is ideal for better estimates of \mathbf{P} . In classical algorithms, this parameter is updated by a factor of 10 when the objective function improves and by a factor of 0.1 otherwise. This approach influences directly the computational cost and convergence of the search. Algorithm 1 presented the classical LM search used in this work. The stopping criterion chosen will be discussed later, where the importance of this choice will be highlighted.

Implementation Tip 1 The order of the difference operation for calculating \mathbf{R}_I and \mathbf{R}_Θ matters. With the presented formulation, the correct order is: the calculated I or Θ quantity minus the experimental data. The contrary is possible, but the minus sign in Eq. 3.11 would change to positive.

Implementation Tip 2 The Jacobian matrices can be joined together with an “Append” operation. It is only necessary to keep in mind that both \mathbf{R}_I and \mathbf{R}_Θ should also be joined and the order must be the same as the joined Jacobians.

3.3.2 Fuzzy Levenberg-Marquardt

In this version of the LM algorithm, proposed by Sajedi et al. (75), the damping factor is updated through a fuzzy scheme. This modification intends to improve convergence and efficiency of the search in comparison to classical LM. More specifically, the input of

the fuzzy system is a relative error evolution for the objective function, namely “Percent Error”, and is calculated for every iteration as

$$\text{PE} = 100 \times \frac{S_{\text{new}} - S_{\text{old}}}{S_{\text{old}}} \quad (3.13)$$

where S_{new} and S_{old} are the new and current objective function values. Briefly, if $\text{PE} < 0$, S is improving; if $\text{PE} \approx 0$, S is converging; if $\text{PE} > 0$, S is getting worse.

Degrees of membership are then associated to the input PE, as presented in Figure 15, where NLR, NL, NM, NS, Z, PS, PM, PL, and PLR mean larger negative, large negative, medium negative, small negative, zero, small positive, medium positive, large positive, and larger positive, respectively.

The output of the fuzzy is the damping factor λ and its membership function is presented in Figure 16. In such figure, the terms VS, S, SS, LM, M, UM, SL, L, and VL mean very small, small, slightly small, lesser medium, medium, more medium, slightly large, large, and very large, respectively.

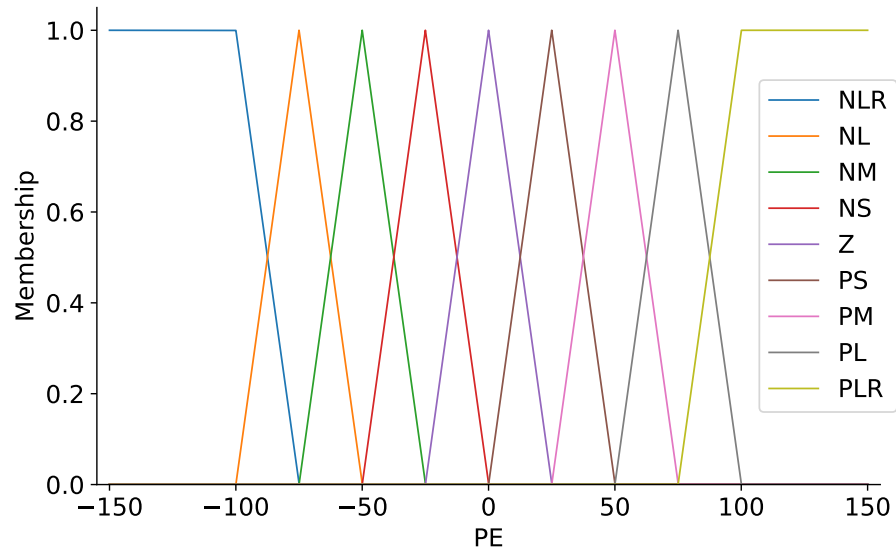
Then, the fuzzy system is constructed with the following rules:

- If PE is NLR then λ is M.
- If PE is NL then λ is LM.
- If PE is NM then λ is SS.
- If PE is NS then λ is S.
- If PE is Z then λ is VS.
- If PE is PS then λ is UM.
- If PE is PM then λ is SL.
- If PE is PL then λ is L.
- If PE is PLR then λ is VL.

Finally, the defuzzification can be performed by different methods, and in this work the centroid technique was chosen. In order to build the algorithm, the complete calculation of the fuzzy system that yields the updated value of λ is represented by the term \mathcal{F} , being $\mathcal{F}(\text{PE})$ the fuzzy function evaluated for the PE value.

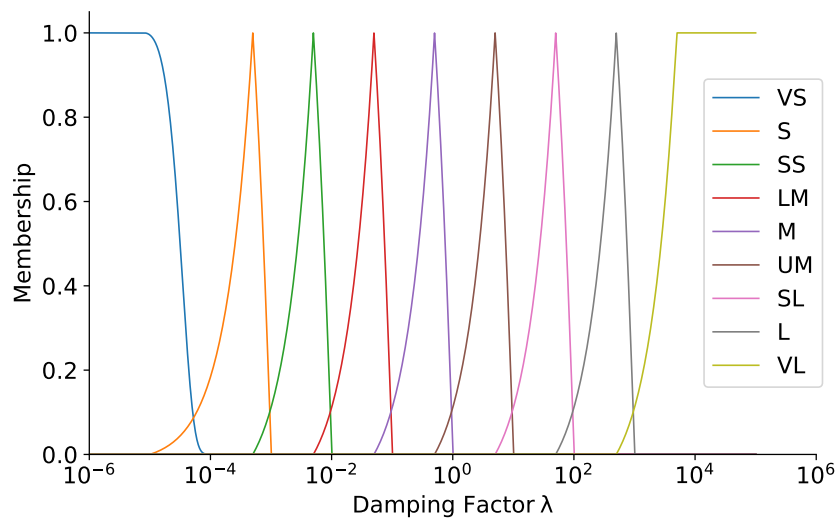
Algorithm 2 presents the pseudo-code for the FLM method. It is possible to observe that both Algorithms 1 and 2 are very similar, where the main difference between them is the λ updating approach. Despite this similarity, modifying the updating choice of λ may have a great impact in improving the convergence of the method.

Figure 15 – Memberships of the fuzzy system input PE.



Source: Adapted from Sajedi et al., 2021 (75).

Figure 16 – Memberships of the fuzzy system output λ .



Source: Adapted from Sajedi et al., 2021 (75).

Algorithm 2: Fuzzy Levenberg-Marquardt for minimization

choose: initial point \mathbf{P}_{old} , initial λ and stopping criterion

 $S_{\text{old}} \leftarrow Q_{\text{TR}}(\mathbf{P}_{\text{old}})$
While Stopping Criterion = False **do:**

 Evaluate \mathbf{J}_I and \mathbf{J}_Θ , for \mathbf{P}_{old}

 Evaluate $\Delta\mathbf{P}$ with Eq. 3.11

 $\mathbf{P}_{\text{new}} \leftarrow \mathbf{P}_{\text{old}} + \Delta\mathbf{P}$

 $S_{\text{new}} \leftarrow Q_{\text{TR}}(\mathbf{P}_{\text{new}})$

 $\text{PE} \leftarrow 100 \times (S_{\text{new}} - S_{\text{old}})/S_{\text{old}}$

 $\lambda \leftarrow \mathcal{F}(\text{PE})$

 $S_{\text{old}} \leftarrow S_{\text{new}}$

 $\mathbf{P}_{\text{old}} \leftarrow \mathbf{P}_{\text{new}}$
end While
 \mathbf{P}_{new} is the solution

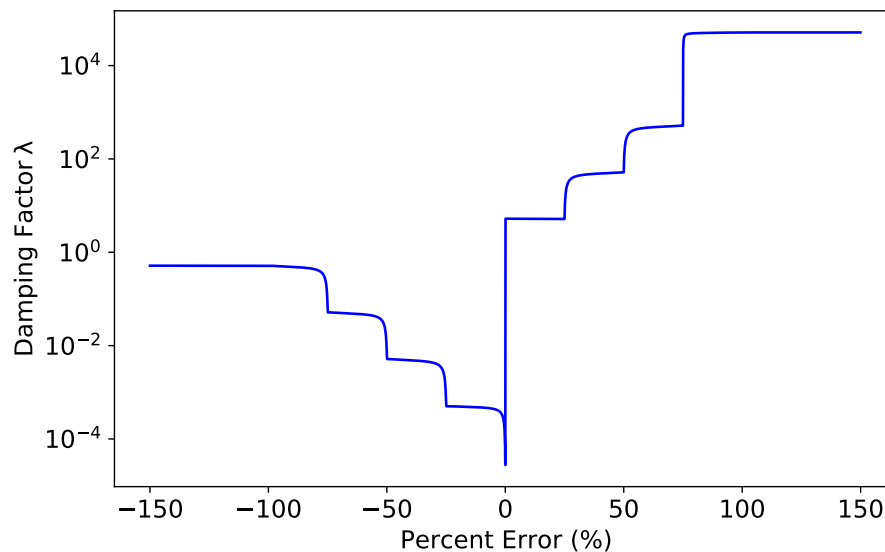
3.4 Results and discussion

In order to compute the fuzzy system, the “skfuzzy” package from Python 3.9 language is used. In this package, the PE input domain is inserted as discrete points, ranging linearly from -150% to 150% with steps of 0.01%. The same must be done for the λ output domain, where 30001 points with a base 10 logarithmic spacing are used, ranging from 10^{-6} to 10^6 . This logarithmic spacing is necessary due to the large range of possible values for the damping factor λ . For both the input and output, the final membership functions are triangular for the interior values, and trapezoidal for the boundary values, as already presented in Figure 15 and Figure 16. It must be noted that, in Figure 16, the logarithmic scale of the λ axis yields a non-triangular shape of the membership functions, which is just a matter of visualization.

Fuzzy System Visualization. To better visualize the Fuzzy System behavior, Figure 17 shows the complete PE input space for its respective λ output. It is possible to see that λ have a step behavior with range of $10^{-5} \leq \lambda \leq 10^0$ for $-150 \leq \text{PE} < 0$, $10^0 < \lambda \leq 10^5$ for $0 < \text{PE} \leq 0$ where the lowest value possible is obtained for $\text{PE} = 0.0$, which is desirable, meaning that convergence was reached. More specifically, this minimum value obtained for λ is $\mathcal{F}(\text{PE} = 0.0) = 2.819902(10^{-5})$

Stopping Criterion. The chosen condition to perform the iterative process of the “while” loop in Algorithms 1 and 2 is $|\text{PE}| > 0.1\%$. That is, while the absolute value of the Percent Error is larger than 0.1%, the argument inside of the loop is performed.

Test Cases Summary. In this work, two main test cases are presented. In the

Figure 17 – Complete PE input vs. λ output of the fuzzy system.

Source: The author, 2023.

first one, only the variable scattering albedo $\omega(\tau)$ is estimated, as performed by Stephany et al. (72): this case considers only the radiative transfer problem, i.e., the conduction N is relatively high and there is no temperature gradient. This first test case is used to compare the performance of both the classical LM and FLM algorithms. In the second one, in addition to $\omega(\tau)$, the thermal conductivity N and optical thickness τ_0 are simultaneously estimated considering the complete conduction-radiation heat transfer problem. This test case is subdivided in three subcases, where different variations of $\omega(\tau)$ are tested.

Experimental Data. For Cases 1 and 2, experimental data are generated with a noise level of $\sigma_{\text{exp}} = 0.01$ - see Eq. 3.7. For Test Case 1, the exact single scattering albedo used is the polynomial expansion $\omega(\tau) = 0.2 + 0.2\tau + 0.6\tau^2$, and for Test Case 2, three different $\omega(\tau)$ are tested: constant, linear and parabolic. Other parameters to simulate the experimental data are presented in Table 9. The radiative properties and conditions presented in such table are the same from the ones used by Ref. (72), with exception of the ones used for the heat conduction problem. The radiation intensity measurements are acquired at $\tau = 0$ for the polar angles corresponding to cosines from $\mu = -0.8$ to $\mu = -0.1$ with steps of $\Delta\mu = 0.05$, and at $\tau = \tau_0$ from $\mu = 0.1$ to $\mu = 0.8$ with the same step size. Temperature readings are obtained from 0.2τ to 0.8τ with steps of 0.1τ . Briefly, there are radiation measurements at both boundaries, and temperature readings inside the medium.

Table 9 – Summary of the parameters to simulate the experimental data set

Parameter	Description	Comments
$A_1 = 1.0$	Incident Radiation at $\tau = 0$	Known
$A_2 = 0.0$	Incident Radiation at $\tau = \tau_0$	Known
$N = 0.05$	Conduction-Radiation Parameter	Unknown for Case 2
$\tau_0 = 1.0$	Optical Thickness	Unknown for Case 2
$\Theta_1 = 1.0$	Dimensionless Temperature at $\tau = 0$	N.A. for Case 1
$\Theta_2 = 0.2$	Dimensionless Temperature at $\tau = \tau_0$	N.A. for Case 1
$\sigma_{\text{exp}} = 0.01$	Noise standard deviation (Eq. 3.7)	
$K = 10$	Number of points to represent $\omega(\tau)$	
$N_T = 7$	Number of temperatura data	
$N_R = 30$	Number of radiation intensity data	

Source: The author, 2023.

3.4.1 Test Case 1

The main objective of this Test Case is to assess the performance of the LM and FLM algorithms by comparing the number of iterations necessary to achieve the stopping criterion, and by comparing the quality of the solutions obtained, which is analyzed by means of the objective function value and the error norm between the exact and estimated solution ω_{error} , that is

$$\omega_{\text{error}} = \|\omega_{\text{exact}} - \omega_{\text{estimated}}\| \quad (3.14)$$

where ω_{exact} is the vector of exact values of $\omega(\tau)$ obtained at the same points as the discretized variable.

As a secondary objective of the present Case, several regularization parameters are tested in order to obtain a good approximation for the optimal value for it. This is performed by testing different values of α for different values of noise levels σ_{exp} .

As already described, this case considers only the radiative transfer problem, and the unknown considered is the scattering albedo $\omega(\tau)$, which is represented by $K = 10$ discrete points. The initial solution for every execution of this case is $\omega_i = 0.5$ for $i = 1, 2, \dots, 10$, and the initial damping factor λ for both methods is set as 10. The *a priori* state vector \mathbf{P}_0 considered is completely zero for its elements, being the most uninformative vector possible. It is important to notice that \mathbf{P}_0 is a fixed vector and it is not correlated with the initial solution of ω . To perform the Tikhonov Regularization, different values of α are

tested, ranging from $\alpha = 0.005$ and $\alpha = 0.020$. The Tikhonov Regularization derivative operator \mathbf{L} is chosen as a first order differential operator in Eqs. 3.9 and 3.11, i.e., when multiplied by \mathbf{P} , it yields another vector containing the numerical first derivatives of \mathbf{P} .

Table 10 presents the results of Test Case 1 for different noise levels σ_{exp} and regularization parameters α . In such table, $Q(\mathbf{P})$ is the objective function value Eq. 3.8, and the term “IT” is the number of iterations needed to reach the stopping criterion. It is possible to see that, although the results are very similar for both the LM and FLM methods, every experiment led to less iterations needed by the latter.

The reader may notice that the value of the objective function $Q(\mathbf{P})$ presented is not the lowest for the best values of ω . This occurs because the displayed objective function value is $Q(\mathbf{P})$, which represents a measure of the fitting between the experimental data and the model. The actual objective function being minimized is $Q_{TR}(\mathbf{P})$, presented in Eq. 3.9 and, when the stopping criterion is reached, it may not yield the best fitting between experimental data and the model, due to the regularization portion of the function.

For every σ_{exp} results presented, it is possible to see the total number of iterations needed to obtain the different α values. These results indicate that the FLM is more suitable to be used in methods to obtain the best Tikhonov parameter, due to its efficiency. For instance, with $\sigma_{\text{exp}} = 0.010$, four values of α were tested leading to a total difference of 4 iterations. This difference can grow considerably when more robust methods, such as the L-curve, are used to obtain the best α , as they require the calculation of many inverse problem solutions.

3.4.2 Test Case 2

In this Case, the coupled conduction-radiation problem is considered, where the main objective is to simultaneously estimate the variable scattering albedo $\omega(\tau)$, the thermal conductivity represented by the parameter N and the optical thickness τ_0 . This is performed using the FLM method and by five numerical experiments presented in Tabs. Table 11, Table 12, and Table 13, for the three subcases tested, respectively. In these tables, a noise level of $\sigma_{\text{exp}} = 0.01$ and regularization parameter $\alpha = 0.01$ are used, which are values that generated reasonable results in Test Case 1 - see Table 10. Moreover, every Execution (“Exec.” column) have a different experimental data set and FLM starting point, which is randomly generated in the range $0.005 \leq N \leq 0.5$ and $0.25 \leq \tau_0 \leq 2.5$

Table 10 – Results for Test Case 1

σ_{exp}	α	LM			FLM		
		$Q(\mathbf{P})$	ω_{error}	IT	$Q(\mathbf{P})$	ω_{error}	IT
0.000	0.005	0.0000206	0.106757	7	0.0000206	0.106956	6
	0.010	0.0000468	0.128737	7	0.0000474	0.129334	5
	0.015	0.0000772	0.144170	6	0.0000770	0.144147	5
	0.020	0.0001085	0.155430	6	0.0001085	0.155422	5
Total				26	21		
0.010	0.005	0.0031084	0.147349	6	0.0031083	0.147118	5
	0.010	0.0031308	0.153546	6	0.0031308	0.153806	5
	0.015	0.0031589	0.162649	6	0.0031586	0.162280	5
	0.020	0.0031898	0.170580	6	0.0031903	0.170228	5
Total				24	20		
0.020	0.005	0.0103297	0.334486	6	0.0103295	0.334416	5
	0.010	0.0105815	0.314535	6	0.0105815	0.314480	5
	0.015	0.0107190	0.311427	6	0.0107189	0.311279	5
	0.020	0.0108118	0.309823	6	0.0108118	0.309728	5
Total				24	20		

Source: The author, 2023.

(initial ω points are the same as Test Case 1, i.e., $\omega_i = 0.5$ for $i = 1, 2, \dots, 10$)

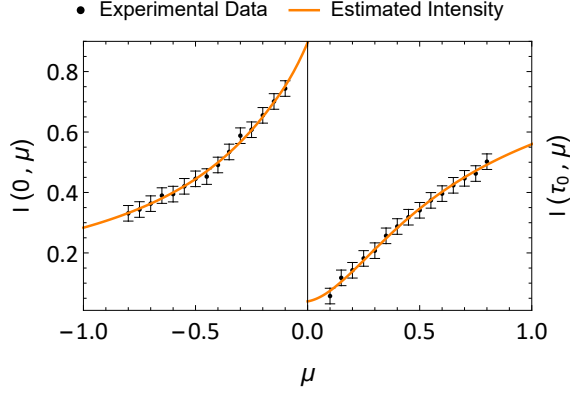
3.4.2.1 Test Case 2A: Constant $\omega(\tau)$

The first subcase deals with a constant scattering albedo, with exact value of $\omega(\tau) = 0.3$. Results presented in Table 11 show that Execution #3 got a completely wrong conduction-radiation parameter N , generating also a relative larger error ω_{error} . Nevertheless, in such execution the optical thickness τ_0 got a good approximation to the exact value $\tau_0 = 1.0$. Although the best objective function value $Q(\mathbf{P})$ is obtained for Exec. #5, the best two ω_{error} can be found for Execs. #1 and #4. This fact can be explained by the random nature of the experimental data. The wrong result in Exec. #3 occurs by a convergence problem, where LM got stuck in a local minimum, which is not the expected solution. This is a common problem to the LM method when initialized with poor initial solutions. A possible way of overcoming this problem is to employ a stochastic global search before employing the LM algorithm, such as the Differential Evolution, Luus-Jaakola or any other global optimization method.

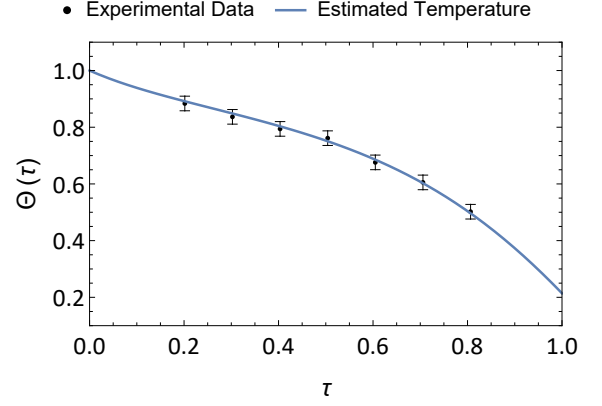
Figure 18 shows the fit between experimental data and the direct problem evaluation for both the (a) Radiation Intensity and (b) Dimensionless Temperature, generated by the

Figure 18 – Comparison among values of the Radiation Intensity, Temperature, and their experimental data obtained for Exec. #5 (Case 2A).

(a) Estimated Radiation Intensity from Exec. #5 vs. Experimental data



(b) Estimated Temperature from Exec. #5 vs. Experimental data



Source: The author, 2023.

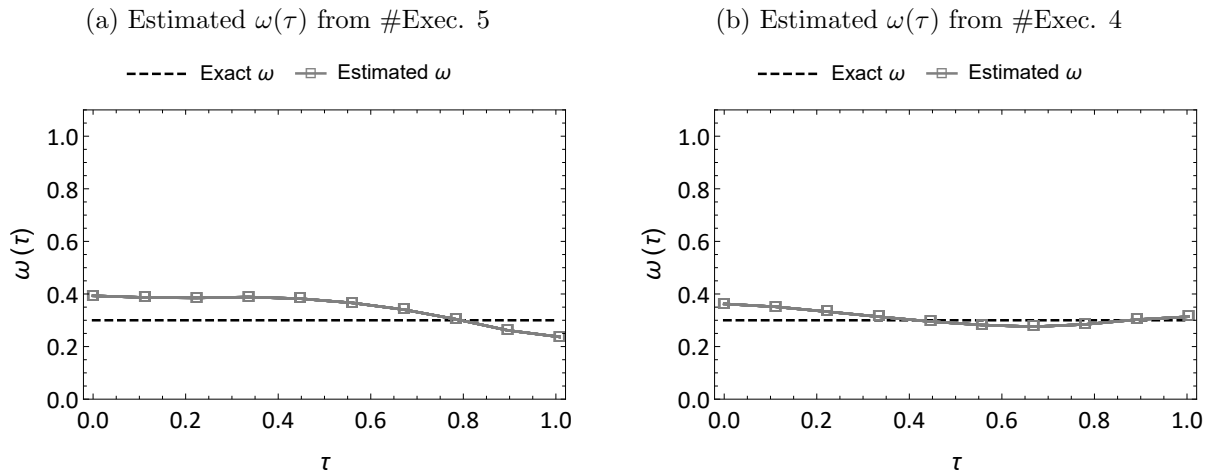
parameters obtained from Exec. #5 (see Table 11). The error bars presented represent a interval of $\pm 2.576\sigma_{\text{exp}}$. The reader may notice that, even though this only execution generated a somewhat poor fit for $\omega(\tau)$ in comparison to the one obtained in Exec. #4, the fit to the experimental data is excellent.

In Figure 19 it is possible to see a comparison between retrieved scattering albedo for Execs. #4 and #5, which generated the lowest ω_{error} and lowest $Q(\mathbf{P})$, respectively. Those two images show the importance of the regularization, i.e., the task of estimating a constant line seems trivial, but even with a proper regularization, some oscillations can be found around the exact value.

Table 11 – Results for Test Case 2A

Exec.	ω_{error}	N	τ_0	$Q(\mathbf{P})$
#1	0.138217	0.0559376	0.994548	0.00319204
#2	0.226018	0.049114	0.999596	0.00389724
#3	1.12332	2.2441	1.0331	0.116122
#4	0.0955803	0.049605	1.00341	0.00284022
#5	0.222445	0.0465192	1.00807	0.00251934

Source: The author, 2023.

Figure 19 – Comparison of estimated ω for (a) Exec. #5 and (b) Exec #4.

Source: The author, 2023.

3.4.2.2 Test Case 2B: Linear $\omega(\tau)$

For this subcase, the linear $\omega(\tau) = 0.9 - 0.6\tau$ is considered. Table 12 presents the obtained results. For the five computational experiments presented, no wrong values for N were obtained. The best solution was obtained for Exec. #5, but considering variations in the experimental data set, one can say that every solution obtained generated good approximations to the measurements.

The fit between experimental data and the calculated direct problem (radiation intensity and dimensionless temperature) are presented in Figure 20 for Exec. #5, where an excellent fit can be seen. Similar to Test Case 2A, the best $Q(\mathbf{P})$ did not yielded the best ω_{error} , which was observed in Exec. #1. In Figure 21 both the $\omega(\tau)$ obtained from Exec. #5 and #1 are presented. It is possible to see that both estimated ω functions represent reasonably good approximations to the exact function, even though some slight oscillation can still be found. This may be corrected by considering a finer adjustment for the Tikhonov Regularization parameter α .

3.4.2.3 Test Case 2C: Parabolic $\omega(\tau)$

Results presented in Table 13 show good approximations for every execution, with exception of Exec. #4, which led to wrong value of N . Indeed, this conduction-radiation parameter is difficult to estimate in certain ranges of values. Moreover, when the starting

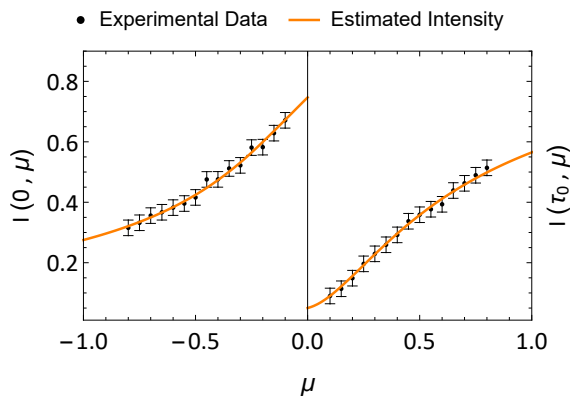
Table 12 – Results for Test Case 2b

Exec.	ω_{error}	N	τ_0	$Q(\mathbf{P})$
#1	0.140365	0.0508578	1.0002	0.00332959
#2	0.164826	0.0521814	1.00647	0.00398747
#3	0.339735	0.0555154	1.00043	0.00483613
#4	0.220589	0.0532661	0.999018	0.00338912
#5	0.225853	0.0465025	1.00216	0.00306238

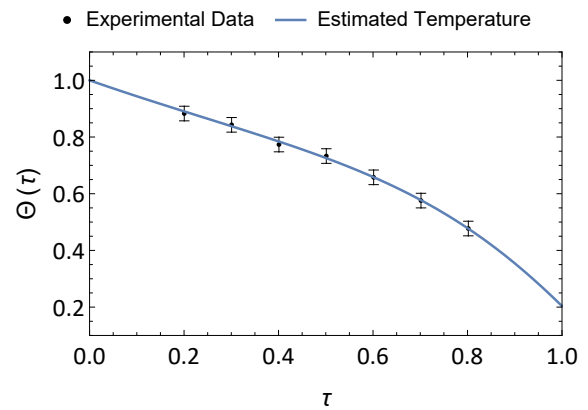
Source: The author, 2023.

Figure 20 – Comparison among values of the Radiation Intensity, Temperature, and their experimental data obtained for Exec. #5 (Case 2B).

(a) Estimated Radiation Intensity from Exec. #5 vs. Experimental data



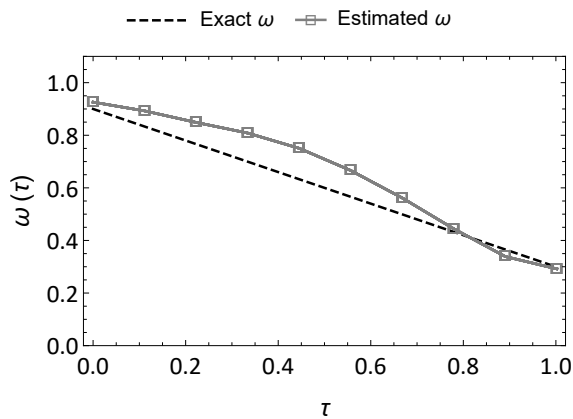
(b) Estimated Temperature from Exec. #5 vs. Experimental data



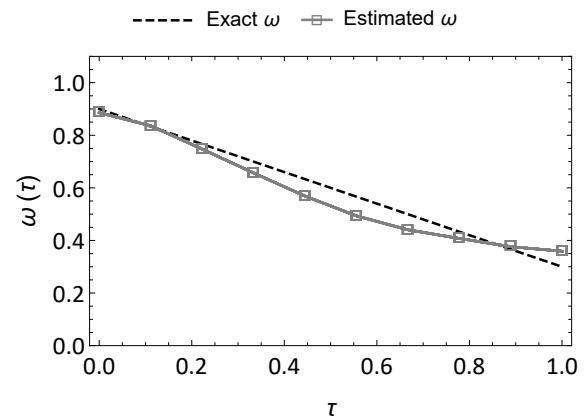
Source: The author, 2023.

Figure 21 – Comparison of estimated ω for (a) Exec. #5 and (b) Exec #1.

(a) Estimated $\omega(\tau)$ from #Exec. 5



(b) Estimated $\omega(\tau)$ from #Exec. 1



Source: The author, 2023.

Table 13 – Results for Test Case 2c

Exec.	ω_{error}	N	τ_0	$Q(\mathbf{P})$
#1	0.147111	0.0510206	1.00546	0.00326721
#2	0.16676	0.0490335	0.994301	0.00430255
#3	0.167729	0.0490189	0.994326	0.00430304
#4	0.640011	2.02078	1.01019	0.126096
#5	0.256811	0.0461	1.01504	0.00189667

Source: The author, 2023.

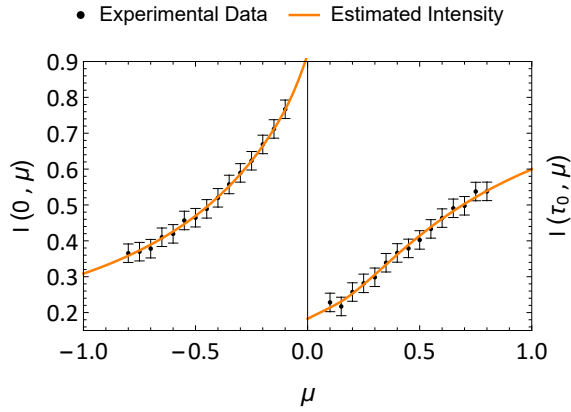
value of N is a relative large value, the conduction problem is completely vanished, and there is almost no sensitivity. On the other hand, τ_0 is the most robust parameter to estimate of such problem. See that even the wrong solution for N and a bad estimation of ω in Exec. #4 led to a good approximation of $\tau_0 = 1.01019$.

Figure 22 presents the fit between experimental data and the direct problem solution - parameters from Exec. #5 (see Table 13). The error bars presented represent a interval of $\pm 2.576\sigma_{\text{exp}}$. Again, an excellent fit between model and experimental data is found, corroborating to the robustness of the FLM method.

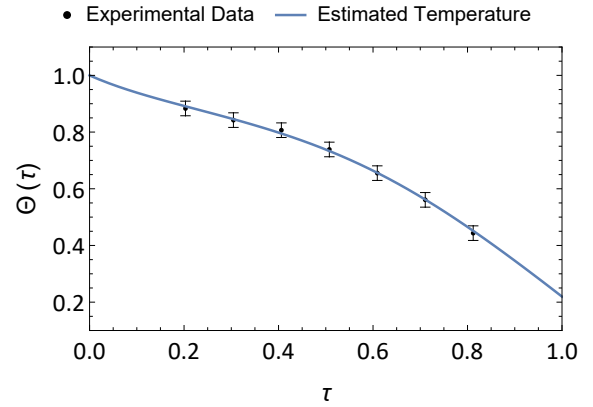
The estimation of $\omega(\tau)$ is presented in Figure 23. This is the result obtained from Exec. #5 (Figure 23a), which generated the lowest value of $Q(\mathbf{P})$, and the one from Exec. #1 (Figure 23b), which generated the best ω_{error} . In such figures it is possible to see a good approximation between exact and estimated values, specially from Exec. #1, but to consider the best fit for the sought function is somewhat artificial, for that reason, the best experimental data fit from Exec. #1 is considered as the best solution.

Figure 22 – Comparison among values of the Radiation Intensity, Temperature, and their experimental data obtained for Exec. #5 (Case 2C).

(a) Estimated Radiation Intensity from Exec. #5 vs. Experimental data



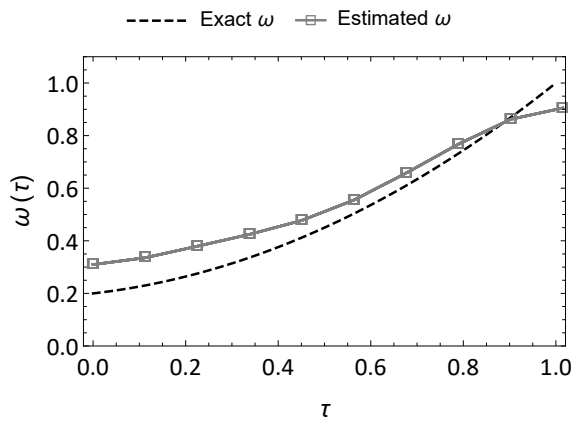
(b) Estimated Temperature from Exec. #5 vs. Experimental data



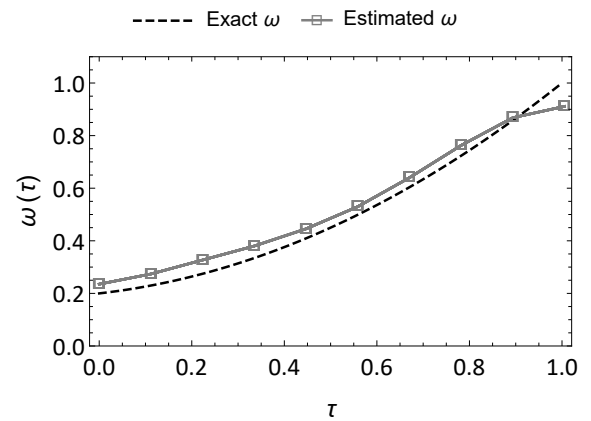
Source: The author, 2023.

Figure 23 – Comparison of estimated ω for (a) Exec. #5 and (b) Exec #1.

(a) Estimated $\omega(\tau)$ from #Exec. 5



(b) Estimated $\omega(\tau)$ from #Exec. 1



Source: The author, 2023.

3.5 Conclusions

An inverse problem of simultaneous radiation and conduction heat transfer was solved using the recently proposed Fuzzy Levenberg-Marquardt Damping Factor Update technique. The physical problem considered is a one dimensional, steady state, participating medium, subjected to heat transfer by conduction and radiation, simultaneously. The inverse problem dealt with the estimation of properties such as space-dependent scattering albedo, conduction-radiation parameter, and optical thickness. Results shows that the technique employed has good convergence capabilities, where a more efficient search was seen in comparisson to classical LM. Moreover, considering that this FLM is still a gradient based method that is indicated to perform local searches, the results obtained are fairly good since no global search were performed beforehand. This work also highlights the importance of the regularization technique used, which may be mandatory to obtain useful estimations of the sought function. Finally, future investigations may take three possible approaches: the use of an automatic method to determine the best TR parameter along with the FLM algorithm; the use the present technique for problems considering function estimation in two- and three-dimensional problems, which leads to increasing challenge in terms of computational cost and regularization; and solution of different types of inverse problems in order to compare the search performance of LM and FLM, drawing more robust conclusions of advantages of one method over the other.

4 PERFORMANCE ANALYSIS OF THE TOPOGRAPHICAL GLOBAL OPTIMIZATION IN INVERSE HEAT TRANSFER PROBLEMS

4.1 Introduction and background

Often entire engineering systems are based on the fundamental principles of heat transfer and diffusion. At other times, the analysis of such principles remains crucial for understanding the proper behaving of such systems. Considering the significant influence that this phenomenon has on the energy efficiency of various types of systems and processes, the scientific community has, and continues to, employ efforts in the design of increasingly efficient and robust computational methods to assist the analysis of this phenomenon.

The estimation of thermophysical material properties and conditions acting in a system is crucial in Heat Transfer Engineering. This can be achieved by formulating and solving an Inverse Heat Transfer Problems (IHTPs), which can be treated as optimization problems when using the maximum likelihood approach (6, 87, 88). To solve IHTPs, several optimization methods have been employed to achieve state-of-the-art results. Among these methods, clustering optimization methods are noteworthy because they tend to choose the best-suited points from a set of sampled points in a search space to initialize a local search. This choice is made to prevent repeated discovery of the same optimum, thereby avoiding unnecessary computational costs. Moreover, the core of these methods usually relies on non-iterative procedures (89, 90), which can be of great benefit for multi-core programming.

With that in mind, the main objective of this work is to evaluate the performance of the clustering optimization method known as Topographical Global Optimization (TGO) for the solution of IHTPs. TGO was developed by Törn (91), having its first formal publications as the Master's dissertation of Juselius (92), an academic report (93), and later published by Törn and Viitanen (94, 95), which are considered as the main work regarding TGO's first appearance. In these two works, it is possible to find a description of the TGO which summarizes the algorithm in 3 main steps. Step 1 is the distribution of points in a search space, which can be at random or uniformly distributed, provided that the entire space is covered homogeneously. In Step 2, the value of the objective function is calculated for each one of the points of Step 1. The points that have all of its K nearest

neighbors evaluating to higher objective function values are considered topographical minima and, similarly, those that obtain all the neighbors evaluating to lower values are considered as topographical maxima. Finally, in Step 3, a local search method is employed using these topographical optima found in Step 2 as initial solutions.

As far as we know, TGO was first employed in an engineering problem with excellent results in the work of Sacco, Henderson and Rios-Coelho (96), who used it to obtain the optimal design of a nuclear core reactor, showing very competitive results when compared to the literature. Later, Ferreira et al. (97) proposed a constrained iterative version of TGO which was used to optimize eight complex engineering design problems, achieving state of the art results. Jardim et al. (98) performed the first comparison of the influence of initial points generators on the outcome of TGO by employing it in a parameter estimation inverse problem. They showed that, indeed, the initial points generator can influence the final results. But the question about how much the performance can be enhanced with different local search methods when combined with these generators has not been tackled yet.

Therefore, the specific objective of this work and its main contribution is to analyze the configuration of the TGO algorithm that achieves the lowest cost in solving the given inverse heat transfer problem. In this case, the number of function evaluations necessary to reach the Morozov's Discrepancy Principle is the metric used. The methods used in Step 1 are the point generators known as Mersenne Twister (MT) (99) and the Sobol Sequence (SS) (100), being the discrepancy of the generated points the main difference between them. While the distance of MT points have a high discrepancy, SS generates points with a low discrepancy among them, that is, the points tend to be uniformly distributed with the latter. For Step 3, the classical local search methods known as Nelder-Mead (101), a gradient-free method, and the gradient based Levenberg-Marquardt (73, 74) are used. Therefore, in total, four different combinations of TGO are tested and used to solve the three different inverse heat transfer problems.

The first IHTP deals with simultaneous heat transfer by conduction and radiation, the second one deals with heat conduction in a thermally thin plate and the third problem involves internal convection in a flow between parallel plates. For each of these problems, related inverse problems are defined. The first two address the estimation of thermophysical parameters of the medium and material, and the third one consists of estimating the

channel's inlet temperature profile.

This paper does not aim to compare the performance of TGO with other optimization methods, as this has already been extensively discussed in the literature (90, 96). Instead, it focuses on developing several comparisons between different variations made in the initial and final steps of the method. The purpose of these comparisons is to understand the strengths and weaknesses of each version and to identify which one is better suited for a given heat inverse transfer problem. The text is organized as follows: Section 2 introduces the TGO algorithm along with the two point generators and the local search methods, while Sections 3 and 4 present the formulation and solution of the heat transfer direct and inverse problems, respectively. The results obtained are showcased and commented in Section 5, and lastly, final remarks are presented in Section 6.

4.2 The Topographical Global Optimization (TGO)

TGO uses the topographic heuristic in order to select minima from a set of H initial points distributed in the search space. These selected minima are then used as starting points for a local optimization method. The algorithm can be briefly described in three steps (90, 96):

1. Sample the search space with H distributed points in such way that the whole space is evenly covered.
2. Construct the topography by analyzing the objective function value at each one of the H points. When a point has K -neighbors evaluating to higher objective function values, this particular point is considered to be a topographical minimum.
3. All the topographical minima from Step 2 are set as starting points for a local optimization method. The global minimum is the lowest function evaluation from all the local search executions.

The present Section provides further insight on how we implemented each one of the Steps and the combinations used to obtain the performance comparisons. Subsection 4.2.1 presents the two point generators used, subsection 4.2.2 presents the main step of TGO, which selects the topographical optima and, lastly, subsection 4.2.3 summarizes the two local search methods.

4.2.1 Step 1: Search space sampling

The first step of TGO consists of generating H points evenly distributed in the search space in order to sample the objective function. These points can be generated uniformly or at random. As mentioned by the original authors, it is important not to leave areas unexplored when performing the sampling, therefore good point generators are needed (102).

In this work we used the pseudo-random Mersenne Twister (MT) (99) and the quasi-random Sobol Sequence (SS) (100). Despite being deterministic, the points from a pseudo-random generator try to imitate a genuine random sequence. The numbers of a quasi-random generator are organized in order to avoid each other as much as possible, approaching an uniform distribution.

In Figure 24, it is possible to observe two illustrative examples of 400 points generated in a two-dimensional space for the Mersenne Twister (a) and the Sobol Sequence (b). It is clear that the Sobol Sequence tends to generate a more uniform distribution, while the Mersenne Twister has a greater discrepancy. Both SS and MT are used in this work as an option of the built-in "RandomReal" function of the Mathematica system, but their codes are freely available on the websites (103) for MT and (104) for SS.

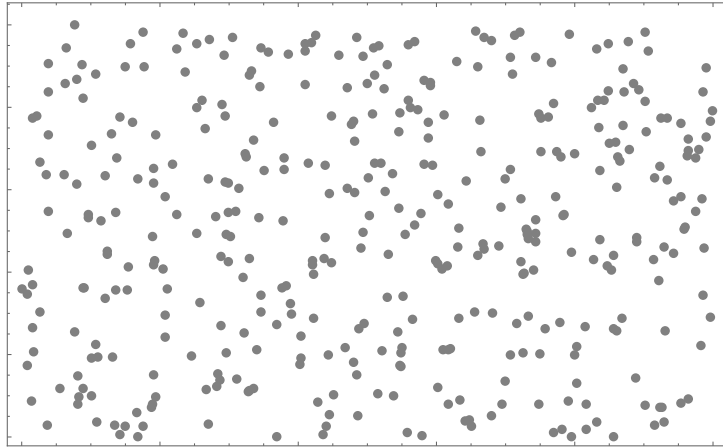
Since SS and MT actually provide a sequence of numbers, each of these numbers can be interpreted as a state of the sequence and, for each new state, a recursive relation is used with previous states, so the sequence must be used in an uninterrupted way (105). It is possible to initialize the sequence starting from any chosen state, as long a seed is provided. In the Wolfram Mathematica system (80), we generated this seed randomly with the "*RandomInteger*" routine for each execution of TGO, which is started independently. These seeds are random integers generated in the range between 1 and 10^6 . The effect of changing seeds on the distribution of points in a two-dimensional space can be observed on the website (106), where a demonstration of different starting point generators implemented in Mathematica can be interactively tested.

4.2.2 Step 2: Construction of the topography

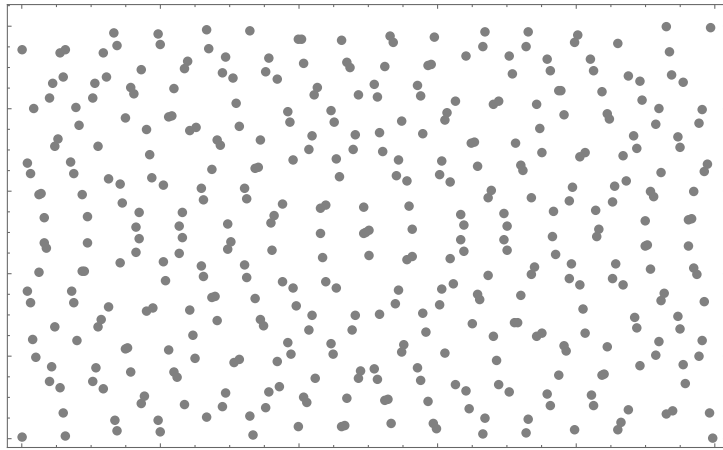
The basic idea of Step 2 is to select points that, by themselves, represent the region of a minimum. This is achieved by the topographical heuristic: the objective function

Figure 24 – Example of 400 points with MT and SS.

(a) Mersenne-Twister



(b) Sobol Sequence



Source: The author, 2023.

is evaluated for each one of the H points from Step 1 and the ones that have all of its K nearest neighbors with higher objective function values are considered topographical minima. One possible implementation of this step is explained as follows.

Consider that the set of points distributed in the search space is denoted by \mathbf{P}_i with $i = 1, 2, \dots, H$, where, for example, \mathbf{P}_1 is the first point given by the random number generator.

To perform the selection of the topographical optima, first a distance matrix, called \mathbf{D} , is constructed with size $H \times H$. In this matrix, each element D_{ij} is the distance between points \mathbf{P}_i and \mathbf{P}_j , with $i, j = 1, 2, \dots, H$.

Now each line of \mathbf{D} must have its elements ranked in ascending order and these rankings are stored in another matrix called \mathbf{R} . Before that, since the distance from a point to itself is zero, the elements of the main diagonal of \mathbf{D} are given a high generic value before the construction of \mathbf{R} , otherwise these elements will always be associated with the first ranking of 1.

In each line of \mathbf{R} , the K -smallest elements have column indices that are the indices of the points closest to the point referring to the index of that line. These K -lower indexes make up the matrix called \mathbf{KNN} , that is, an $H \times K$ matrix that has in its line i the list of indexes of K -nearest points of point \mathbf{P}_i .

Now it is necessary to evaluate the objective function for each one of the H sampled points. These evaluations are stored in a vector called \mathbf{F} that has dimension H . Usually, this is the stage of the method that has the highest computational cost, as it depends on the evaluation of the objective function for each point.

The elements j of a \mathbf{KNN} line i receive a “+” sign if the evaluation of \mathbf{P}_j leads to a higher objective function value than \mathbf{P}_i . Similarly, this element is given a “-” sign when this evaluation is lower.

Points associated with \mathbf{KNN} lines indices that have only positive signs are considered the topographical minima and points that are associated with lines that have only negative signs are considered topographic maxima. A pseudo-code for Step 2 is presented in Algorithm 1.

From this description given about TGO, some comments can be highlighted. The method will always return at least 1 point as the topographic optimum. That is, if the number of nearest neighbors to be analyzed K is small, the tendency is that many points

will be found. If K is large, few points will be found, with the minimum limit being only one point, which in this case is the minimum among all H points. Neither extreme situation is desirable, as finding many points will increase the computational cost of the method by executing many local searches, and finding only few points can be considered as a poor exploration of the search space.

Algorithm 1: TGO algorithm for minimization. See Ref. (2)

choose: number of initial points H and number of closest neighbors K
store in \mathbf{P} : H points distributed in a closed search space
store in \mathbf{F} : the objective function evaluation for each point of \mathbf{P}
assemble the distance matrix \mathbf{D} for the points of \mathbf{P}
rank the elements of each line of \mathbf{D} in ascending order and **store in \mathbf{R}**
for each line $i = 1, \dots, H$ **do**
 for each rank $k = 1, \dots, K$ **do**
 for each element $j = 1, \dots, H$ **do**
 if $\mathbf{R}[i, j] = k$ **then**
 $\text{KNN}[i, j] \leftarrow j$;
 end
 end
 end
end
for each line $i = 1, \dots, H$ of \mathbf{KNN} **do**
 for each element of the line $j = 1, 2, \dots, K$ **do**
 if $F[\text{KNN}[i, j]] < F[i]$ **then**
 $\text{KNN}[i, j] \leftarrow \text{KNN}[i, j] \times (-1)$;
 end
 end
end
for each line $i = 1, \dots, H$ of \mathbf{KNN} **do**
 $j = 1$;
 while $\text{KNN}[i, j] > 0$ **do**
 $j \leftarrow j + 1$;
 end
 if $j = K$ **then**
 append j in **index**
 end
end
end
 $P[\text{index}[i]]$ are the topographical minima, for all elements of **index**

4.2.3 Step 3: Local search

The final step of TGO performs a local search using the points selected in Step 2. Any optimization method with local search properties can be used and this is a positive characteristic of TGO, since the performance of local optimizers can change depending on the objective function. In this work we tested two fundamentally different methods for Step 3: Nelder-Mead and Levenberg-Marquardt algorithms.

4.2.3.1 Nelder-Mead (NM)

NM is a minimization method that does not require the calculation of derivatives of the objective function (107), and is considered a direct search method (108). Some authors have highlighted its efficiency in hybridizations with stochastic methods, such as the Particle Collision Algorithm (109), Differential Evolution (110), and the Ant Colony Algorithm (111, 112), among others. Even to this day, some novel improvements and adaptations of this classical algorithm are still being developed (113, 114) and its fundamental characteristics are the base for improvements of other methods (115).

To illustrate how one can perform the NM search, consider a generic objective function $f(\mathbf{x})$, where \mathbf{x} is a vector of real variables, we define the set of points $\mathbf{x}^* = \{\mathbf{x}_1, \mathbf{x}_2, \dots, \mathbf{x}_n, \mathbf{x}_{n+1}\}$ as initial candidate solutions. In addition, for the implementation of NM, four scalar parameters must be specified. They are the coefficient of reflection (A), expansion (B), contraction (C) and shrinkage (D). To minimize f using NM, the points in \mathbf{x}^* must be ordered so that $f(\mathbf{x}_1) \leq f(\mathbf{x}_2) \leq \dots \leq f(\mathbf{x}_n) \leq f(\mathbf{x}_{n+1})$ and then the centroid \mathbf{x}_0 of all points, except \mathbf{x}_{n+1} , is calculated. After that, several conditional steps are performed until a stopping criterion Δ is reached, as presented in Algorithm 2.

Here an implementation choice must be done. The user can choose these two options:

- **Set each point given by TGO's Step 2 as an NM search by itself.** This can be performed by generating random points inside a relatively small interval around each point returned by Step 2. This option may have an increased computational cost, since more points are generated in order to complete the search. Note that NM needs at least the number of dimensions plus one point to properly execute its algorithm. For example, in a two-dimensional search space, NM needs three points

to execute its routine, if TGO returns four points in Step 2, each one of these points will receive two randomly generated points, giving a total of 12 points, 4 given by TGO and 8 later added.

- **Set all points from Step 2 as a single search for NM.** With this option, the computational cost tends to be smaller, but some problems can be found. If TGO returns less points than the necessary for the NM routine, random points must be generated in the whole search space in order to complete the minimum needed, which can decrease its performance. Another problem is the exploration of the local minima itself, which may be poor since the simplex vertices will converge quickly to the best point from TGO.

In this work, we implemented the first option described: every point from TGO is a search by itself. However, we tested the second option and the results found were better in terms of computational cost. Nevertheless, the routine with the first option is more *aligned* with the classical description of TGO, where every point given in Step 2 represents the neighborhood of an optimum. Moreover, we opted to perform one iteration of the NM algorithm for each TGO point in a sequential way. Therefore, one loop presented in Algorithm 2 is executed for one point of TGO, then the next point is used. This loop is executed in a cycle for every TGO point until stopping criterion is reached.

4.2.3.2 Levenberg-Marquardt (LM)

The Levenberg-Marquardt (LM) method is a deterministic optimization technique that aims to minimize the least squares functional. It was originally introduced by Levenberg (73) in 1944, but it was Marquardt (74) who rediscovered it in 1963 and made a crucial contribution to increase the chances of convergence of the algorithm. As a result, the method became widely known as the Levenberg-Marquardt algorithm.

LM applications and its variations to solve inverse problems in science and engineering are still relevant today due to the robust convergence characteristics of the method (116, 117). In addition, since its purpose is to minimize least squares objective functions, LM has recently found great usefulness in Artificial Neural Networks training (118, 119, 120, 121, 122), which is a fitting problem.

To illustrate the algorithm, consider a generic least-squares objective function $F(\mathbf{x})$

Algorithm 2: Nelder-Mead Simplex Algorithm for minimization

choose: A, B, C, D and Δ

sort the points of \mathbf{x}^* so that $f(\mathbf{x}_1) \leq f(\mathbf{x}_2) \leq \dots \leq f(\mathbf{x}_{n+1})$

while $f(\mathbf{x}_1) > \Delta$ **do**

1. **centroid:** compute the centroid \mathbf{x}_0 from all points except \mathbf{x}_{n+1}

2. **reflection:** compute the reflected point \mathbf{x}_r

$\mathbf{x}_r = \mathbf{x}_0 + A(\mathbf{x}_0 - \mathbf{x}_{n+1});$

if $f(\mathbf{x}_1) \leq f(\mathbf{x}_r) \leq f(\mathbf{x}_{n+1})$ **then**

$\mathbf{x}_{n+1} \leftarrow \mathbf{x}_r;$

go to step 6;

else

3. **expansion:**

if $f(\mathbf{x}_r) < f(\mathbf{x}_1)$ **then**

 Compute the expanded point \mathbf{x}_e

$\mathbf{x}_e = \mathbf{x}_0 + B(\mathbf{x}_r - \mathbf{x}_0);$

if $f(\mathbf{x}_e) < f(\mathbf{x}_r)$ **then**

$\mathbf{x}_{n+1} \leftarrow \mathbf{x}_e;$

go to step 6

else

$\mathbf{x}_{n+1} \leftarrow \mathbf{x}_r$

go to step 6

end

end

4. **contraction:** Compute the contracted point \mathbf{x}_c

$\mathbf{x}_c = \mathbf{x}_0 + C(\mathbf{x}_{n+1} - \mathbf{x}_0);$

if $f(\mathbf{x}_c) < f(\mathbf{x}_{n+1})$ **then**

$\mathbf{x}_{n+1} \leftarrow \mathbf{x}_c$

end

5. **shrinkage:**

for each point $i = 2, 3, \dots, n, n + 1$ **do**

$\mathbf{x}_i \leftarrow \mathbf{x}_1 + D(\mathbf{x}_i - \mathbf{x}_1)$

end

end

6. **sort** the points of \mathbf{x}^* so that $f(\mathbf{x}_1) \leq f(\mathbf{x}_2) \leq \dots \leq f(\mathbf{x}_{n+1})$

end

\mathbf{P}_1 is the solution

written as

$$F(\mathbf{x}) = \sum_{i=1}^{N_{\text{EXP}}} (Y_i - \phi(x_i))^2 = (\mathbf{Y} - \phi(\mathbf{x}))^T \cdot (\mathbf{Y} - \phi(\mathbf{x})) = \mathbf{r}(\mathbf{x})^T \cdot \mathbf{r}(\mathbf{x}) \quad (4.1)$$

where \mathbf{x} is the vector of real unknowns variables, \mathbf{Y} is the vector containing the experimental data, ϕ is the solution of the physical model related to \mathbf{Y} , $\mathbf{r}(\mathbf{x})$ is the residual vector containing the difference between the experimental data and the physical model at \mathbf{x} and N_{EXP} is the total number of experimental data.

Starting from an iteration k , the procedure is built to obtain new estimates $k + 1$ using $\mathbf{x}^{k+1} = \mathbf{x}^k + \Delta\mathbf{x}^k$ where $\Delta\mathbf{x}^k$ is defined as

$$\Delta\mathbf{x}^k = - \left[(\mathbf{J}^k)^T \mathbf{J}^k + \lambda^k \mathbf{I} \right]^{-1} (\mathbf{J}^k)^T \mathbf{r}^k \quad (4.2)$$

where \mathbf{I} is the identity matrix with dimension of the number of variables, λ the damping factor and \mathbf{J} is the Jacobian matrix of the physical quantities with respect to the unknown parameters, i.e.

$$J_{ij} = \frac{\partial \phi_i}{\partial x_j}, \quad i = 1, 2, \dots, N_{\text{EXP}}, \quad b = 1, 2, \dots, N_{\text{un}} \quad (4.3)$$

where N_{un} is the number of unknowns.

Concerning the implementation of LM with the points selected by TGO, the approach chosen is to advance one iteration k for each point from TGO's Step 2. That is, each TGO point takes a step with Eq. 4.2 in a sequential way. This approach may result in an increased computational cost, but it also enhances the likelihood of overcoming local minima.

Algorithm 3 presents the pseudo-code for the LM using a set of starting points given by $\mathbf{x}^* = \{\mathbf{x}_1, \mathbf{x}_2, \dots, \mathbf{x}_n\}$, where n represents the number of points selected in the second step of TGO. In this implementation it is also necessary to define the vector of objective function evaluations $\mathbf{F} = \{F(\mathbf{x}_1), F(\mathbf{x}_2), \dots, F(\mathbf{x}_n)\}$, where F represents the generic least squares calculation, as described by Eq. 4.1.

Algorithm 3: Levenberg-Marquardt Algorithm for minimization

choose: λ and assemble $\boldsymbol{\lambda} = \{\lambda, \lambda, \dots, \lambda\}$ with the same dimension as \mathbf{F}

choose: Δ as stopping criterion

define: $\mathbf{F}_{\text{old}} \sim \{\infty, \infty, \dots, \infty\}$ with the same dimension as \mathbf{F}

for each external iteration $k = 1, 2, \dots, \text{MaxIter}$ **do**

for each point $i = 1, 2, \dots, n$ **do**

evaluate the residue vector $\mathbf{r}(\mathbf{x}^* [i])$

$F [i] \leftarrow \mathbf{r}(\mathbf{x}^* [i])^T \cdot \mathbf{r}(\mathbf{x}^* [i])$

if $F [i] < \Delta$ **then**

 | **break**

end

if $F [i] < F_{\text{old}} [i]$ **then**

 | $\boldsymbol{\lambda} [i] \leftarrow \boldsymbol{\lambda} [i] / 10$

else

 | $\boldsymbol{\lambda} [i] \leftarrow \boldsymbol{\lambda} [i] \times 10$

end

evaluate the step $\Delta \mathbf{x}$ with Eq. 4.2 for point $\mathbf{x}^* [i]$

$\mathbf{x}^* [i] \leftarrow \mathbf{x}^* [i] + \Delta \mathbf{x}$

end

end

Find: the smallest value of \mathbf{F} and store its index as min

$\mathbf{x}^* [min]$ is the solution

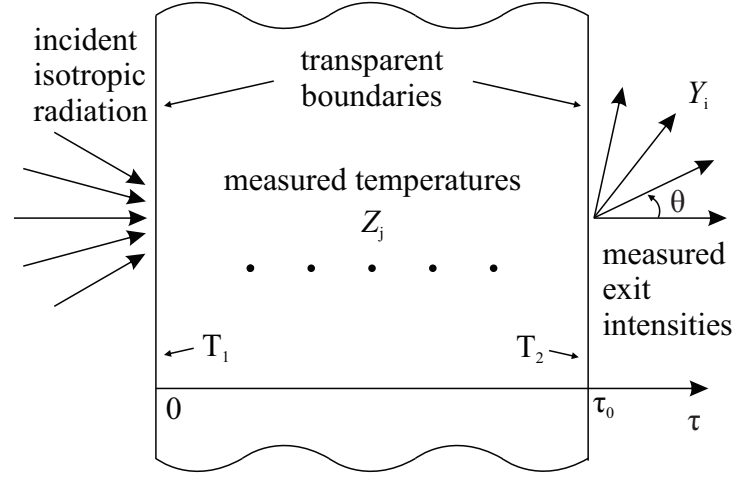
4.3 Formulation and solution of the Heat Transfer Problems

4.3.1 Direct Problem 1 (DP-1): Heat transfer by simultaneous conduction and radiation in a semi-transparent medium

Consider a steady-state one-dimensional medium that is subjected to heat transfer by both conduction and radiation. Consider also that this medium absorbs, emits and scatters isotropically the radiation. The spatial coordinate and the optical thickness are represented respectively by $\tau = \int_0^x \beta dx$ and $\tau_0 = \int_0^L \beta dx$, where β is the extinction coefficient, and L is the physical length of the medium, which has transparent boundaries and incident radiation in $\tau = 0$, as shown in Figure 25. The temperatures at the boundaries $\tau = 0$ and $\tau = \tau_0$ are kept constant as T_1 and T_2 , respectively, also shown in Figure 25.

The mathematical formulation for the combined conduction-radiation heat transfer problem with the temperature in its dimensionless form, $\Theta(\tau)$, is given by the Poisson Equation (77)

Figure 25 – Schematic representation of the medium subjected to the coupled conduction-radiation heat transfer phenomena (2, 3).



Source: Adapted from Silva Neto and Ozisik, 1993 (3).

$$\frac{d^2\Theta}{d\tau^2} - \frac{(1-\omega)}{N} [\Theta^4 - G^*(\tau)] = 0, \text{ in } 0 < \tau < \tau_0 \quad (4.4a)$$

$$\Theta = \Theta_1 \text{ at } \tau = 0 \quad (4.4b)$$

$$\Theta = \Theta_2 \text{ at } \tau = \tau_0 \quad (4.4c)$$

where ω is the single scattering albedo, and the dimensionless variables are defined as

$$G^*(\tau) = \frac{1}{2} \int_{-1}^1 I(\tau, \mu) d\mu \quad (4.5a)$$

$$N = \frac{k\beta}{4\psi^2\bar{\sigma}T_1^3} \quad (4.5b)$$

$$\Theta(\tau) = \frac{T(\tau)}{T_1} \quad (4.5c)$$

where G^* is the dimensionless incident radiation, N the conduction-radiation parameter, k is the thermal conductivity, ψ is the refraction index and $\bar{\sigma}$ is the Stefan-Boltzmann constant. The dimensionless radiation intensity, $I(\tau, \mu)$, is determined by the solution of the radiative transfer problem (77)

$$\mu \frac{\partial I(\tau, \mu)}{\partial \tau} + I(\tau, \mu) = R(\Theta) + \frac{\omega}{2} \int_{-1}^1 I(\tau, \mu') d\mu' \text{ in } 0 < \tau < \tau_0, -1 \leq \mu \leq 1 \quad (4.6a)$$

$$I(0, \mu) = 1 \text{ with } \mu > 0 \quad (4.6b)$$

$$I(\tau_0, -\mu) = 0 \text{ with } \mu > 0 \quad (4.6c)$$

where μ is the cosine of θ - angle between the radiation beam and the positive τ axis (also known as polar angle). Another dimensionless quantity is $R(\Theta)$, which is defined as

$$R(\Theta) = (1 - \omega)\Theta^4(\tau) \quad (4.7)$$

The simultaneous conduction and radiation heat transfer direct problem - from now on called DP-1 - is described by Eqs. 4.4 and 5.8. Its solution is obtained using Chandrasekhar's discrete ordinates method where the angular domain is discretized and the integrals replaced by Gauss-Legendre quadratures.

The built-in routine "NDSolve" of the Wolfram Mathematica 11.0 software (80) is then used to solve the differential equation of coupled equations generated by the the polar angle discretization - see Eq. 5.8a and Eq. 4.4a. This routine is performed under automatic absolute and relative error control. The problem given by Eq. 4.4a is also solved with "NDSolve" routine, but for the sake of stability, a pseudo-transient regime is necessary to increase the solution's stability.

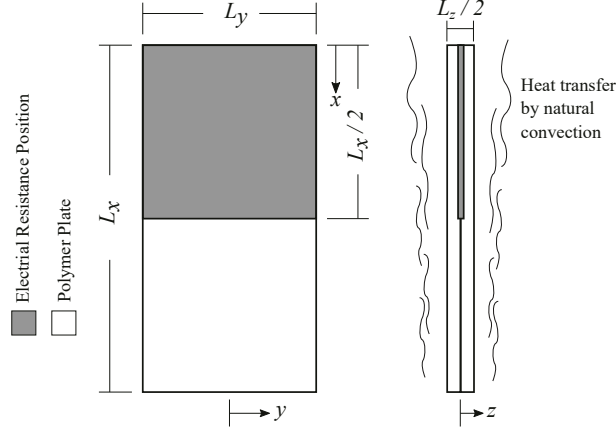
This solution method was used by Knupp et al. (81), but here a heat conduction problem is present and coupled with the radiation problem. The conduction problem uses information of the radiation intensity through the term G^* and the radiation problem requires information of the temperature in the dimensionless quantity R . Algorithmically, the iterative process is constructed by giving an initial solution to the radiation intensity so the quantity G^* can be calculated. Following that it is possible to obtain obtain the temperature profile and calculate R . That ends the iteration because this R generates a new radiation intensity profile and the process restarts. This method is considered converged when the maximum absolute error between two radiation intensity profiles in consecutive iterations is below some pre-defined tolerance.

4.3.2 Direct Problem 2 (DP-2): Heat conduction in a thermally thin plate

Consider a system composed by two polymer plates with dimensions $L_x \times L_y \times L_z$ each. There is a thin heater between those two plates, positioned as illustrated in Figure 26. Furthermore, the external surfaces of both plates exchange heat with the external

environment via natural convection.

Figure 26 – Schematic representation of the system plate-resistance-plate. (4)



Source: The author, 2023.

We assume that there is no heat gradient along the y direction and that all thermal and physical properties are constant. The lumped analysis technique can be employed to model this system, thereby reducing its dependence on spatial dimensions to just one, the x direction. Such technique uses the hypothesis that the average temperature inside the plate, along the z axis, is very close to the temperature at both $z = 0$ and $z = L_z$, i.e., the temperature variation along z is so small when compared to the variation in x , that its effect can be neglected (4). The heat diffusion equation with the mathematical manipulation of the lumped parameters technique is written as

$$k \frac{\partial^2 T(x, t)}{\partial x^2} - \frac{h_{\text{eff}}(x)[T(x, t) - T_{\infty}]}{L_z} + \frac{q_h''(x)}{L_z} = \rho c_p \frac{\partial T(x, t)}{\partial t} \quad (4.8a)$$

$$k \left. \frac{\partial T(x, t)}{\partial x} \right|_{x=0} = 0 \quad (4.8b)$$

$$k \left. \frac{\partial T(x, t)}{\partial x} \right|_{x=L_x} = 0 \quad (4.8c)$$

$$T(x, 0) = T_{\infty} \quad (4.8d)$$

where $T(x, t)$ is the average temperature along the z direction, T_{∞} is the ambient temperature, which is considered constant during the experiment, $h_{\text{eff}}(x)$ is the heat transfer coefficient at $z = L_z$, which is a combination of heat transfer by natural convection and

linear radiation, $q_h''(x)$ is the heat flux into the plate at $z = 0$ due to the electrical heater, ρ and c_p are, respectively, the specific mass and the specific heat of the plate, and k its thermal conductivity. Note that with this formulation the temperature profile has only one spatial coordinate dependence.

The problem described by Eq. 4.8 is numerically solved using a Finite Difference formulation. With an implicit formulation, this approach yields a system of linear equations, which is solved using the built-in routine "LinearSolve" of the Wolfram Mathematica 11.0 (80) software. The result obtained, when all the variables, parameters and conditions are known, is the temperature $T(x, t)$ as an interpolated function of space and time.

4.3.3 Direct Problem 3 (DP-3): Heat transfer in a thermally developing fluid flow inside parallel plates

DP-3 consists of determining the steady state temperature field of a hydrodynamically developed and thermally developing fluid flow inside two parallel plates channel subjected to a constant heat flux q'' (123, 124), as presented schematically in Figure 35. Neglecting viscous dissipation, free convection, and the axial conduction effects, the mathematical formulation that describes the temperature field $T(x, y)$ can be written as (125)

$$k \frac{\partial^2 T(x, y)}{\partial y^2} = u(y) \rho c_p \frac{\partial T(x, y)}{\partial x}, \text{ in } 0 < x < b \text{ and } 0 < y < h \quad (4.9a)$$

$$k \left. \frac{\partial T(x, t)}{\partial y} \right|_{y=h} = q'', \text{ with } 0 < x < b \quad (4.9b)$$

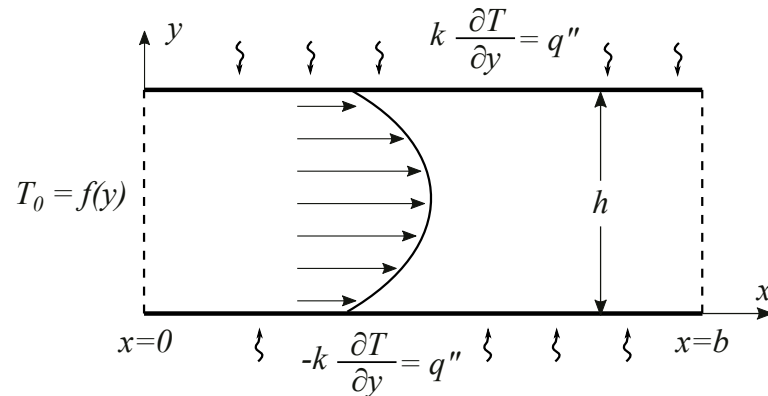
$$-k \left. \frac{\partial T(x, t)}{\partial y} \right|_{y=0} = q'', \text{ with } 0 < x < b \quad (4.9c)$$

$$T(0, y) = f(y), \text{ in } 0 \leq y \leq b \quad (4.9d)$$

$$u(y) = 6u_m \frac{y}{h} \left(1 - \frac{y}{h} \right) \quad (4.9e)$$

where the thermophysical parameters k , ρ and c_p are: the thermal conductivity, specific mass and specific heat, respectively. The term u_m is the average velocity of the fluid flow

Figure 27 – Schematic representation of the parallel plates system showing the height dependence of the fluid velocity with the transversal coordinate.



Source: Adapted from Bokar and Ozisik, 1995 (125).

in the channel, calculated from the parabolic profile for the velocity field $u(y)$.

To solve the problem described by Eq. 4.9, the built-in routine “NDSolve” of the Mathematica system is used again. Here the chosen approach is to use the Finite Elements Method and, to do so, the mesh generated to discretize the domain is rectangular and all the elements have the same dimensions, i.e., the mesh is uniform. In this approach, the velocity field $u(y)$ and the inlet temperature $f(y)$ are implemented as continuous functions, so the discretization to solve the differential equation numerically is performed automatically by the “NDSolve” routine (80).

4.4 Inverse Problems Formulation

The inverse problems proposed in this work are formulated using the maximum likelihood approach, which yields a least-squares objective function to be minimized. This function is given by the sum of squared residuals between the experimental data and the corresponding quantity calculated by the direct model. The first two inverse problems deal with the estimation of thermophysical parameters, and the third one with the estimation of the inlet temperature profile. These formulations are further explained on subsections 4.4.1 to 4.4.3.

4.4.1 Inverse Problem 1 (IP-1):

Consider that the thermal conductivity k , the single scattering albedo ω and the optical thickness τ_0 are unknowns in DP-1, leading to the following vector of unknowns:

$$\mathbf{u}_1 = \{N, \omega, \tau_0\}^T \quad (4.10)$$

where the thermal conductivity k is included in the formulation of the conduction-radiation dimensionless parameter N . See Eq. 4.5b.

Experimental data are necessary to obtain the estimates of \mathbf{u}_1 . In this work these data are simulated using the solution of the DP-1 itself. This solution yields two physical quantities, the radiation intensity I and the dimensionless temperature Θ , and, in order to generate the simulated experimental data, random noise drawn from a normal distribution is added, as follows

$$Y_i = I(\tau_0, \mu_i, \mathbf{u}_1^{\text{exact}}) + e, \quad e \sim N(0, \sigma_1^2), \quad i = 1, 2, \dots, D_1^{\text{Rad}} \quad (4.11a)$$

$$Z_j = \Theta(\tau_j, \mathbf{u}_1^{\text{exact}}) + r, \quad r \sim N(0, \sigma_1^2), \quad j = 1, 2, \dots, D_1^{\text{Temp}} \quad (4.11b)$$

where D_1^{Rad} and D_1^{Temp} are the total number of radiation intensity and temperature experimental data, respectively. The reader can notice that the variance has the same value for the radiation intensity and for the temperature. This choice was based on the fact that both quantities are dimensionless, and their magnitude lies within the same range. Another important thing to keep in mind is the fact that the radiation intensity is acquired on the exit boundary $\tau = \tau_0$, which is physically reasonable due to the nature of the problem - see Figure 25.

The following objective function is then obtained, and should be minimized (3):

$$S_1(\mathbf{u}_1) = \sum_{i=1}^{D_1^{\text{Rad}}} [Y_i - I(\tau_0, \mu_i, \mathbf{u}_1)]^2 + \sum_{j=1}^{D_1^{\text{Temp}}} [Z_j - \Theta(\tau_j, \mathbf{u}_1)]^2 \quad (4.12)$$

4.4.2 Inverse Problem 2 (IP-2):

Consider that the unknown parameters are thermal conductivity k and the specific heat c_p , thus forming the vector of unknowns \mathbf{u}_2 , which is written as

$$\mathbf{u}_2 = \{k, c_p\}^T \quad (4.13)$$

In this problem, the experimental temperature data are also simulated, but as they can be obtained spatially for different time periods, the indices j and i are used to represent such variables dependence, respectively. Then it is possible to write the set of experimental temperature data \mathbf{W} as

$$W_{i,j} = T(x_j, t_i, \mathbf{u}_2^{\text{exact}}) + p, \quad p \sim N(0, \sigma_2^2), \quad i = 1, 2, \dots, D_2^t, \quad j = 1, 2, \dots, D_2^x \quad (4.14)$$

The term D_2^t represents the number of time instants for which all the D_2^x temperature data were obtained. In other words, there is a total number of $D_2 = D_2^t \times D_2^x$ experimental data for this problem.

The IP-2 solution, can be obtained with the minimization of the following objective function:

$$S_2(\mathbf{u}_2) = \sum_{i=1}^{D_2^t} \sum_{j=1}^{D_2^x} [W_{i,j} - T(x_j, t_i, \mathbf{u}_2)]^2 \quad (4.15)$$

4.4.3 Inverse Problem 3 (IP-3):

The third inverse problem aims at estimating the inlet temperature profile $f(y)$ given that temperature measurements are available at some discrete positions along the channel. In this case, the vector of unknowns contains temperature values representing discrete points of $f(y)$

$$\mathbf{u}_3 = \{T_1, T_2, \dots, T_n\}^T, \quad T_1 = f(y_1), T_2 = f(y_2), \dots, T_n = f(y_n) \quad (4.16)$$

where n is the total number of points used in the discretization. The experimental measurements are simulated with

$$Q_i = T(x^{\text{exp}}, y_i, f^*) + v, \quad v \sim N(0, \sigma_3^2), \quad i = 1, 2, \dots, D_3 \quad (4.17)$$

where D_3 is the total number of experimental data, f^* is the exact inlet temperature profile. Then, the objective function to be minimized is formulated as

$$S_3(\mathbf{u}_3) = \sum_{i=1}^{D_3} [Q_i - T(x^{\text{exp}}, y_i, \mathbf{u}_3)]^2 \quad (4.18)$$

4.5 Results and discussion

The results are presented in three main parts: in Section 4.5.1 the direct problem solutions and the simulated experimental data are presented. In section 4.5.2 we present the results using TGO with different combinations of methods in order to compare the efficiency yielded by each one. Finally, in section 4.5.3 a statistical test is performed to show which approach led to better results.

4.5.1 Direct problems solutions and experimental data

4.5.1.1 Direct Problem 1: Solution and experimental data

Some authors have already shown that there is a difficulty in estimating the conduction-radiation parameter N when it has small values, that is, $N < 0.05$ due to the lack of sensitivity (3, 126). In order to obtain a feasible result of the optimization method with a reasonable computational cost, the exact value chosen for parameter N in this work is precisely $N_{\text{exact}} = 0.05$. In addition, the single-scattering albedo and the optical thickness exact values are $\omega_{\text{exact}} = 0.3$ and $\tau_{0\text{exact}} = 1.0$, respectively.

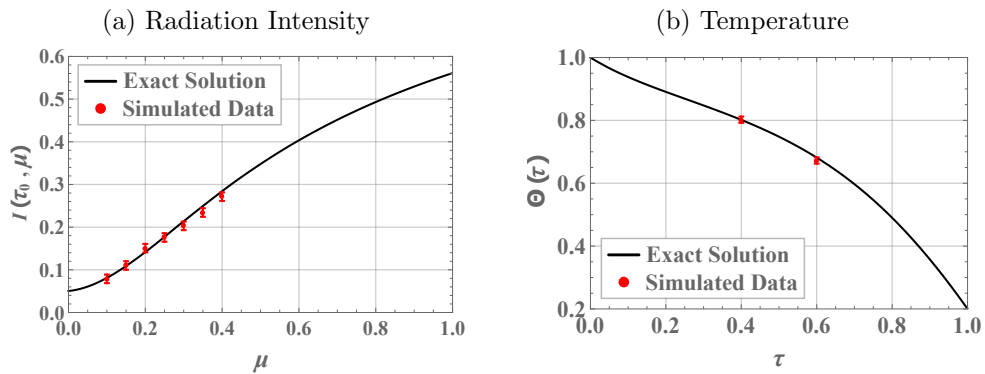
As previously mentioned, the radiation intensity experimental data are all obtained at the exit boundary, i.e., $\tau = \tau_0$. But the polar angles chosen to read these radiations must be more carefully determined. According to the sensitivity analysis performed in Ref. (2), the best angular range to position the sensors would be within the cosine range of $0 < \mu < 0.4$. Thus, we selected seven radiation intensity acquisition sensors positioned at polar angles cosines of $\mu = \{0.10; 0.15, 0.20; 0.25; 0.30; 0.35; 0.40\}$. For the temperature readings, the choice is to use two sensors located at $\tau = \{0.4 \tau_0, 0.6 \tau_0\}$. The experimental data is simulated using a noise level of $\sigma_1 = 0.01$ in Eq. 4.11, which leads to a maximum

Table 14 – Exact values of the parameters for DP-1 and IP-1.

Parameter	Value	Dim.	Description
N	0.05	-	Conduction-radiation parameter
ω	0.30	-	Single-scattering albedo
τ_0	1.00	-	Optical thickness
Θ_1	1.00	-	Temperature boundary condition
Θ_2	0.20	-	Temperature boundary condition
D_1^{Rad}	7	-	Number of radiation experimental data
D_1^{Temp}	2	-	Number of temperature experimental data
σ_1	0.01	-	Std. dev. of the experimental data error

Source: The author, 2023.

Figure 28 – Exact solution and experimental data for DP-1, obtained with $N = 0.05$, $\omega = 0.3$, $\tau_0 = 1.0$ and $\sigma_1 = 0.01$.



Source: The author, 2023.

percentage error of 6.5% for the radiation intensity and 1.3% for the temperature for this particular set of data. All these and other parameters used in the simulations are summarized in Table 25. The calculated values for radiation intensity and dimensionless temperature obtained with these parameter values are displayed in Figure 28, where the continuous line is the exact solution, and the points are the experimental data generated with Eq. 4.11.

4.5.1.2 Direct Problem 2: Solution and experimental data

The plates used in this problem have dimensions $L_x = 0.08$ m, $L_y = 0.04$ m and $L_z = 0.0016$ m, as displayed in Table 15. The spatial discretization of the x coordinate was performed with 21 uniformly distributed points, which yielded a discrete interval of

Table 15 – Exact values of the parameters of DP-2 and IP-2.

Parameter	Value	Dim.	Description
k	0.22	[W/m.K]	Thermal conductivity
c_p	1680	[J/kg.K]	Specific heat
ρ	1060	[kg/m ³]	Specific mass
L_x	0.0800	[m]	Plate dimension
L_y	0.0400	[m]	Plate dimension
L_z	0.0016	[m]	Plate dimension
T_∞	24.0	[°C]	Ambient temperature
D_2^t	3	-	Number of time instants
D_2^x	201	-	Number temperature data in x
σ_2	0.50	[°C]	Std. dev. of experimental data error

Source: The author, 2023.

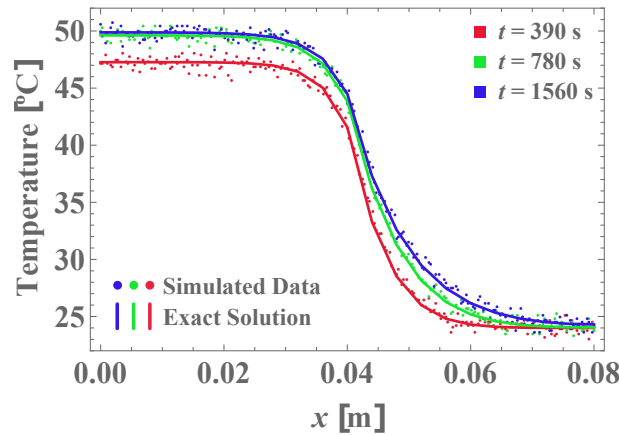
0.004 m. The transient march was defined with a step in time of 5 s.

The material chosen for the plates is the Nylon_{6,12}: it has thermal conductivity $k = 0.22$ W/m.K, specific heat $c_p = 1680$ J/kg.K, and specific mass $\rho = 1060$ kg/m³ (127). Therefore, $\mathbf{u}_2^{\text{exact}} = \{0.220, 1680\}^T$ is the vector of exact values which generates the experimental data.

According to empirical correlations for natural convection and linearized radiation, the coefficient of heat transfer by convection h_{eff} has a magnitude of 17 W/m²K for the heated portion and 4 W/m²K for the non-heated portion of the plate (54). The generated heat due to the thin electrical resistance - which acts only on the top half of the plate - can be calculated via Joule's law of heating leading to a magnitude of $q_h'' = 440.0$ W/m²K. The whole experiment is carried out with a constant ambient temperature $T_\infty = 24^\circ\text{C}$.

The experimental data are acquired in three instants of time: $t = 390$ s, $t = 780$ s and $t = 1560$ s. In addition, for each of these time instants, 201 temperature data will also be acquired along the x direction, resulting in $D_2 = 603$ experimental data in total. These are temperatures readings supposedly acquired on the exposed face of the plate at different time points, such as those obtained via infrared thermography presented in Ref. (4). Figure 29 shows the simulated experimental data for the three time levels along with the exact solution. The discrepancy between the points is due to the addition of random noise, which is calculated using $\sigma_2 = 0.5$ °C in Eq. 4.14.

Figure 29 – Exact solution and experimental data for the temperature in DP-2, obtained with $k = 0.22$ W/mK, $c_p = 1680$ J/kgK and $\sigma_2 = 0.5$ °C.



Source: The author, 2023.

Table 16 – Exact values of the parameters of DP-3 and IP-3.

Parameter	Value	Dimension	Observation
k	0.0265	[W/m.K]	Thermal conductivity
c_p	1007.0	[J/kgK]	Specific heat
ρ	1.1614	[kg/m ³]	Specific mass
h	0.128	[m]	Spacing between plates
b	0.635	[m]	Plate length
u_m	0.025	[m/s]	Fluid velocity
q''	500	[W/m ²]	Heat flux at the plates
D_3	20	-	Number of experimental data
σ_3	0.50	[°C]	Std. dev. of experimental data error

Source: The author, 2023.

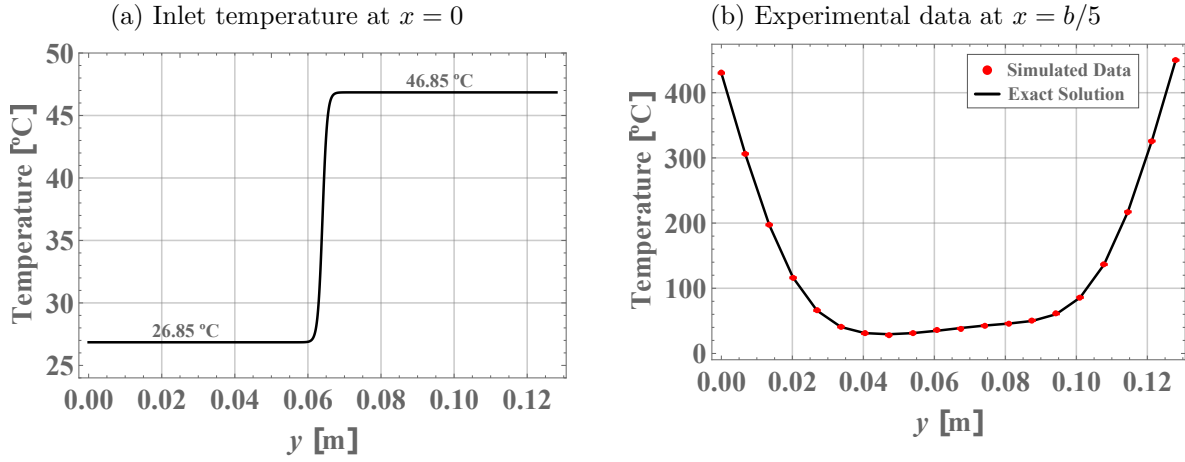
4.5.1.3 Direct Problem 3: Solution and experimental data

To obtain the experimental data from DP-3, the fluid considered is air, and its conditions are the same ones found in Ref. (128), which are presented in ???. The experimental data is acquired with readings evenly distributed on the y direction with incremental spacing of $\Delta y = h/19$ at the horizontal position of $x = b/5$. This acquisition of temperature can be achieved in real experiments by the use of infrared thermography.

As mentioned in subsection 4.3.3, the fluid domain is discretized with a uniform rectangular mesh in order to obtain the solution with FEM. The mesh has a total of 4470 rectangular elements (30 vertically and 149 horizontally).

Figure 30 presents the (a) inlet temperature profile $f(y)$ and (b) the experimental data with the exact solution of the problem. The inlet temperature profile is a step

Figure 30 – Exact solution and experimental data for the temperature in DP-3, obtained with the inlet temperature profile (a) and $\sigma_3 = 0.5$ °C.



Source: The author, 2023.

function, which can represent a stratified flow. The reader can notice that, as expected, the temperature readings are greater when taken closer to the walls due to the presence of the heat flux q'' .

4.5.2 Computational Experiments

Stopping Criterion. To compare the the various TGO combinations performance, we chosen to count the number of objective function evaluations (NFE) necessary to reach the Morozov’s Discrepancy Principle (87). To use this principle as stopping criterion, a tolerance Δ must be defined. This tolerance is calculated for each inverse problem as follows:

$$\Delta_{IP-1} = D_1^{\text{Rad}} \sigma_1^2 + D_1^{\text{Temp}} \sigma_1^2 = 9.0 \times 10^{-4} \quad (4.19a)$$

$$\Delta_{IP-2} = D_2 \sigma_2^2 = 150.75 \text{ [}^\circ\text{C]}^2 \quad (4.19b)$$

$$\Delta_{IP-3} = D_3 \sigma_3^2 = 5.0 \text{ [}^\circ\text{C]}^2 \quad (4.19c)$$

where σ_1^2 , σ_2^2 , σ_3^2 are the variance of the experimental data errors, as already defined in Section 4.4, and D_1 , D_2 and D_3 are the total number of experimental data for each inverse problem. Then, the local search methods in Step 3 are interrupted when the objective function is less or equal than these calculated tolerances. With this approach, it is expected

that the obtained solution will be reasonably stable, meaning that the curve fitting will fall within the experimental error (6).

Search Intervals. The search intervals are shown in Table 17, where \mathbf{u}_{\min} represents the lower limits and \mathbf{u}_{\max} the upper limits for each particular unknown. These intervals define the enclosed space in which the TGO has its points generated. The local search methods also have limitations when they reach these boundaries. If any points of the NM search surpasses one of these boundaries, the simplex from this point is removed completely from the search. The approach with the LM is similar, when any step from LM leads to a point outside the search limit, this particular point is then removed entirely from subsequent searches. This is a reasonable expectation since the LM algorithm demonstrates exceptional convergence characteristics when provided with a good initial estimate. Therefore, even if one of the points provided by Step 2 of TGO exceeds the search limit and is excluded, the LM algorithm will still be able to explore other topographical minima and continue the search. In Table 17, also, the exact values for the unknowns are displayed, with exception of IP-3, whose exact solution is shown in Figure 30a.

Nelder-Mead Configuration. To perform the NM search, each point from TGO Step 2 is a single search by itself, therefore one point must be added to the TGO point for every search dimension. This is achieved by generating random points drawn from a normal distribution centered at the given TGO point, and with standard deviation of 1% of the total search space length in that particular dimension. These points are generated the “RandomReal” Mathematica routine. The parameters for NM are the ones considered standard in the literature: $a = 1.0$, $b = 2.0$, $c = -0.5$ and $d = 0.5$. See Algorithm 2.

Levenberg-Marquardt Configuration. To perform the LM search, it is necessary to choose the damping factor λ : if its value is relatively high, the search tends to be more refined, with smaller steps, which is acceptable when the initial position is a poor initial estimate, but if its value tends to zero, the search will favor convergence - ideal for better initial points - the choice of this parameter directly affects the computational cost of the method. In this work the damping factor is zero for all the inverse problems described, IP-1, IP-2 and IP-3, that is, $\lambda_{\text{IP-1}} = \lambda_{\text{IP-2}} = \lambda_{\text{IP-3}} = 0$. This is a strong choice because when there is no damping factor, the points selected by TGO are trusted to be good initial estimates of the solution.

Table 17 – Search intervals and exact values for IP-1, IP-2 and IP-3

Problem	Parameter	\mathbf{u}_{\min}	$\mathbf{u}_{\text{exact}}$	\mathbf{u}_{\max}
IP-1	N	0.005	0.05	0.5
	ω	0.00	0.3	1.0
	τ_0	0.25	1.0	2.0
IP-2	k [W/m.K]	0.10	0.22	10.0
	c_p [J/kgK]	1000 J/kg.K	1680	5000
IP-3	T_n [°C]	-73.15	See Figure 30a	326.85

Source: The author, 2023.

4.5.2.1 Results for IP-1

Table 18 displays the average NFE required to meet the stopping criterion, based on 10 independent TGO executions - every execution uses a new set of initial points for TGO in Step 1, which is completely determined by the random points generator. In such Table, the terms H and K are the number of initial points and the number of nearest neighbors analyzed, respectively. NNN represents the average number of nearest neighbors found by TGO Step 2. This number indicates how many topographical minima were found by the algorithm.

Among the 16 configurations displayed in Table 18, the SS-LM combination accounted for 10 of the lowest NFE's obtained. The reader may notice that NM presents worse results compared to the LM algorithm for every scenario. This is due to the nature of the search, in NM, extra points are added to each one of the points from TGO's Step 2, which considerably increases the computational cost. In contrast, in LM, in addition to the fact that the gradient search is considerably faster, no extra points are added to the original set of points.

It is also possible to observe that the performance of LM improves considerably when NNN decreases. This is expected, but not always desired. Indeed, with higher values of K , less selected points for initializing the local search method there are, thus leading to less computational cost, however decreasing the number of selected points in Step 2 can be considered a sub-utilization of the TGO algorithm - if the local search algorithm is lost, it will not have other points available to perform the search.

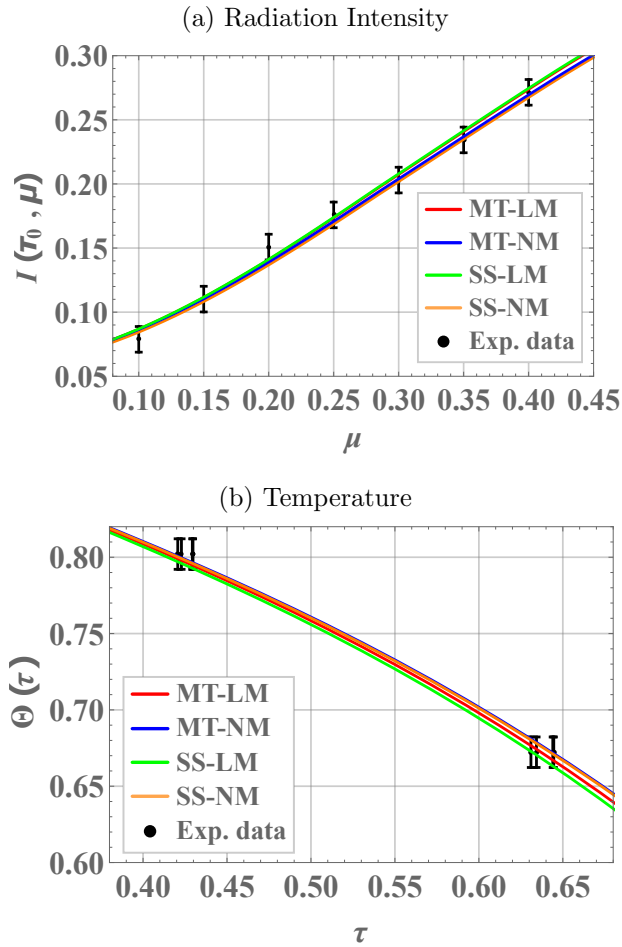
In Figure 31, the obtained temperature and radiation intensity profiles are displayed with the simulated experimental data. In such figure, the error bars correspond to plus

Table 18 – Average results for 10 independent executions of IP-1 with comparisons of Sobol Sequence (SS), Mersenne Twister (MT), Levenberg-Marquardt (LM) and Nelder-Mead (NM).

H	K	SS-LM		SS-NM		MT-LM		MT-NM	
		NNN	NFE	NNN	NFE	NNN	NFE	NNN	NFE
100	10	7.6	167.5	7.7	315.4	8.1	165.4	7.5	189.2
	15	4.3	140.2	4.4	211.2	4.4	140.9	4.3	150.6
160	10	12.8	261.1	12.3	367.4	12.1	244.3	12.8	380.9
	15	6.3	215.6	6.2	250.2	7.9	228.6	6.7	319.2
200	20	6.2	250.7	5.7	298.5	6.2	246.5	6.1	291.4
	25	3.5	233.9	3.8	250.9	4.3	233.9	4.4	280.1
320	25	7.1	376.3	5.8	383.7	7.8	372.8	8.1	415.5
	30	4.4	351.1	4.4	385.2	5.1	359.5	4.7	375.0
400	30	5.1	431.8	6.3	494.9	6.6	448.6	7.0	505.1
	40	3.3	425.5	3.4	422.6	3.9	431.8	4.3	459.6
640	30	9.7	697.4	9.1	718.3	10.7	701.9	11.2	774.4
	40	5.3	673.2	5.7	673.3	6.4	685.8	6.9	721.5
	50	4.3	672.5	3.5	676.0	4.5	671.1	4.0	683.4
800	40	7.2	837.4	6.5	853.2	8.1	856.3	7.3	865.3
	50	4.6	829.7	4.6	840.0	5.7	831.8	6.3	870.9
	60	3.7	823.4	3.4	817.6	3.8	822.7	4.3	842.5
Avg			461.7		497.4		465.1		507.8

Source: The author, 2023.

Figure 31 – Comparison of solutions obtained with $H = 100$ and $K = 10$ configuration for IP-1 and the respective simulated experimental data.



Source: The author, 2023.

and minus the standard deviation used to generate the simulated experimental data. The four results presented are obtained from the $H = 100$ and $K = 10$ configurations. Here the image is zoomed in to better showcase the difference among the configurations and how they fit the experimental data. The temperature simulated data in Figure 31b are not aligned because the position of the sensor is built in the τ_0 unknown, so its placement is also found by the optimization method. As expected, by applying the Morozov's Discrepancy Principle as stopping criterion, the temperature and radiation intensity profile lies within the experimental error standard deviation with reasonable confidence.

Table 19 – Average results for 50 independent executions of IP-2 with comparisons of Sobol Sequence (SS), Mersenne Twister (MT), Levenberg-Marquardt (LM) and Nelder-Mead (NM).

H	K	SS-LM		SS-NM		MT-LM		MT-NM	
		NNN	NFE	NNN	NFE	NNN	NFE	NNN	NFE
100	5	2.18	117.3	2.78	159.8	2.14	130.6	5.12	216.6
	10	1.52	110.5	1.40	135.0	1.42	112.3	1.64	143.0
200	5	3.52	220.4	3.82	270.2	2.74	247.4	8.56	377.3
	10	1.36	208.5	1.30	227.3	1.92	213.0	1.94	242.3
400	5	5.64	429.6	5.4	487.1	16.48	478.5	15.66	672.9
	10	1.58	408.3	1.64	431.3	2.50	413.8	2.56	446.2
	15	1.22	406.7	1.18	426.2	1.62	410.0	1.60	434.2
800	5	8.46	840.7	7.56	878.4	27.78	929.9	29.52	1190.8
	10	1.84	809.3	1.80	828.4	3.64	818.7	3.24	845.0
	15	1.50	807.8	1.22	819.5	1.78	809.6	1.70	830.2
	20	1.2	805.9	1.10	812.6	1.44	807.5	1.34	823.1
1600	10	2.6	1610.1	2.36	1628.6	4.64	1621.0	4.70	1642.1
	15	1.54	1607.5	1.44	1619.5	2.24	1610.7	2.44	1628.8
	20	1.36	1606.1	1.48	1615.2	1.42	1606.8	1.54	1617.5
	25	1.22	1604.6	1.22	1617.4	1.24	1606.2	1.28	1617.3
Avg			772.8		797.1		787.7		848.4

Source: The author, 2023.

4.5.2.2 Results for IP-2

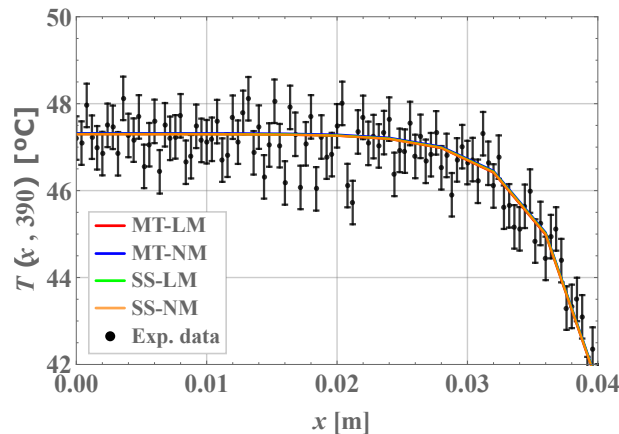
Table 19 shows the NFE obtained for IP-2. These results are the average of 50 independent executions of the TGO. This greater number of executions is necessary due to the increased amount of experimental data used for IP-2, which leads to greater discrepancies in the solution, even when the Morozov's Principle is achieved.

Again, the SS-LM combination produced the lowest NFE averages, as displayed in Table 19. TGO with SS point generator produced the best results for IP-2, for both LM and NM. Notice in the last lines of results, with $H = 1600$ starting points, the effort made in the local search phase is very small for both the LM and NM search. This is due to the fact that, in addition to TGO Step 2 returning fewer points with a high K , the search space with $H = 1600$ points is better sampled, thus finding great initial solutions for local search methods.

Figure 32 shows the temperature profile obtained for the configuration $H = 100$ and $K = 10$. In order to better visualize the differences of the methods, this profile is

presented only for $t = 390$ s and at the heated portion of the plate, i.e., $0 \leq x \leq 0.04$ m. The error bar represents the simulated experimental data standard deviation and, as it is possible to see, even though some of the experimental data lies outside of the curve, the four solutions obtained are reasonably consistent with each other.

Figure 32 – Comparison of solutions obtained with $H = 100$ and $K = 10$ configuration for IP-2 and the respective simulated experimental data.



Source: The author, 2023.

4.5.2.3 Results for IP-3

The inlet temperature function $f(y)$ - see Eq. 4.9 - is discretized with six points in its domain, which are the unknowns of the inverse problem. Then, they are linearly interpolated yielding a continuous function to be used in the direct problem. The choice of six points can be considered a small amount for a function estimation problem, however, since this problem is not formulated with any regularization, tests have shown that increasing the number of variables generated unwanted oscillations in the sought solution.

Table 20 presents the results as averages of 30 independent executions for IP-3. First of all, the reader can notice that the combinations with LM generated better results for every configurations (similarly to IP-2 and IP-3). Moreover, it is possible to see that this problem was more computationally expensive than IP-1 and IP-2, as the values for NFE are considerably higher for all the combinations, which is reasonable for a problem with more dimensions and a tendency to have a oscillatory solution.

Figure 33 shows the comparison among the four solutions obtained with the $H = 100$ and $K = 5$ configuration. In order to better visualize the difference, only the middle portion of the channel's height is presented since the peripheral temperature magnitude

Table 20 – Average results for 30 independent executions of IP-3 with comparisons of Sobol Sequence (SS), Mersenne Twister (MT), Levenberg-Marquardt (LM) and Nelder-Mead (NM).

H	K	SS-LM		SS-NM		MT-LM		MT-NM	
		NNN	NFE	NNN	NFE	NNN	NFE	NNN	NFE
100	5	15.86	307.2	16.70	536.4	16.50	315.5	16.86	574.4
	10	8.26	208.4	8.53	404.9	7.86	203.2	8.16	453.2
200	15	9.83	328.8	10.7	532.6	9.76	327.9	10.56	517.7
	20	6.76	288.9	7.13	481.3	7.00	292.0	7.30	504.7
400	25	12.33	561.3	12.23	697.4	11.63	552.2	12.16	707.9
	30	8.73	514.5	8.56	664.8	9.23	521.0	8.93	663.3
800	40	12.90	968.7	12.73	1066.8	14.16	985.1	13.13	1081.4
	45	11.26	947.4	11.03	1057.1	11.73	953.5	10.83	1059.6
	50	9.13	919.7	9.73	1089.5	9.70	927.1	9.46	1060.5
1600	60	16.46	1815.0	16.50	1907.9	17.23	1825.0	17.16	1931.1
	70	12.63	1765.2	12.90	1856.7	13.16	1772.1	12.56	1850.6
	80	9.96	1730.5	9.96	1839.1	10.86	1742.2	9.73	1878.8
Avg			862.96		1011.21		868.06		1023.60

Source: The author, 2023.

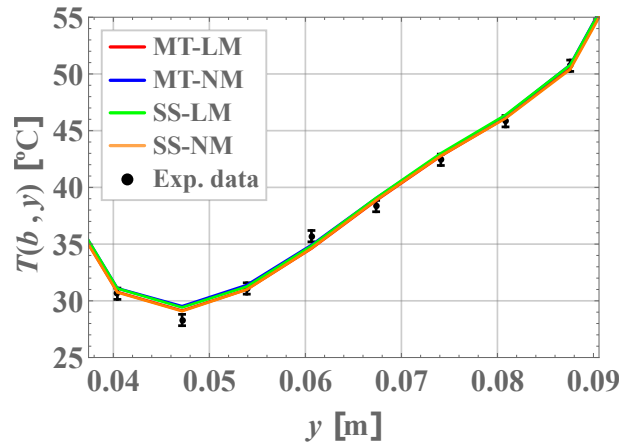
is large if compared to the simulated experimental data noise level. The fitted curve presented shows how each one of the configuration adjusted to the experimental data and, as expected due to the Morozov's Discrepancy Principle stopping criterion, they are very similar in behavior.

4.5.3 Wilcoxon signed ranks test

The comparison of the computational results presented in subsection 4.5.2 is performed with the Wilcoxon Signed Ranks Test - WSRT (129). This test allows to identify if there is a difference between two groups of results, observations or samples, i.e., it is a paired test that aims to detect significant differences between two samples (130).

This test is performed by taking the difference between two observations and ranking their absolute values in ascending order, i.e., the smallest gets the rank 1, the second smallest gets the rank 2 and so on. Draws receive averages ranks, e.g., if the second and third ranks have the same absolute difference value, they both receive the rank of 2.5. Consider that $T_{(+)}$ is the sum of all ranks obtained from positive differences, and $T_{(-)}$ the sum of ranks from negative differences. The statistical parameter T_s is defined as the smallest among $T_{(+)}$ or $T_{(-)}$ (131). If T_s is smaller than or equal to than the critical value

Figure 33 – Comparison of solutions obtained with $H = 100$ and $K = 5$ configuration for IP-3 and the respective simulated experimental data.



Source: The author, 2023.

Table 21 – Critical values T_w for the Wilcoxon Signed-Rank Test.

η	$\alpha = 15\%$	$\alpha = 5\%$	$\alpha = 2\%$	$\alpha = 1\%$
12	19	13	9	7
13	24	17	12	9
14	28	21	15	12
15	33	25	19	15
16	39	29	23	19
17	45	34	27	23
18	51	40	32	27

Source: Adapted from McCornack, 1965 (132).

T_w from the Wilcoxon distribution, then the null hypothesis H_0 is rejected, meaning that there is statistical difference between the two observations, but if T_s is greater than T_w , the null hypothesis is accepted and there is no difference between the observations.

A brief table of critical values for a two tailed test is displayed in Table 21, where α is the level of significance and η represents the degrees of freedom (132). The level of significance represents how much the null hypothesis describes the pair of observations - in other words, the null hypothesis indicates that the difference between observations has its center at zero.

Comparisons for IP-1. Table 22 shows the comparisons sums $T_{(+)}$ and $T_{(-)}$ obtained for the IP-1 - see Table 18. The combinations are presented as the differences calculated, for example, the line (SS-NM) – (SS-LM) represents the values from SS-NM minus the values from SS-LM in Table 18. So negative values in this example means larger

Table 22 – Wilcoxon Signed Rank Test for IP-1

Combination	$T_{(+)}$	$T_{(-)}$	T_s	H_0
(SS-NM) – (SS-LM)	0	136	0	$\alpha \leq 1\%$
(SS-NM) – (MT-LM)	0	136	0	$\alpha \leq 1\%$
(SS-NM) – (MT-NM)	25	111	25	$\alpha \leq 5\%$
(SS-LM) – (MT-NM)	127	8	8	$\alpha \leq 1\%$
(SS-LM) – (MT-LM)	41	94	41	—
(MT-NM) – (MT-LM)	3	133	3	$\alpha \leq 1\%$

Source: The author, 2023.

NFE for SS-LM. It is possible to see in Table 22 that, for IP-1, the SS-LM combination prevailed against all others, which was observed in Table 18. The comparison (SS-LM) - (MT-LM) presented in line 5 of Table 22 shows that there was no significant difference between the two combinations, in practice this means that the value of α would have to be greater than the maximum value of 15 % shown in Table 21. But between the combinations SS-NM and MT-NM, in line 3, presented a difference with $\alpha \leq 5\%$, which corroborates for the use of SS as the initial point generator.

Comparisons for IP-2. Table 23 presents the test parameters for IP-2. The reader can notice that there was no difference between SS-LM and MT-NM and this fact was not observed on IP-1. It appears that LM was much more competitive on IP-2 than on IP-1, leading to the conclusion that the surface of the IP-2 objective function favors the gradient-based method. Again, SS-NM generated the lowest NFE, with $\alpha \leq 1\%$ in all comparisons. An important observation for the IP-2 results is that the combination SS-LM has a better performance than the MT-LM with $\alpha \leq 1\%$, which was also not observed in IP-1. This comparison in IP-1 led to the acceptance of the null hypothesis, but here it contributes to the idea that SS has better characteristics to be used in Step 1 of TGO.

Comparisons for IP-3. Table 24 presents the test parameters for IP-3. It is clear that all the LM combinations were more efficient than the ones with NM as the local search method. In line 3 and line 5 of Table 24 the reader can see the difference of the random points generators SS and MT. These results go in favor of the use of SS in Step 1 of TGO, more specifically, these affirmations are drawn with 95% of confidence when used with LM and 85% with NM. In fact, the three inverse problems proposed in this work got the best results in general when SS was used.

Table 23 – Wilcoxon Signed Rank Test for IP-2

Combination	$T_{(+)}$	$T_{(-)}$	T_s	H_0
(SS-NM) – (SS-LM)	17	136	17	$\alpha \leq 1\%$
(SS-NM) – (MT-LM)	13	140	13	$\alpha \leq 1\%$
(SS-NM) – (MT-NM)	22	131	22	$\alpha \leq 1\%$
(SS-LM) – (MT-NM)	106	47	47	—
(SS-LM) – (MT-LM)	19	134	19	$\alpha \leq 1\%$
(MT-NM) – (MT-LM)	15	138	15	$\alpha \leq 1\%$

Source: The author, 2023.

Table 24 – Wilcoxon Signed Rank Test for IP-3

Combination	$T_{(+)}$	$T_{(-)}$	T_s	H_0
(SS-NM) – (SS-LM)	78	0	0	$\alpha \leq 1\%$
(SS-NM) – (MT-LM)	78	0	0	$\alpha \leq 1\%$
(SS-NM) – (MT-NM)	19	59	19	$\alpha \leq 15\%$
(SS-LM) – (MT-NM)	0	78	0	$\alpha \leq 1\%$
(SS-LM) – (MT-LM)	13	65	13	$\alpha \leq 5\%$
(MT-NM) – (MT-LM)	78	0	0	$\alpha \leq 1\%$

Source: The author, 2023.

4.6 Conclusions

The method known as Topographical Global Optimization was used to solve three heat transfer inverse problems. The solution of these problems served as a framework in order to compare combinations of TGO when implemented with different point generators and local search methods, namely Mersenne Twister (MT), Sobol Sequence (SS), Nelder-Mead (NM) and Levenberg - Marquardt (LM).

Results were compared using the Wilcoxon Signed Ranks Test, which supported the hypothesis that the Sobol Sequence is the best point generator to be used with TGO when dealing with these types of inverse problems. For the problems of this work, LM was more efficient than the NM algorithm. This is due to the implementation options chosen. The NM method initialized independently for every TGO point resulted in an increased computational cost. Therefore, the choice of the local search method turnout to be very important, as different styles of methods will behave differently on certain objective functions.

Moreover, the results highlighted that the Sobol Sequence can stand out when

larger number of initial points are used. This is in agreement with the literature and corroborates with the fact that there is, in fact, differences on the outcome of the TGO when used with distinct point generators. Therefore the choice of SS in this initial step is recommended.

TGO is a simple algorithm and only requires the configurations of the number of initial points and the number of closest neighbors to be analyzed, parameters which can be tuned very intuitively (the local search methods also have its own parameters, but information about them are usually readily available on the literature). It is also an advantage of TGO that it can be implemented in parallel. Once the vector of starting points is determined through the generator, whether MT, SS or any other, the process of calculating the objective function at these points can take place in different processing cores, which is an approach that can be further investigated.

5 COMPUTATIONAL INTELLIGENCE AND TIKHONOV REGULARIZATION WITH REDUCED DIMENSION MODEL: APPLICATIONS IN HEALTH, RENEWABLE ENERGY AND CLIMATE HEAT TRANSFER INVERSE PROBLEMS

5.1 Introduction

Inverse problems can be formulated as minimization problems, where an objective function is defined as the sum of the squared differences between information calculated with a model and experimental data, which corresponds to the maximum likelihood approach (5). The class of inverse problems that deals with function estimation is often ill-posed due to the presence of noise on the data used as input (5, 6, 133, 134). Such experimental noise is amplified and generates undesired oscillations on the obtained solution, making it very difficult to retrieve any useful information and, to overcome this problem, the classical technique known as Tikhonov Regularization (76) can be used. This technique works by adding a term to the objective function which penalizes oscillatory solutions. This term comes multiplied by a positive non-zero scalar, namely the Tikhonov regularization parameter λ . The fine tuning of λ is crucial to the outcome of the method: if λ is too large, only over regularized solutions will prevail, on the other hand, if it is too small, not enough regularization will happen, and the solution will still be too oscillatory.

Therefore, the solution of the inverse problem may incorporate itself the search of an adequate value for the regularization parameter. To do so, several methods have been proposed along the years, such as the L-curve method (82, 83), Morozov's Discrepancy Principle (85), Fixed Point Iteration method (84), among others. For a more detailed review of these methods, the reader can see the work of Hansen (135).

In this chapter we focus on the Fixed Point Iteration method (FP), as proposed by Bazán (84). This method does not require previous information on the experimental error variance and works by finding the parameter λ that balances the values of the objective function terms, i.e., the residue and the regularization term (136). The FP finds the best λ by reaching the convergence of a series where each new term is calculated by solving the inverse problem with the previous λ . When convergence is reached, the newly found λ is considered the optimal one. In practice, the iterative process stops when a small prescribed tolerance is reached.

Although FP is very efficient, it obviously can be affected by the number of dimensions of the problem, i.e., the number of points used to represent the sought function. In this chapter we present a technique to find an estimate for the best value of λ in a problem with a large number of variables by solving an alternative problem with reduced order, i.e., smaller number of dimensions. This low order solution is extrapolated in order to find an estimate for the complete problem regularization parameter λ and, then, this estimate is used as an initial value to restart the series. Furthermore, when divergence is detected on the series, no value of λ can be retrieved. Bazán (84), the author of the method, suggested different approaches to overcome this problem, but in this chapter we present a step-by-step algorithm based on the recent work of Aucejo and De Smet (137), which introduced an idea to overcome this problem based on the objective function terms values.

The methodology developed in this work is demonstrated in three inverse heat transfer problems with potential practical applications in bioengineering, renewable energy and climate, as follows:

- **Identification of spatially variable thermal conductivity of biological tissues**
 The bioheat transfer model proposed by Pennes (138) is used in a steady-state condition to predict the thermal conductivity of tissues. Thermal techniques and their analysis are common in the treatment of cancer (139, 140), laser ablation procedures (141) and even brain related diseases therapy (142), to name a few. Furthermore, using this model with spatially variable thermal conductivity of biological tissue has attracted the attention of the scientific community (143, 144, 145, 146).
- **Estimation of spatially variable inlet temperature profiles in parallel plates channel**
 The model used takes into account the velocity field of a fluid inside a parallel plates channel. The heat transfer process by convection considered has many applications in the design of optimal heat exchangers, energy transformation, micro system mechanisms development, among many others. Spatially variable inlet temperature profiles may be of special interest in micromixers.
- **Spatially dependent single scattering albedo**
 The process of radiative transfer is investigated in steady state for one dimensional participating media. Such problem, related model and analysis is of great importance in many areas of interest (72, 147,

148, 149, 150), including those related to climate research, such as atmospheric and oceanic models (60), oceanography (151) and atmosphere studies (152).

Such problems and corresponding applications are in alignment with the Sustainable Development Goals (SDG) 3, 4, 7, 9, 13 and 17 of the United Nations 2030 Agenda established in 2015.

5.2 Fixed Point Iteration method with reduced model

Consider an inverse problem formulated with the maximum likelihood approach. This formulation leads to a minimization problem where the squared norm of the difference between the vectors of observed data and values obtained from a model must be minimized. This objective function can be written as

$$Q(\mathbf{u}) = \|\mathbf{T}^{\text{exp}} - \mathbf{F}(\mathbf{u})\|^2 \quad (5.1)$$

where \mathbf{u} is the vector of unknown parameters, \mathbf{T}^{exp} is the vector of experimental data, $\mathbf{F}(\mathbf{u})$ is the vector of values obtained with the mathematical model, and the operator $\|\cdot\|$ is the l_2 Euclidean norm.

When a function intrinsic to the model \mathbf{F} is unknown and must be estimated, one possible approach is to represent this function as linearly interpolated discrete points, where such points compose the vector \mathbf{u} in Eq. 5.1. This formulation of the inverse problem is often ill-posed and the solutions obtained for \mathbf{u} may contain heavy oscillations (36, 72, 153).

The Tikhonov Regularization (TR) is one of the many techniques proposed to overcome this problem (5, 134, 154). It consists on adding a term to the objective function Q that penalizes oscillating solutions of \mathbf{u} . The modified Eq. 5.1 with the regularization term is written as

$$Q(\mathbf{u}) = \|\mathbf{T}^{\text{exp}} - \mathbf{F}(\mathbf{u})\|^2 + \lambda^2 \|\mathbf{L}\mathbf{u}\|^2 \quad (5.2)$$

where λ is the regularization parameter, and \mathbf{L} is the derivative operator matrix. Particularly, we call the term $\|\mathbf{T}^{\text{exp}} - \mathbf{F}(\mathbf{u})\|$ as the residue norm and $\|\mathbf{L}\mathbf{u}\|$ as the regularization norm.

The derivative operator \mathbf{L} can be of zero, first or second order: this choice depends on desired aspects of the sought solution (84, 136). The regularization parameter λ controls

the balance between how much regularized the solution must be (154), in other words, if λ is large, the solution will tend to be constant (over regularized) and, on the other hand, if λ tends to zero, no regularization is performed.

The following subsections explain the Fixed Point Iteration method (FP) used to calculate the optimal value of λ , and how it is possible to perform the associated iterative procedure using a simpler version of the inverse problem, i.e., using a lower dimension vector of unknowns \mathbf{u} .

5.2.1 The Fixed Point Iteration method (FP)

The main idea of FP is to select the value of λ that minimizes the product between the residue norm and the regularization norm as a function of λ (136). This minimization corresponds, in other words, to the value of λ that balances the two terms growth. The iterative process is built with the expression

$$\lambda_{i+1} = \sqrt{\phi} \frac{\|\mathbf{T}^{\text{exp}} - \mathbf{T}(\mathbf{u})\|}{\|\mathbf{L}\mathbf{u}\|} \Big|_{\lambda_i}, \quad i = 0, 1, 2, \dots \quad (5.3)$$

where $\phi > 0$ is a parameter that plays a role on the convergence of the series, and the residue and regularization norms are obtained from the solution of the inverse problem with the previous value for the regularization parameter, i.e. λ_i . Therefore, it is necessary to perform the optimization cycle in order to obtain the next term of the sequence.

A few aspects of this technique must be pointed out. First of all, to start the series, the author of the method suggests in Ref. (84) that the initial regularization parameter should be close to zero, i.e., $\lambda_0 \rightarrow 0^+$. Furthermore, it is possible that the series fails to converge. Initially, it is suggested to use $\phi = 1$ as an initial choice and, if divergence is detected, ϕ must be updated to overcome this problem. Bazán (84) proposed different ways for this parameter tuning, but in this chapter we use the approach recently proposed by Aucejo and De Smet (137), which takes into account the balance of the terms of the objective function, and does not require any information of the physical problem. We implemented this approach with some modifications on the stopping criterion, but the core of the actualization of ϕ holds, as shown in Algorithm 4 next:

Algorithm 4: Fixed Point Iteration method with adapted stopping criterion

- 1: Set $\phi = 1$.
 - 2: Set $i = 0$, $\lambda_0 \rightarrow 0^+$, and $R_0 \rightarrow 0^+$.
 - 3: Compute λ_{i+1} with Eq. 5.3.
 - 4: Compute the ratio $R_{i+1} = \lambda_i^2 \frac{\|\mathbf{L}\mathbf{u}\|^2}{\|\mathbf{T}^{\text{exp}} - \mathbf{T}(\mathbf{u})\|^2} \Big|_{\lambda_i}$.
 - 5: Compute $\Delta = R_{i+1}/R_i$.
 - 6: If $\Delta < 1$, the series is considered divergent, then make $\sqrt{\phi} = \sqrt{R_i}$, and restart the process from Step 2, otherwise, go to Step 7.
 - 7: If $\Delta - 1 \leq \epsilon$, the series is considered convergent, λ_{i+1} is the optimal regularization parameter, and the iterative process is stopped.
Otherwise, make $i = i + 1$, and go to Step 3.
-

where ϵ is a relatively small prescribed tolerance. Here it is important to make a few remarks. The first term R_1 will most likely be very small because $\lambda_0 \rightarrow 0^+$. Furthermore, the sequence R_i increases until divergence is detected on Step 6. This indicates that the regularization parameter is increasing and making the regularization norm decrease to a point that it is not balanced with the residue norm.

Algorithmically, we introduce a stopping criterion on the convergence of the ratio R on Step 7, which corresponds to the convergence of λ , whereas Aucejo and De Smet (137) suggested a stopping criterion on the convergence of ϕ , which is a robust option, despite being more computationally expensive.

5.2.2 The Reduced Dimension Model approach

The objective of this approach is to find an estimate for the initial value of λ to start the algorithm presented in Sec. 5.2.1, by solving the inverse problem with a coarser discretization of the sought function, i.e., a lower dimension vector \mathbf{u} , identified as \mathbf{u}_{low} . Once the corresponding optimal regularization parameter λ_{low} and the regularized solution \mathbf{u}_{low} are determined, the initial regularization parameter λ_{high} for a problem with higher dimension can be estimated by equalizing the regularization norms with their respective regularization parameters, yielding

$$\lambda_{\text{low}}^2 \|\mathbf{L}\mathbf{u}\|_{\text{low}}^2 = \lambda_{\text{high}}^2 \|\mathbf{L}\mathbf{u}\|_{\text{high}}^2 \quad (5.4)$$

where "low" and "high" are the indexes indicating the lower and the higher dimension inverse problem, respectively. Then:

$$\lambda_{\text{high}} = \lambda_{\text{low}} \frac{\|\mathbf{L}\mathbf{u}\|_{\text{low}}}{\|\mathbf{L}\mathbf{u}\|_{\text{high}}} \quad (5.5)$$

where λ_{low} and $\|\mathbf{L}\mathbf{u}\|_{\text{low}}$ are known from the solution of the lower dimension problem. The matrix \mathbf{L}_{high} is simply the finite difference operator with the corresponding dimension. Yet to be determined is the term \mathbf{u}_{high} . Here some assumptions must be introduced, since we do not have any solution \mathbf{u} obtained with the the high dimension model. The suggestion is to perform a linear interpolation of \mathbf{u}_{low} in order to generate \mathbf{u}_{high} .

Now it is possible to evaluate the whole expression given by Eq. 5.5 to obtain an initial value for λ_{high} , since all the terms on the right-hand side are determined. In terms of computational cost, this can be of great advantage if the estimated value of λ_{high} is reasonably good, meaning that the higher dimension problem will be solved fewer times.

Another important aspect of this approach is the choice of the dimension size for \mathbf{u}_{low} . A small dimension size will lead to an easier problem to optimize, but relevant information of the real solution can be lost, which can lead to a poor estimate for λ_{high} . On the other hand, if this dimension is increased, the problem will become more cumbersome to solve, since more variables are included, leading to higher computational time and, therefore, more severe regularization issues.

5.3 Direct Problems

In this Section, the three Direct Problems of interest in this work are presented. As already mentioned, the first one is concerned with the bioheat transfer in steady state regime on a biological tissue with spatially variable thermal conductivity in order to model different layers. The second problem deals with the inlet temperature profile of a fluid inside a parallel plate channel aiming at applications in microchannels. The third problem addresses the radiative transfer problem in participating media, in which the spatially variable single scattering albedo must be reconstructed.

5.3.1 Direct Problem 1: Spatially varying thermal conductivity of a biological tissue

The bioheat transfer model given by Pennes' equation (138) is a well established approach in determining the temperature field of biological tissues (143). In this chapter, we consider the steady-state model with one spatial dimension. Also, the thermal conductivity $k(x)$ is modeled as a spatially dependent parameter, i.e., it varies across the different types of tissues. As presented in Figure 34, there is heat exchange with the ambient at $x = 0$, and no external heating. The Pennes' model, in such conditions, can be written as

$$\frac{d}{dx} \left[k(x) \frac{dT(x)}{dx} \right] + \omega_b \rho_b c_b [T_b - T(x)] + q_m = 0 \quad (5.6a)$$

$$-k(x) \left. \frac{dT(x)}{dx} \right|_{x=0} = h [T_\infty - T(x)|_{x=0}] \quad (5.6b)$$

$$\left. \frac{dT(x)}{dx} \right|_{x=L} = 0 \quad (5.6c)$$

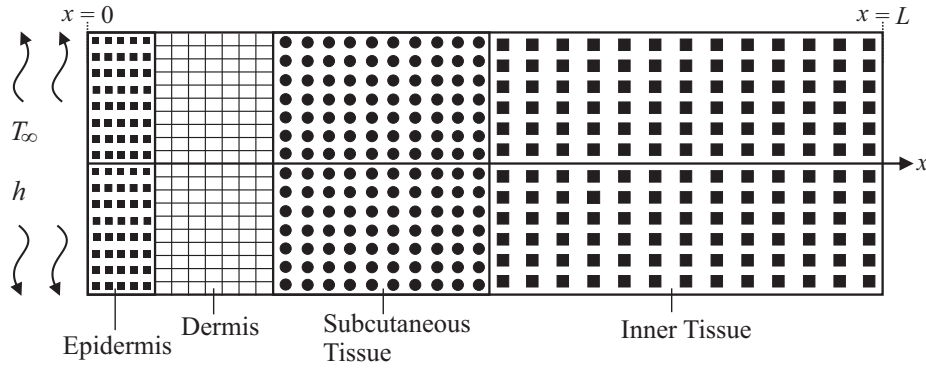
where ω_b is the blood perfusion parameter, ρ_b and c_b are the specific mass and specific heat of the blood, respectively, T_b is the blood temperature, q_m is the internal heat generation due to metabolic activity, L is domain length, T_∞ is the ambient temperature, and h is the heat transfer coefficient of the convection phenomenon at $x = 0$.

The problem given by Eq. 5.6 is solved using the built-in "NDSolve" routine of the Wolfram Mathematica software with the Implicit Runge Kutta method option (80), and fixed step size. The spatially varying thermal conductivity is considered constant for each tissue, and, therefore, this can be implemented as a step function, i.e. constant by parts. In this chapter we use an exponential approximation to write this step function as a continuous function, in order to avoid stiffness of the numerical solution.

5.3.2 Direct Problem 2: Inlet temperature profile in a parallel plates channel

Consider the problem of determining the steady state temperature field of a hydrodynamically developed and thermally developing fluid inside a two parallel plates channel subjected to a constant heat flux q at both boundary plate surfaces, as schematically presented in Figure 35. Neglecting viscous dissipation, free convection and the axial conduction effects, the mathematical formulation that describes the temperature field

Figure 34 – Schematic representation of the heterogenous biological tissue.



Source: Adapted from Cotta et al., 2010 (143).

$T(x, y)$ can be written as (123, 125, 155).

$$k \frac{\partial^2 T(x, y)}{\partial y^2} = v(y) \rho c_p \frac{\partial T(x, y)}{\partial x} \quad (5.7a)$$

$$k \frac{\partial T(x, y)}{\partial y} \Big|_{y=H} = q \quad (5.7b)$$

$$-k \frac{\partial T(x, y)}{\partial y} \Big|_{y=0} = q \quad (5.7c)$$

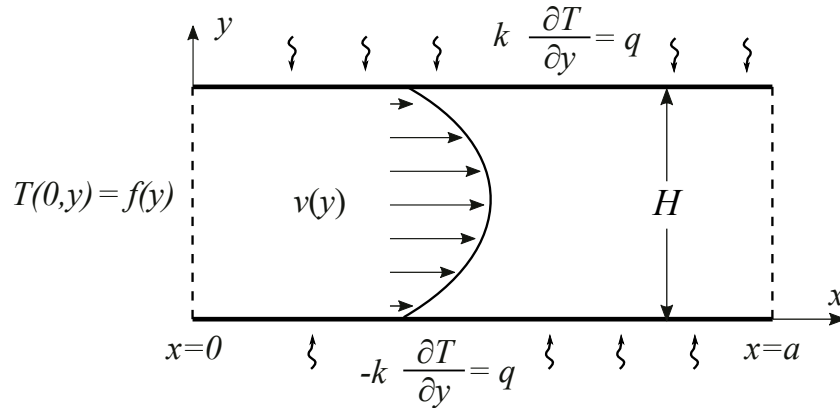
$$v(y) = 6v_m \frac{y}{H} \left(1 - \frac{y}{H}\right) \quad (5.7d)$$

$$T(0, y) = f(y) \quad (5.7e)$$

where the thermophysical parameters k , ρ and c_p are the thermal conductivity, and specific mass and specific heat, respectively. The parameter v_m is the average velocity of the fluid inside the channel.

The problem described by Eq. 5.7 is also solved using the built-in "NDSolve" routine of the Mathematica software (80). Here, the Finite Element Method option is used, and the mesh generated to discretize the domain is rectangular with all the elements having the same dimensions, i.e., the mesh is uniform. In this approach, the velocity field $v(y)$ and the inlet temperature $f(y)$ are implemented as continuous functions, and, therefore, the discretization needed to solve the differential equation is performed automatically by

Figure 35 – Schematic representation of the two parallel plates channel showing the transversal coordinate spatially dependent fluid velocity.



Source: Adapted from Bokar and Ozisik, 1995 (125).

the routine.

5.3.3 Direct Problem 3: Radiative transfer with variable space dependent scattering albedo

Consider a steady-state regime for an one-dimensional medium that absorbs, emits and scatters radiation isotropically. The spatial coordinate (optical variable) and the optical thickness are represented by $\tau = \beta x$ and $\tau_0 = \beta L$, respectively, where β is the extinction coefficient, and x and L are the physical spatial coordinate and total length of the medium, respectively. External incident radiation with isotropic constant intensities A_1 at $\tau = 0$ and A_2 at $\tau = \tau_0$ are considered as shown in Figure 36.

The mathematical formulation of the steady-state radiative transfer problem, for a given wavelength, considering the case of azimuthal symmetry, isotropic scattering, and neglecting the radiation emission by the medium, is given by the linear version of the Boltzmann equation (77),

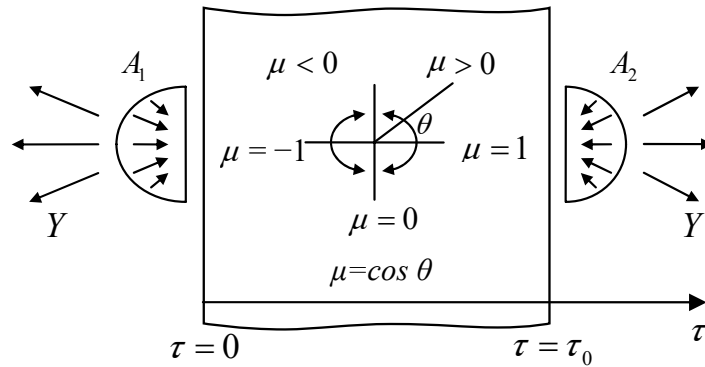
$$\mu \frac{\partial I(\tau, \mu)}{\partial \tau} + I(\tau, \mu) = \frac{\omega(\tau)}{2} \int_{-1}^1 I(\tau, \mu') d\mu' \text{ in } 0 < \tau < \tau_0, \quad -1 \leq \mu \leq 1 \quad (5.8a)$$

$$I(0, \mu) = A_1 \text{ for } \mu > 0 \quad (5.8b)$$

$$I(\tau_0, \mu) = A_2 \text{ for } \mu < 0 \quad (5.8c)$$

where μ is the cosine of the polar angle θ , i.e., the angle of the radiation beam with the

Figure 36 – Schematic representation of a radiative transfer participating medium. Here Y represents the exit radiation intensity at both boundaries of the medium.



Source: Adapted from Silva Neto e Silva Neto, 2003 (156).

positive τ axis, and $\omega(\tau)$ is the spatially varying single scattering albedo.

The solution of the radiative transfer problem given by Eq. 5.8 is obtained using Chandrasekhar's discrete ordinates method (78), in which the angular domain is discretized and the integrals replaced by Gauss-Legendre quadratures, as performed in (2, 5, 54, 72, 79, 81, 150). The built-in routine "NDSolve" (80) of the Wolfram Mathematica software (80) is then used to solve the system of differential equations generated by this discretization, with the method set as automatic, and a precision goal of 10^{-4} in order to control the computational cost in obtaining the radiative transfer problem solution.

5.4 Inverse Problems

The Inverse Problem 1 (IP-1) consists of estimating the thermal conductivity $k(x)$ in Eq. 5.6. The Inverse Problem 2 (IP-2) is formulated similarly to IP-1, but here we are interested in estimating the inlet temperature profile $f(y)$ in Eq. 5.7e. Lastly, in the Inverse Problem 3 (IP-3) the varying scattering albedo $\omega(\tau)$ in Eq. 5.8a is considered unknown, and must be determined.

For the three cases, the corresponding vector of unknowns, here called \mathbf{u}_1 , \mathbf{u}_2 and \mathbf{u}_3 , contains values of the sought function at discrete points of the computational domain, which can be represented as

$$\mathbf{u}_1 = \{k_1, k_2, \dots, k_n\}^T, \quad k_1 = k(x_1), k_2 = k(x_2), \dots, k_n = k(x_n) \quad (5.9a)$$

$$\mathbf{u}_2 = \{T_1, T_2, \dots, T_n\}^T, \quad T_1 = f(y_1), T_2 = f(y_2), \dots, T_n = f(y_n) \quad (5.9b)$$

$$\mathbf{u}_3 = \{\omega_1, \omega_2, \dots, \omega_n\}^T, \quad \omega_1 = \omega(\tau_1), \omega_2 = \omega(\tau_2), \dots, \omega_n = \omega(\tau_n) \quad (5.9c)$$

where n is the total number of points used in the discretization of the sought function within the physical medium domain.

In order to simulate the experimental measurements required for the solution of each one of the inverse problems considered, noise is added to the solution of the respective direct problem using the exact values for the unknown functions that will be determined:

$$T_i^{1,\text{exp}} = T(x_i^{\text{exp}}, k^*) + v_1, \quad v_1 \sim N(0, \sigma_1^2), \quad i = 1, 2, \dots, N_1 \quad (5.10a)$$

$$T_i^{2,\text{exp}} = T(x_i^{\text{exp}}, y_i^{\text{exp}}, f^*) + v_2, \quad v_2 \sim N(0, \sigma_2^2), \quad i = 1, 2, \dots, N_2 \quad (5.10b)$$

$$I_i^{\text{exp}} = I(\tau_0, \mu_i^{\text{exp}}, \omega^*) + v_3, \quad v_3 \sim N(0, \sigma_3^2), \quad i = 1, 2, \dots, N_3 \quad (5.10c)$$

where for IP-1, IP-2 and IP-3, the subscript 1, 2 and 3 holds, respectively, for the total number of experimental data N , and the random numbers v drawn from a normal distribution centered at zero with standard deviation σ . $T^{1,\text{exp}}$, $T^{2,\text{exp}}$ and I^{exp} represent the simulated (synthetic) experimental data to be used for the corresponding inverse problems, i.e. IP-1, IP-2 and IP-3, respectively. The terms k^* , f^* and ω^* represent the exact thermal conductivity, inlet temperature and single scattering albedo functions, respectively. Then, the objective functions are formulated similarly as presented in Eq. 5.2, where, for each inverse problem, the respective direct problem model is used.

5.5 Results and Discussion

To obtain the solutions of the inverse problems, the optimization is performed initially with a combination of both the Differential Evolution (DE) (24) and the Nelder-Mead (NM) (101) methods. For every solution obtained, DE starts with a random population of five times the dimension of \mathbf{u} , i.e. $5 \times n$. The crossover probability CR and the scaling factor W , i.e. control parameters for DE, are set as $CR = 0.25$ and $W = 0.85$. The DE method stops when a number of internal loops, which is specific for each problem, are completed, and, then, all the points from DE are used to start the NM simplex method. The NM reflection, expansion, contraction and shrink coefficients are set as 1.0, 2.0, 0.5

and 0.5, respectively. The iterative procedure of NM is stopped when

$$100 \times \frac{\max(\mathbf{F}) - \min(\mathbf{F})}{\bar{F}} \leq \gamma \quad (5.11)$$

where \mathbf{F} is the vector of objective function values for each NM point, \bar{F} is the calculated mean of such values, and γ a relative small tolerance defined by the user. This dimensionless stopping criterion represents the percentage of how the values of \mathbf{F} are spread relative to its average values, making it more reasonable to use across the three different inverse problems.

5.5.1 Results for the Inverse Problem 1 (IP-1)

The values of the parameters for the bioheat model are obtained from the literature (143, 157). Such values are displayed in Table 25. Experimental data are simulated in the range $0 \leq x \leq L$ with steps of $\Delta x = L/200$, which in a real application can be obtained experimentally with the Photoacoustic Thermography (124, 158) or near-field microwave radiometry techniques (159), for instance. The exact calculated temperatures are corrupted with a noise level of $\sigma_1 = 0.05$ °C in Eq. 5.10a. In order to damp these errors, and make the retrieval of the sought function more robust, we applied the Total Variation filter (TV) on the simulated experimental data (154). This filtering method requires the definition of its own regularization parameter, which was obtained in such way to satisfy the following criterion

$$SD(TV(\mathbf{T}^{1,\text{exp}}) - \mathbf{T}^{1,\text{exp}}) = \sigma_1 \quad (5.12)$$

where SD and TV are the standard deviation and Total Variation functions, respectively, leading to a TV regularization parameter of 1.25.

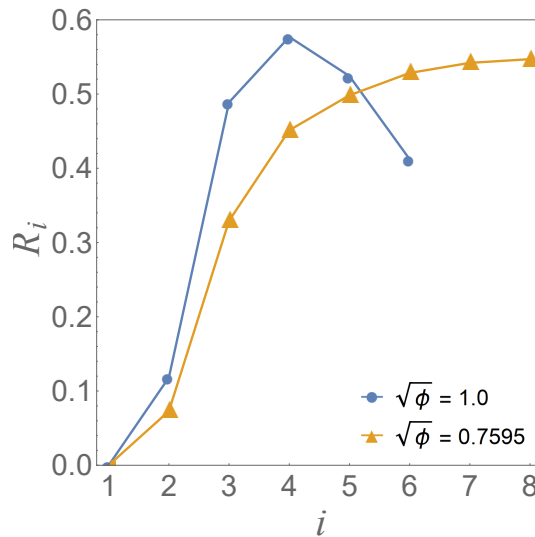
The epidermis layer was neglected due to its small thickness, thus not influencing the quality of the results exposed in this subsection (143). Therefore, the exact thermal conductivity function considered in this work has three constant step values: $k_1 = 0.45$ W/m K in $0 \leq x < 0.002$ m for the dermis, $k_2 = 0.19$ W/m K in $0.002 \leq x < 0.012$ m for the subcutaneous tissue and $k_3 = 0.50$ W/m K in $0.012 \leq x \leq L$ for the inner tissue. All the searches are performed considering the stopping criterion tolerance $\gamma = 0.001$, see Eq. 5.11, the search region bounds of $0.1 \leq \mathbf{u}_1 \leq 0.8$ W/m K and 20 internal loops in DE.

Table 25 – Exact values of the parameters for the Direct Problem 1 (DP-1).

Parameter	Value	Dimension	Description
L	0.042	[m]	Sample thickness
c_b	3770.0	[J/kg K]	Blood specific heat
ρ_b	1060.0	[kg/m ³]	Blood specific mass
T_b	37.0	[°C]	Blood temperature
ω_b	0.00125	[m ³ /s m ³]	Blood perfusion coefficient
q_m	420.0	[W/m ³]	Metabolic heat generation
T_∞	20.0	[°C]	Ambient temperature

Using an initial parameter of $\sqrt{\phi} = 1.0$, see Eq. 5.3, and Algorithm 1, divergence was detected at the 4th iteration, as can be seen in the behavior of the R_i sequence in Figure 37 (solid dots), which changes its growth path at the 4th iteration. The process then restarted with $\sqrt{\phi} = 0.7595$ - notice in Figure 37 the converging behavior of this R_i sequence (solid triangles). The series with $\sqrt{\phi} = 0.7595$ is considered converged with $|\Delta - 1| = 0.0092$, which is ≤ 0.01 (see Step 7 in Algorithm 1).

Figure 37 – Evolution of the sequence R_i for the low dimension model with $n = 7$ showing the divergent sequence for $\sqrt{\phi} = 1.0$, and the convergent sequence of the found $\sqrt{\phi} = 0.7595$.



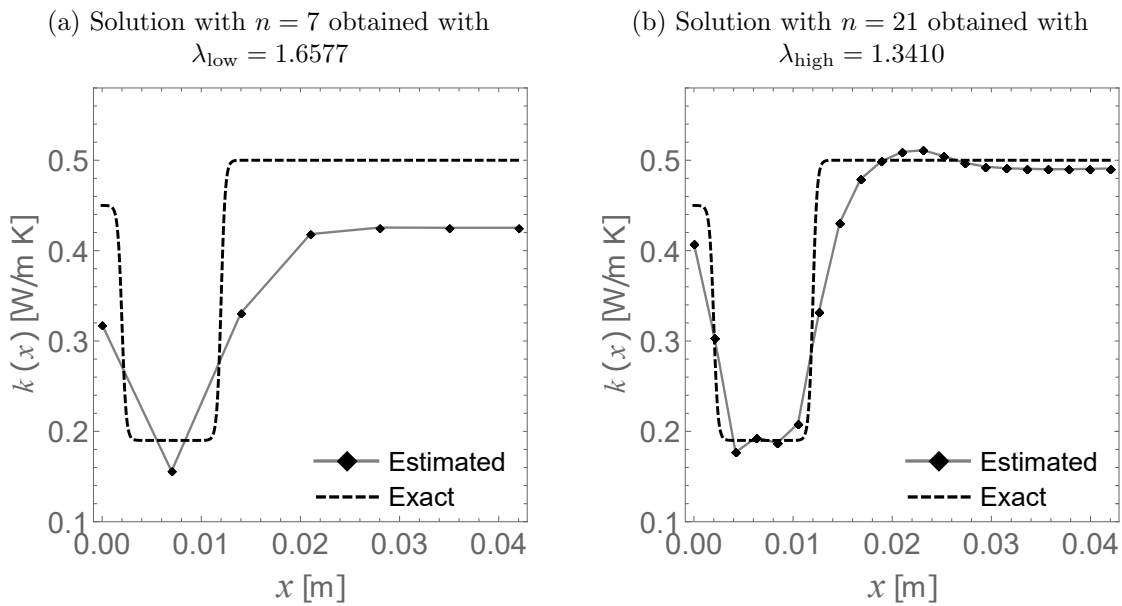
Source: Jardim et al., 2022 (160).

Using this value of $\sqrt{\phi}$ for $n = 7$, the regularization parameter obtained was $\lambda_{\text{low}} = 1.6577$, and the solution obtained for IP-1 is displayed in Figure 38a. It is possible to observe that the estimation is in general poor, but mainly in $0.012 \leq x \leq L$. This may be due to two facts: the coarse mesh of points used to discretize the sought function, and

a lack of sensitivity, specially in the region of the domain farther from the surface.

Nevertheless, this low order solution generated an initial regularization parameter for the high dimension model with $n = 21$ of $\lambda_{\text{high}} = 3.3650$ calculated according to Eq. 5.5. Keeping $\sqrt{\phi} = 0.7595$, the process restarts with the new λ and convergence is obtained on the 5th iteration, with $\lambda = 1.3410$. Finally, the recovered thermal conductivity obtained with $\lambda = 1.3410$ is presented in Figure 38b, where it is possible to see the improvement in the quality of the estimation all over the physical domain.

Figure 38 – Solutions for IP-1 with the low dimension model (a) that generated the estimative for the regularization parameter of the high dimension model (b)



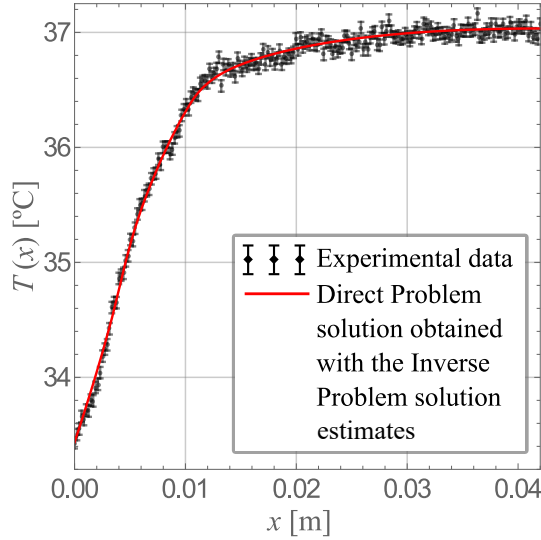
Source: Jardim et al., 2022 (160).

In Figure 39 the temperature profile obtained with the solution of the inverse problem with $n = 21$ points is displayed with the simulated experimental data. The error bars of $0.05\text{ }^{\circ}\text{C}$ correspond to the added noise standard deviation used to generate the simulated data. In such figure, it is possible to notice the good agreement of the temperature profile obtained with the simulated experimental data, specially in the regions of the dermis and the subcutaneous tissue, i.e. $0.00 \leq x \leq 0.012\text{ m}$.

5.5.2 Results for the Inverse Problem 2 (IP-2)

The fluid considered for Problem 2 is air ($k = 0,0265\text{ W/m K}$, $\rho = 1.1614\text{ kg/m}^3$, $c_p = 1007.0\text{ J/kg.K}$), and the experimental data are acquired with 101 evenly distributed

Figure 39 – Simulated experimental data and temperature profile obtained with the solution of IP-1 with $n = 21$.



Source: Jardim et al., 2022 (160).

points in the y direction at the horizontal position of $x = a/5$, with $a = 0.635$ m, representing an acquisition of temperature measurements that can be achieved in real experiments by the use of infrared thermography (161). The imposed heat flux and average fluid velocity are $q = 500$ W/m² and $v_m = 0.025$ m/s. In this chapter, the exact inlet temperature profile $f(y)$ is a step function, which represents a stratified flow of magnitude 26.85 °C in $0 < y \leq H/2$ and 46.85 °C in $H/2 < y \leq h$, with $H = 0.128$ m. The experimental noise is then added to the exact solution by using a noise level of $\sigma_2 = 0.5$ °C in Eq. 5.10b. Since the direct solution is less computationally intensive, DE is set to perform 100 internal loops, and NM stopping criterion as $\gamma = 0.005$ in Eq. 5.11. The search space bounds considered for every point ranges from -73.15 °C to 326.85 °C.

Using $\sqrt{\phi} = 1$, every test performed for IP-2 converged. For this problem, we present in Table 26 the obtained values for the low dimension model and comparisons with their respective estimates for λ_{high} . Also in Table 26, the values of $\lambda_{21} = 0.4923$ and $\lambda_{31} = 0.5957$ were obtained without the auxiliary reduced model.

As it is possible to observe in Table 26, the estimations for λ_{high} gets closer to the value found by solving the high dimension problem itself. This is expected since the error of the approximation reduces when the dimensions of lower and higher order are closer. Another point to be noticed is that the regularization parameter found for $n = 7$ generated

Table 26 – Results obtained for several values for the low dimension model λ , and their respective λ_{high} estimates for IP-2.

n	λ_{low}	$\lambda_{21} = 0.4923$	$\lambda_{31} = 0.5957$
6	0.2280	0.4570	0.5597
7	0.3232	0.6263	0.7225
8	0.2807	0.5135	0.5998
9	0.3030	0.5119	0.6048
10	0.3249	0.4996	0.6017
11	0.3402	0.4809	0.5893
12	0.3509	0.4957	0.5991
13	0.3753	0.5052	0.6050

Source: Jardim et al., 2022 (160).

the highest value of λ_{high} . One possible way to explain this is due to the choice of the points in the physical domain, where the error increases depending on how the points are allocated.

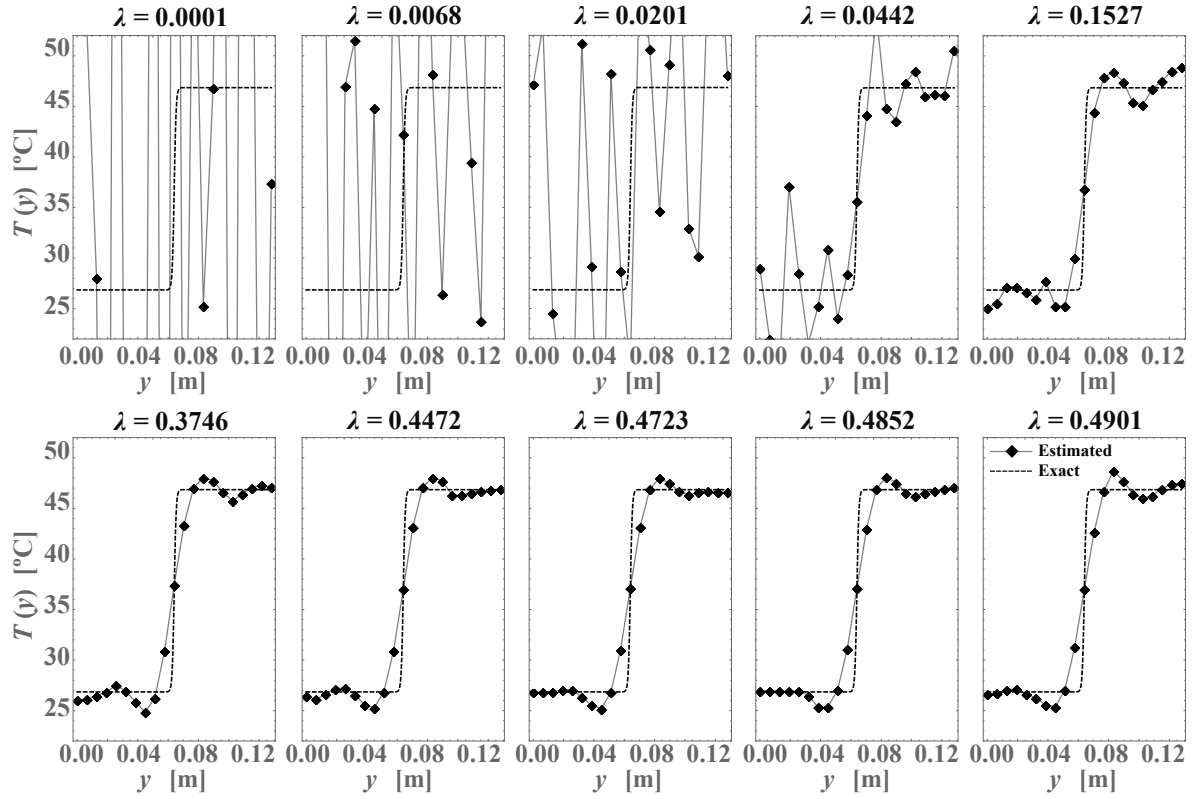
Figure 40 shows the solutions obtained for $n = 21$ starting from $\lambda_0 = 0.0001$ (obtained without the auxiliary low dimension problem). It is noticeable how the first solutions are highly oscillatory and, later on, it stabilizes. In fact, these figures demonstrate the behavior of the FP method in converging to the optimal regularization parameter.

The obtained temperature profile with the high dimension model of $n = 21$ points is displayed with the simulated experimental data in Figure 41. This profile is zoomed at the region of $0.03 \leq y \leq 0.09$ m in order to better visualize the behavior in the middle portion of the channel - the peripheral temperature magnitude is much larger than the ones in such range. The obtained temperature profile displayed shows good agreement with the experimental data.

5.5.3 Results for the Inverse Problem 3 (IP-3)

In the radiative transfer problem, the single scattering albedo considered assumes a parabolic profile along the spatial coordinate, with the exact function given by $\omega^*(\tau) = -0.6\tau^2 + 1.0$. The optical thickness is set as $\tau_0 = 1.0$, and the incident external radiation as $A_1 = 1.0$ and $A_2 = 0.0$, at $\tau = 0$ and $\tau = \tau_0$, respectively, i.e., there is no incident radiation at $\tau = \tau_0$. The experimental data are considered to be evenly acquired in the range $0.1 \leq \mu \leq 0.8$, with steps of $\Delta\mu = 0.05$, and noise level of $\sigma_3 = 0.01$ is used in Eq.

Figure 40 – Evolution of the solution obtained for different values of λ as the FP series converges.

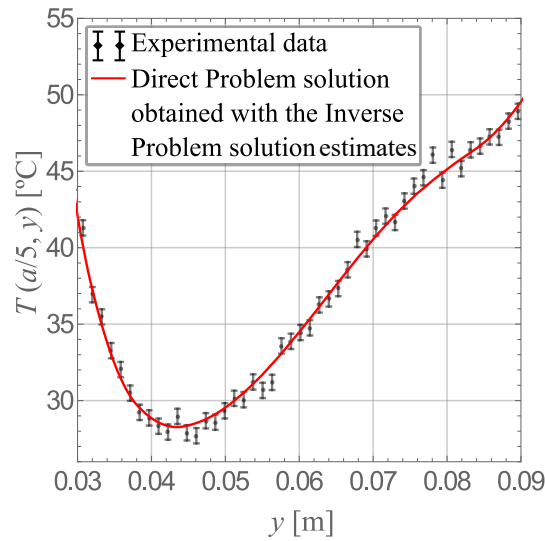


Source: Jardim et al., 2022 (160).

5.10c. For IP-3, we tested only one low dimension model, with $n = 7$ dimensions. Every solution is obtained with 20 DE internal loops, and the search is performed in the range $0 \leq \mathbf{u}_3 \leq 1.0$, which are indeed the physical bounds for the single scattering albedo.

Using an initial parameter of $\phi = 1.0$, divergence was detected on the 7th term of the series, as explained in Section 5.2.1. Therefore, using the steps proposed in Section 5.2.1, the new value of $\sqrt{\phi} = 0.8988$ was obtained. With this new ϕ , the series is considered converged with less than 1% of error on the 5th term. The solution obtained for this low dimension model is displayed in Figure 42a. Then, from this low dimension solution, the estimated initial value of the regularization parameter for the high dimension model with $n = 21$ was $\lambda_{\text{high}} = 0.2677$. The problem is solved again with this initial λ_{high} , and the results obtained are displayed in Figure 42b. For the sake of illustration, the next term of the series calculated by the FP method yielded a regularization parameter of $\lambda_{\text{high}} = 0.2686$, which represents an increase of 0.0009. Therefore, the series can also be considered converged.

Figure 41 – Simulated experimental data and temperature profile obtained with the solution of IP-2 with $n = 21$.



Source: Jardim et al., 2022 (160).

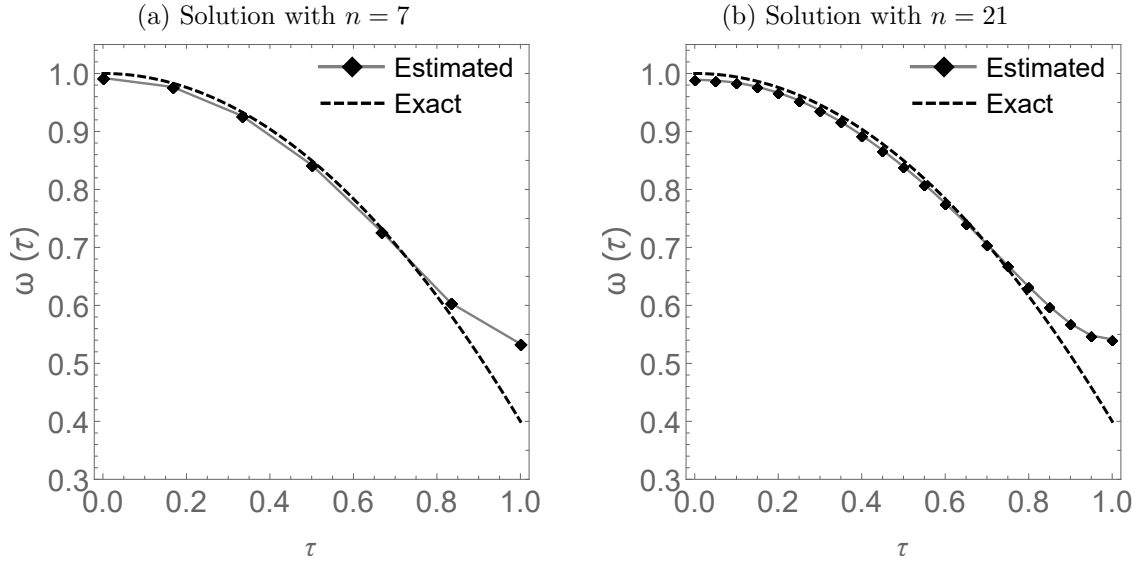
It is possible to see in Figure 42b that the estimate of λ_{high} yielded a good agreement of the estimated values for the single scattering albedo to the exact values. It is important to notice that, due to the lack of sensitivity from $\tau = 0.8$ to $\tau = 1.0$, some information is lost. Although the results displayed in Figure 42 are equally good in approximating the exact value of the scattering albedo, the increased resolution of $n = 21$ points makes the technique attractive for reducing the computational cost of finding the optimal λ .

Figure 44 presents the radiation intensity profile obtained with the solution of the high dimension model IP-3, i.e. $n = 21$ points. The simulated experimental data is also presented with error bars corresponding to the standard deviation of 0.01. Similarly to IP-1 and IP-2, the solution obtained also shows good approximation with the experimental data.

5.6 Conclusions

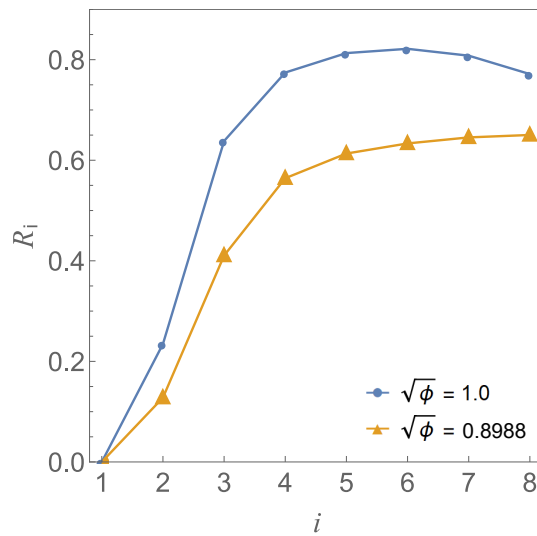
In this chapter a technique aimed at obtaining an estimate for the Tikhonov Regularization parameter is presented. This is achieved by finding the optimal parameter of a problem with reduced number of dimensions, and then equalizing the norm of the regularized solutions. The computational experiments were carried out on the scope of inverse heat transfer problems, which are common subjects in the areas of health,

Figure 42 – Solutions for IP-3: (a) low dimension model with $n = 7$, and (b) the high dimension model with $n = 21$, obtained with the estimated value for λ_{high}



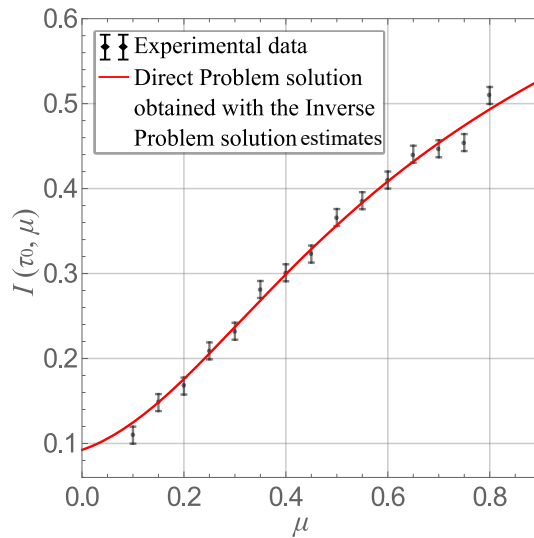
Source: Jardim et al., 2022 (160).

Figure 43 – Evolution of the sequence R_i for the low dimension model with $n = 7$ showing the divergent sequence of $\sqrt{\phi} = 1.0$ (solid dots), and the convergent sequence of the found value $\sqrt{\phi} = 0.8988$ (solid triangles)



Source: Jardim et al., 2022 (160).

Figure 44 – Simulated experimental data and radiation intensity profile obtained with the solution of IP-3 with $n = 21$.



Source: Jardim et al., 2022 (160).

renewable energy and climate research. The results have shown that this technique is robust when the low dimension model has sufficient points to represent the sought function, specially when it has several abrupt changes. Investigation must continue on testing this technique on other inverse problems, and also on the development of a more robust and automatic algorithm, especially regarding 2D function estimation problems. Furthermore, the convergence criterion for the Fixed Point Iteration method is discussed in the light of these problems. The presented results reinforce the robustness of the FP method when the proposed series converges to the optimal regularization parameter. However, when the series does not converge, fixing the hyperparameter ϕ of the method is crucial.

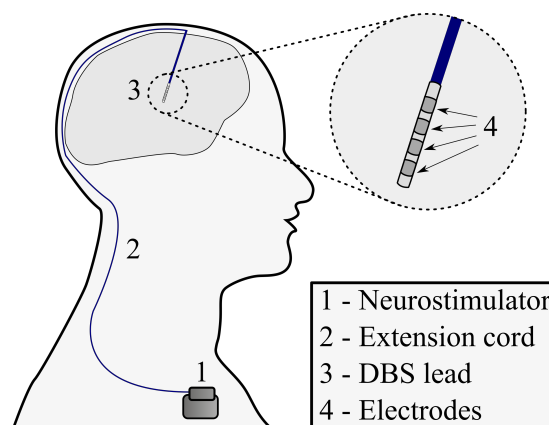
6 BRAIN THERMAL AND ELECTRICAL PROPERTIES ESTIMATION USING EXPERIMENTAL DATA FROM DEEP BRAIN STIMULATION LEAD

6.1 Introduction

The surgery known as Deep Brain Stimulation (DBS) is a neurosurgical procedure where an electrical stimulator is implanted in a specific brain region in order to reduce the symptoms of several tremor diseases. Starting at the end of the decade of 1980, DBS has become highly accepted as treatment for Parkinson's disease (162), dystonia (163), epilepsy (164) and others (165). To this day, new investigations are still discovering and increasing the collection of diseases that is possible to treat with DBS.

Figure 45 shows a simplified representation of the DBS system and its implementation inside the patient's head. An electrical signal with specific frequency is generated by the circuit on the neurostimulator, which is a pacemaker-like device installed subcutaneously near the clavicle of the patient. This signal is delivered to the lead via an extension cord, a subcutaneous wire. The thin, insulated and coiled wires inside the lead carry this signal to the electrodes on its ending. Then, these electrodes deliver the stimulation to the targeted area of the brain (165, 166).

Figure 45 – Representation of the DBS system with detail on the lead inside the brain.



Source: Jardim et al., 2022 (167).

Despite its use being largely spread worldwide and having a well-tolerated surgical procedure (168), little is known about DBS's physiological effects on the brain and, on

top of that, some of the most common injuries are related to possible internal burns from thermal coupling with other equipment, such as magnetic resonance imaging (169). Although less common, there are injuries reported in the literature which are related to internal burn during normal operation (170).

In this context, the present work intends to formulate and solve a bioheat model of the brain with a DBS lead. The Penne's model (138) is coupled with the Laplace equation of electrical field yielding two partial differential equations. This theoretical approach to solve the electrical heating due to DBS's activity was originally introduced in (142). Furthermore, the present work aims to use this solution as a direct problem of an inverse analysis to obtain estimates of thermal and electrical conductivities of the brain. This information can be of great value to avoid injuries due to temperature increase. Results show that positioning a sensor inside the DBS lead can generate useful experimental data for physicians to characterize the patient brain, given that the sensor is accurate enough.

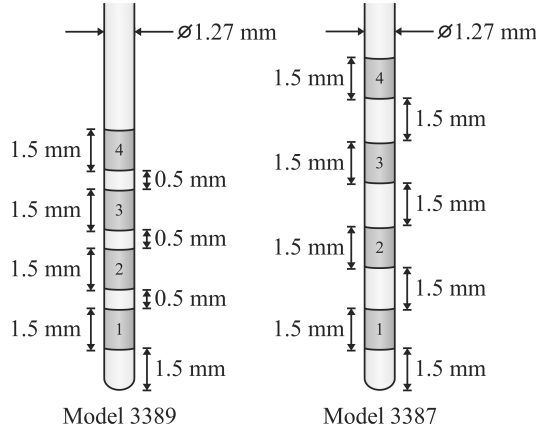
6.2 Formulation and solution of the dbs heating problem

To understand the heating process caused by the electrical stimulation of the brain, two Medtronic® DBS leads are studied: Model 3387 and Model 3389. These are cylindrical leads with 1.27 mm of diameter and, in each one, there are four electrodes with 1.5 mm of length. The main difference between them is the electrodes spacing, with distances of 1.5 mm on the Model 3387 and 0.5 mm on Model 3389, as schematically presented in Figure 46

Considering the axisymmetric plane defined by the length of the lead and the radius of a cylindrical coordinates system, as illustrated in Figure 47. This plane has boundaries ranging from $r = R_1$ to $r = R_2$, where R_1 is the radius of the lead and R_2 a sufficient long distance, and from $z = 0$ to $z = H$, where H is a sufficient long height. Also in Figure 47, the term z^{exp} represents the height where the sensor is located.

To describe how temperature increases on the brain with the electrical stimulator, phenomena such as blood perfusion and metabolic heat generation must be considered. So the model proposed by (138) and (172) is used herein. The Joule heating due to the DBS electrical activity is caused by the current flowing from one electrode to another. It can be added to the bioheat model by terms of the electrical potential $V(r, z)$, which is calculated by the Laplace equation. So the bioheat equation, in axisymmetrical cylindrical

Figure 46 – Schematic representation of Medtronic’s Model 3389 and Model 3387 showing the geometrical configuration of the electrodes.



Source: Adapted from Medtronic Inc., 2002 (171).

coordinates, is given by

$$\frac{1}{r} \frac{\partial}{\partial r} \left(k r \frac{\partial T}{\partial r} \right) + \frac{\partial}{\partial z} \left(k \frac{\partial T}{\partial z} \right) - \rho_b \omega_b c_b (T - T_b) + Q_m + \sigma |\Delta V|^2 = \rho c_p \frac{\partial T}{\partial t} \quad (6.1)$$

$$\left. \frac{\partial T}{\partial r} \right|_{r=R_1} = 0 \quad (6.2)$$

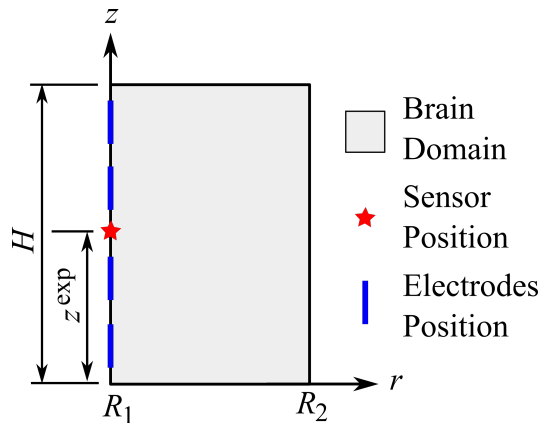
$$T(r, z, t) = T_a \text{ at } r = R_2, z = 0, z = H \quad (6.3)$$

where, for the brain tissue, k is the thermal conductivity, ρ is the specific mass, c_p is the specific heat, σ is the electrical conductivity and Q_m the metabolic heat generation. The temperature T_a is the initial brain temperature when there is no electrical heating. The parameters related to the blood perfusion are ω_b , ρ_b , c_b and T_b , which are the blood perfusion parameter, the specific mass, the specific heat and the temperature, respectively, for the blood in the brain. As previously mentioned, $V(r, z)$ is the electrical potential, which can be directly calculated by the Laplace equation in cylindrical coordinates, given by

$$\frac{1}{r} \frac{\partial}{\partial r} \left(\sigma r \frac{\partial V}{\partial r} \right) + \sigma \frac{\partial^2 V}{\partial z^2} = 0 \quad (6.4)$$

$$\left. \frac{\partial v}{\partial \mathbf{n}} \right|_{r=R_2, z=0, z=h} = 0 \quad (6.5)$$

Figure 47 – Schematic representation of the computational axisymmetric domain.



Source: Jardim et al., 2022 (167).

$$V(R_1, z) = f(z) \quad (6.6)$$

The problem given by Eq. 6.1 to Eq. 6.6 is solved with the built-in routine *NDSolve* of the Wolfram Mathematica 10.0 system (173), which is used here with an automatic absolute and relative error control. The chosen method of solution is the Finite Elements Method (FEM) as a sub-routine of *NDSolve*.

6.3 Inverse problem formulation and solution

Acquiring experimental temperature data inside the brain can be challenging and complicated in terms of technology and two main difficulties can be encountered when dealing with the DBS heating process: the small size of the lead and the also small variation of temperature due to normal DBS operation. This work proposes the use of a sensor inside the lead positioned at halfway distance between electrodes 2 and 3, therefore, the objective of this work is to evaluate if is possible estimate the parameters accurately assuming that the sensor is in the position shown in Figure 47.

Since experimental data are not available, they are simulated by adding random noise to the solution of the direct problem given by Eq. 6.1 to Eq. 6.6. These errors are drawn from a normal distribution centered in zero and are calculated with the expression

$$T_i^{\text{exp}} = T(R_1, z^{\text{exp}}, t_i^{\text{exp}}) + e_i, \text{ with } e_i \sim N(0, \epsilon^2), i = 1, 2, \dots, N_d \quad (6.7)$$

where N_d is the total number of experimental data, z^{exp} is the height corresponding to the position of the temperature sensor, \mathbf{t}^{exp} is the vector containing time instants when such data is acquired and ϵ is the standard deviation of the experimental data. The reader should note that the exact temperature is calculated at $r = R_1$ and $z = z^{\text{exp}} = H/2$, i.e., as already mentioned, at the lead-brain interface and in the middle of the four electrodes.

The thermal and electrical conductivity, k and σ respectively, are here considered unknowns and, not only that, their prior information can be modeled as a normal distribution in order to obtain the inverse problem formulation as a Maximum a Posteriori (MAP) objective function. This approach allows us to obtain single point estimates for the unknowns and approximations for the confidence intervals (28). So, the MAP objective function can be written as

$$Q(\mathbf{Z}) = [\mathbf{T}^{\text{exp}} - \mathbf{T}^{\text{calc}}(\mathbf{Z})]^T \mathbf{W}^{-1} [\mathbf{T}^{\text{exp}} - \mathbf{T}^{\text{calc}}(\mathbf{Z})] + (\mu_{\text{pr}} - \mathbf{Z})^T \mathbf{V}^{-1} (\mu_{\text{pr}} - \mathbf{Z}) \quad (6.8)$$

where \mathbf{Z} is the vector of unknown estimatives, \mathbf{T}^{exp} the vector containing the experimental data, \mathbf{T}^{calc} is the calculated temperatures with \mathbf{Z} , \mathbf{W} is the covariance matrix, \mathbf{V} is the priori covariance matrix and μ_{pr} is the mean of the prior information. To minimize this objective function, the Gauss-Newton iterative procedure is applied and it can be formulated as (153)

$$\mathbf{Z}^{n+1} = \mathbf{Z}^n + [(\mathbf{J}^T)^n \mathbf{W}^{-1} \mathbf{J} + \mathbf{V}^{-1}]^{-1} \times [(\mathbf{J}^T)^n \mathbf{W}^{-1} [\mathbf{T}^{\text{exp}} - \mathbf{T}^{\text{calc}}(\mathbf{Z})] + \mathbf{V}^{-1} (\mu_{\text{pr}} - \mathbf{Z})] \quad (6.9)$$

where \mathbf{J} is the Jacobian matrix, which have its elements defined by

$$J_{ij} = \frac{\partial T_i^{\text{calc}}}{\partial Z_j}, \quad i = 1, 2, \dots, N_d \text{ and } j = 1, 2, \dots, N_u \quad (6.10)$$

with N_u being the number of unknowns and N_d was already defined as the total number of experimental data.

To obtain approximations of the standard deviation of the posterior distribution for each parameter, one can use the following expression

$$\sigma_{z_i} = \sqrt{\left[(\mathbf{J}^T \mathbf{W}^{-1} \mathbf{J} + \mathbf{V}^{-1})^{-1} \right]_{i,i}} \quad (6.11)$$

The expression given by Eq. 6.11 is an approximation when dealing with non-linear inverse problems. Even with the prior information and the experimental noise modeled as a normal distribution, it is not possible to guarantee that the posterior distribution is, in fact, also modeled by a normal distribution (174).

6.4 Results and discussion

6.4.1 Direct problem solution and results

In order to obtain the solution of the direct problem given by Eq. 6.1 to Eq. 6.6, several parameters related to the physiology of the brain must be known. The exact values of these parameters can be readily found in the literature and, in this work, the ones from (142) are used. Table 27 summarizes all the values used for the solution of the direct problem and, later on, this solution is used to generate the experimental data.

The boundary condition proposed in Eq. 6.6 must be set as a step function where the DBS electrical potential is applied only at the position of active electrodes. In this work, the V_{rms} of the DBS high setting operation mode is used due to its higher capacity of generating heat. This setting generates an electrical signal of 10 V, 185 pps and 210 ms yielding a V_{rms} of 1.561 V (142).

The solution obtained with these parameters is displayed in Figure 48, where Figure 48a represents the temperature distribution and Figure 48b the electrical potential distribution. These results are obtained in $t = 1000$ s, which, from our results, can be reasonably considered as steady state. The pair of active electrodes selected are 1 and 4 – see Figure 46 – and the DBS lead type is the Model 3389.

In Figure 48a, it is possible to see the magnitude of the temperature increase, which is approximately 0.65 °C, for that configuration. This result shows that, in order to identify this temperature variation, the sensor placed inside the DBS lead and in the middle of the electrodes must have a precision of 0.05 °C, which is considerably small for today’s technology but somewhat achievable with a thermistor.

The Finite Elements mesh is composed by 2786 triangular elements, generated with the option “*MaxCellMeasure*” included in the *NDSolve* routine. The same mesh is used

Table 27 – Exact values of the parameters of the direct problem.

Parameter	Value	Dimension	Observation
T_b	36.7	[°C]	Blood temperature
σ	0.35	[S/m]	Electrical conductivity
k	0.527	[W/m.K]	Thermal conductivity
H	50.0	[mm]	Height of the domain
R_1	0.635	[mm]	First radius of the domain
R_2	20.0	[mm]	Second radius of the domain
Q_m	9132.0	[W/m ³]	Internal metabolic heat generation
c_p	3650	[J/kgK]	Specific heat of the brain tissue
ρ	1040	[kg/m ³]	Specific mass of the brain
ω_b	0.008	[ml/s.cm ³]	Blood perfusion
ρ_b	1057	[kg/m ³]	Specific mass of the blood
c_b	3600	[J/kg.K]	Specific heat of the blood

Source: Jardim et al., 2022 (167).

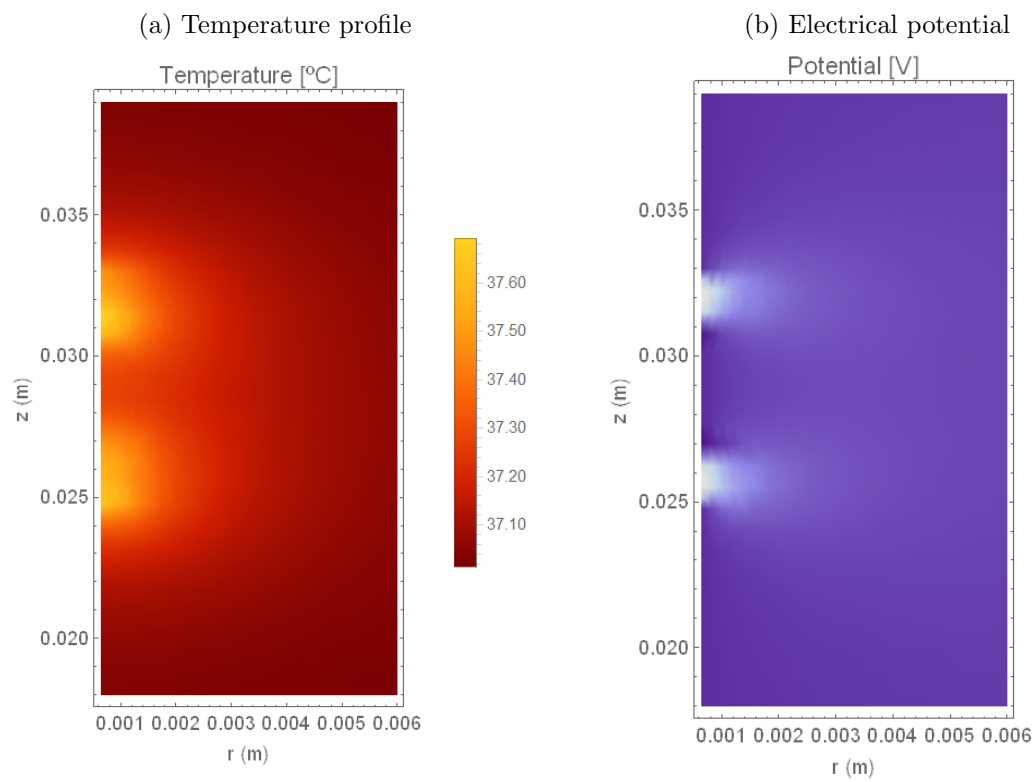
for both the electrical and the temperature problem. This approach can benefit from the use of different mesh for each problem, as it is possible to see that the electrical problem got some unwanted oscillations in its solution.

6.4.2 Inverse problem solution and results

To acquire experimental data, the vector containing the instants of time \mathbf{t}^{exp} range from 1 s to 61 s with fixed intervals of $\Delta t = 1$ s, which generates $N_d = 61$ experimental data. Using $\epsilon = 0.05$ °C and $\epsilon = 0.025$ °C in Eq. 6.7, the experimental noise can be added in order to simulate real data. This level of error is relatively low when dealing with temperature information, but considering the maximum amplitude variation of temperature obtained in the problem, this is a fundamental condition to obtain a solution within a reasonable confidence region. Figure 49 shows the exact solution with their respective experimental data obtained for both noise levels. Observe how the experimental data spread along on the plot range of 0.4 °C. In this context, noise level of $\epsilon = 0.05$ °C generates more realistic measurements of temperature.

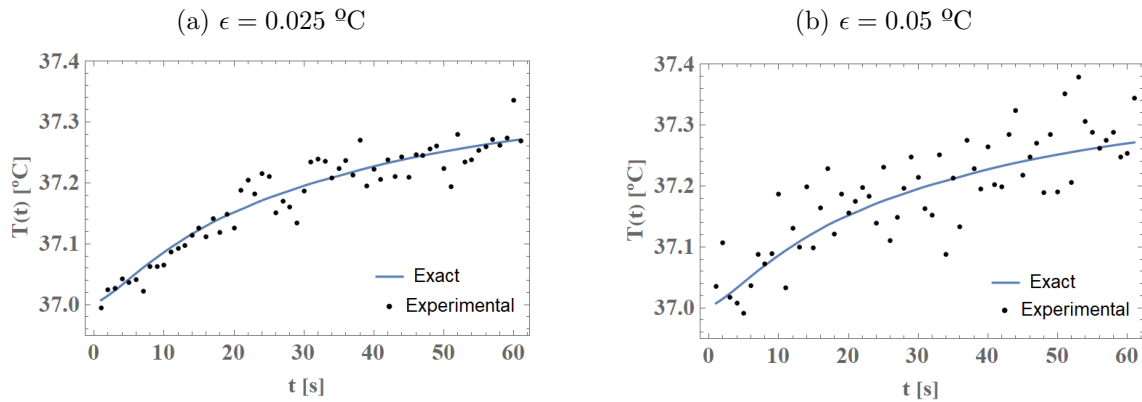
To solve the inverse problem using the MAP approach, a prior information of the unknown parameters must be set. In this work it is used arbitrary information for both the thermal and electrical conductivities. Their mean values are both set as 0.5 W/m.K and 0.5 S/m, respectively, and their standard deviation as 0.25 W/m.K and 0.25 S/m,

Figure 48 – Solution of both the temperature and the electrical problem for Model 3389 with activity on electrodes 1 and 4.



Source: Jardim et al., 2022 (167).

Figure 49 – Experimental data along with exact solution for Model 3389 with activity on electrodes 1 and 4 for two noise levels: $\epsilon = 0.025$ °C and $\epsilon = 0.05$ °C in Eq. 6.7, respectively.



Source: Jardim et al., 2022 (167).

which represents a considerable large interval centered in an expected value.

For the iterative method described in Eq. 6.9, the approach used is to fix the number of iterations in five steps. The main goal is to have a solution influenced mainly by the MAP formulation and to have a somewhat predictable computational time. The derivative in Eq. 6.10 is obtained with a centered finite difference formula using an interval of 1% for each parameter exact value.

The results displayed on Table 28 and Table 29 are the ones obtained for DBS lead Model 3389 with the pairs of electrodes 1-2 and 1-4 actives, respectively. Table 30 and Table 31 presents the results for the Model 3387, with the same pairs of electrodes mentioned. These two pairs of electrodes are the only ones tested: 1-2 and 1-4. Since the sensor is positioned in the middle of the four electrodes, it is expected that pairs 2-3 will render the best results due to increased temperature reading, therefore we omitted the results for this pair.

Six independent experiments were performed for each configuration of lead type, pairs of electrode actives and noise level, meaning that the experimental data are different for each one. Since the optimization method used is deterministic and the starting point is the same for every scenario, there is no need to perform multiple executions with the same experimental data.

The terms k^* and σ^* on Table 28 to Table 31 represent the mean value obtained for the thermal and electrical conductivity, respectively. The standard deviation is presented

below of each parameter estimation inside parentheses. As explained in Section 6.3, this posterior normal distribution is a linear approximation, so this standard deviation displayed correspond to this approximation deviation.

Firstly, the reader must notice how much more accurate are the estimatives for the electrical conductivity σ in comparison to the thermal conductivity k . This indicates a higher sensitivity of the electrical problem, meaning that changes in σ are more noticeable on the temperature profile resultant than changes in k . In every configuration, the averages for the standard deviations of the electrical conductivity is smaller than its thermal conductivity counterpart.

Although the thermal conductivity generated small intervals with the most sensible set up (Model 3389, electrodes 1 and 2 and noise levels of $\epsilon = 0.25$ °C), the mean value of of $k = 0.4022$ W/m.K estimated in Experiment 2 W/m K is considerably far from its exact value of $k = 0.5270$ W/m.K. In spite of that poor result, the averages for the mean values of the six experiments presented in Table 28 are acceptable when compared to the exact value, indicating that these average standard deviations are somewhat expectable.

The results for lead type Model 3387, in Table 30 and (Table 31), are supposed to have less precise intervals since the temperature variation is smaller than the ones from Model 3389 and, indeed, they do for the parameter k . When comparing the average standard deviations this becomes clear: thermal conductivity estimatives enlarges its standard deviation more than electrical conductivity when going from Model 3389 to Model 3387. The reader can grasp this observation by comparing results from Table 28 with Table 30) and Table 29 with Table 31.

Table 28 – Results obtained using DBS lead Model 3389 with electrode pair 1-2 active and experimental noise levels of $\epsilon = 0.025$ °C and $\epsilon = 0.050$ °C

Model 3389 - Electrodes 1 and 2				
ϵ	0.025 °C		0.050 °C	
u_i	k^* (Std. Dev.)	σ^* (Std. Dev.)	k^* (Std. Dev.)	σ^* (Std. Dev.)
Exp. #1	0.4477 (0.0722)	0.3135 (0.0378)	0.5970 (0.1449)	0.3925 (0.0729)
Exp. #2	0.4022 (0.0675)	0.2873 (0.0356)	0.6164 (0.1523)	0.3950 (0.0745)
Exp. #3	0.5440 (0.0998)	0.3547 (0.0495)	0.4915 (0.1347)	0.3276 (0.0676)
Exp. #4	0.5281 (0.0572)	0.3513 (0.0274)	0.4480 (0.1037)	0.3135 (0.0501)
Exp. #5	0.5862 (0.0681)	0.3746 (0.0314)	0.4516 (0.0214)	0.3132 (0.0081)
Exp. #6	0.5957 (0.0724)	0.3820 (0.0333)	0.5918 (0.1275)	0.3725 (0.0577)
Avg.	0.5222 (0.0728)	0.3439 (0.0358)	0.5327 (0.1140)	0.3523 (0.0551)
Dim.	[W/m.K]	[S/m]	[W/m.K]	[S/m]

Source: Jardim et al., 2022 (167).

Table 29 – Results obtained using DBS lead Model 3389 with electrode pair 1-4 active and experimental noise levels of $\epsilon = 0.025$ °C and $\epsilon = 0.050$ °C.

Model 3389 - Electrodes 1 and 4				
ϵ	0.025 °C		0.050 °C	
u_i	k^*	σ^*	k^*	σ^*
	(Std. Dev.)	(Std. Dev.)	(Std. Dev.)	(Std. Dev.)
Exp. #1	0.4951 (0.0715)	0.3402 (0.0205)	0.5585 (0.1310)	0.3727 (0.0388)
Exp. #2	0.5858 (0.0509)	0.3799 (0.0253)	0.5469 (0.1270)	0.3634 (0.0387)
Exp. #3	0.5806 (0.0824)	0.3631 (0.0235)	0.4385 (0.1192)	0.3183 (0.0338)
Exp. #4	0.5212 (0.0688)	0.3581 (0.0174)	0.4457 (0.1133)	0.3247 (0.0269)
Exp. #5	0.4815 (0.0533)	0.3467 (0.0292)	0.5730 (0.1223)	0.3547 (0.0322)
Exp. #6	0.4710 (0.0644)	0.3342 (0.0154)	0.4598 (0.0661)	0.3123 (0.0191)
Avg.	0.5225 (0.0652)	0.3537 (0.0218)	0.5037 (0.1131)	0.3410 (0.0324)
Dim.	[W/m.K]	[S/m]	[W/m.K]	[S/m]

Source: Jardim et al., 2022 (167).

Table 30 – Results obtained using DBS lead Model 3387 with electrode pair 1-2 active and experimental noise levels of $\epsilon = 0.025$ °C and $\epsilon = 0.050$ °C.

Model 3387 - Electrodes 1 and 2				
ϵ	0.025 °C		0.050 °C	
u_i	k^* (Std. Dev.)	σ^* (Std. Dev.)	k^* (Std. Dev.)	σ^* (Std. Dev.)
Exp. #1	0.6568 (0.1189)	0.4001 (0.0489)	0.6377 (0.1774)	0.3980 (0.0742)
Exp. #2	0.5726 (0.1075)	0.3747 (0.0466)	0.3670 (0.1396)	0.2765 (0.0654)
Exp. #3	0.5854 (0.1108)	0.3726 (0.0468)	0.5848 (0.1778)	0.3547 (0.0713)
Exp. #4	0.4545 (0.0475)	0.3181 (0.0239)	0.6834 (0.1579)	0.3996 (0.0755)
Exp. #5	0.4477 (0.0994)	0.3163 (0.0454)	0.5294 (0.0394)	0.3574 (0.0183)
Exp. #6	0.5644 (0.1169)	0.3685 (0.0502)	0.5142 (0.0541)	0.3491 (0.0264)
Avg.	0.5249 (0.1001)	0.3583 (0.1169)	0.5527 (0.1243)	0.3558 (0.0551)
Dim.	[W/m.K]	[S/m]	[W/m.K]	[S/m]

Source: Jardim et al., 2022 (167).

Table 31 – Results obtained using DBS lead Model 3387 with electrode pair 1-4 active and experimental noise levels of $\epsilon = 0.025$ °C and $\epsilon = 0.050$ °C.

Model 3387 - Electrodes 1 and 4				
ϵ	0.025 °C		0.050 °C	
u_i	k^* (Std. Dev.)	σ^* (Std. Dev.)	k^* (Std. Dev.)	σ^* (Std. Dev.)
Exp. #1	0.4347 (0.1601)	0.3369 (0.0158)	0.6140 (0.2152)	0.3448 (0.0361)
Exp. #2	0.4338 (0.1501)	0.3710 (0.0128)	0.4686 (0.1576)	0.3729 (0.0291)
Exp. #3	0.5184 (0.1528)	0.3622 (0.0189)	0.4276 (0.1279)	0.4041 (0.0386)
Exp. #4	0.4556 (0.1434)	0.3714 (0.0176)	0.6050 (0.2161)	0.3599 (0.0376)
Exp. #5	0.4140 (0.1303)	0.3587 (0.0146)	0.2931 (0.1935)	0.3191 (0.0321)
Exp. #6	0.7910 (0.1874)	0.3686 (0.0279)	0.6119 (0.2175)	0.3550 (0.0378)
Avg.	0.5079 (0.1540)	0.3614 (0.0179)	0.5033 (0.1879)	0.3593 (0.0352)
Dim.	[W/m.K]	[S/m]	[W/m.K]	[S/m]

Source: Jardim et al., 2022 (167).

6.5 Conclusions

The DBS electrical activity inside the brain causes a temperature increase by Joule effect. In this work, this heating process was modeled as an axis-symmetrical problem in order to obtain the temperature distribution around the brain with active electrodes. This model is then used to formulate a practical inverse problem where, with one temperature sensor inside the DBS's lead, experimental temperature data are acquired and used to estimate the thermal and electrical conductivities of the brain tissue. This inverse problem was formulated and solved using the Maximum a Posteriori method, which resulted in approximation for the posteriori distribution. This approach showed that it is possible to estimate those parameters simultaneously with only one sensor inside the lead, but the accuracy of this sensor must be considerably high and its positioning inside the lead must be as close to active electrodes as possible.

FINAL CONSIDERATIONS

This thesis presented a collection of five case studies where Computational Intelligence methods are used to solve inverse heat transfer problems. The contributions of such studies can be briefly classified into two main categories: (i) testing and development of efficient computational procedures, and (ii) development and enhancement of heat transfer scientific and engineering applications. In the first group are the investigations presented in Chapters 3, 4 and 5, and in the second group the works of Chapters 2 and 6. Namely, this classification can be detailed as follows:

Contributions to efficient computational procedures. The common factor in this group is the fact that the focus of the studies is on improving the Computational Intelligence techniques presented, such as local and global optimization methods, regularization schemes, and others. To do this, the formulation and solution of different inverse problems were the testbed of such methods. Chapter by chapter, the contributions of this group are:

- Chapter 3: The damping factor of the Levenberg-Marquardt method is updated using a recently proposed Fuzzy Logic approach. To test this technique, a coupled conduction-radiation inverse problem was proposed. This study showcased the first time that Tikhonov Regularization was used with this Fuzzy Logic updating scheme. The results were competitive against the classical Levenberg-Marquardt, but more investigations to assess its performance must be performed.
- Chapter 4: The Topographical Global Optimization method is tested with two different initialization and two different local search methods, resulting in four combinations. Three inverse heat transfer problems were tested and they pointed out advantages and disadvantages of each one via the Wilcoxon Signed Ranks test.
- Chapter 5: A technique to estimate the optimal Tikhonov Regularization parameter is developed, where a version with low dimension of the original problem is solved. The results obtained show the feasibility of the technique in reducing the computational cost of obtaining the optimal regularization parameter with an automatic method, such as the Fixed Point Iteration used. Further investigations should test this approach with 2D and 3D inverse problems.

Contributions to heat transfer scientific and engineering applications. In this group, the main focus was to enhance or develop heat transfer inverse problems with the application in mind. In other words, the objective was not the method itself, but the final purpose of the inverse problem. With that said, two chapters were presented dealing with different problems, they are:

- Chapter 2: An Artificial Neural Network with Autoencoders was modeled as an inverse heat transfer problem in order to access the bonding quality between two materials. With this approach, a fast estimation procedure were developed, where temperature experimental data of the exposed medium surface serves as input to the neural network, which outputs the thermalphysical properties of the bonding layer.
- Chapter 6: The temperature increase of a Deep Brain Stimulation lead was study and a inverse problem was formulated and solved considering a temperature sensor inside the lead. With this approach, physicians may have access to information about the lead functioning and even brain tissue parameters estimation. Further investigations may deal with more complex DBS directional leads.

Finally, it is worth mentioning here that the application of Computational Intelligence techniques in inverse problems are a enormous field of Applied Computational Mathematics and Engineering. In fact, this thesis intended to showcase an organized - and relatively small - collection of the four main Computational Intelligence Concepts: Neural Networks, Metaheuristics, Probabilistic Models and Fuzzy Logic. In addition to all the advances and results obtained for each one of the works presented, this thesis is also an unpretentious way of celebrating over 60 years of research and application of Computational Intelligence in science and engineering.

CONSIDERAÇÕES FINAIS

Esta tese apresentou uma coleção de cinco estudos de caso onde métodos de Inteligência Computacional são usados para resolver problemas inversos de transferência de calor. As contribuições de tais estudos podem ser resumidamente classificadas em duas categorias principais: (i) teste e desenvolvimento de rotinas computacionais eficientes, e (ii) desenvolvimento e aprimoramento de aplicações científicas e de engenharia de transferência de calor. No primeiro grupo estão as investigações apresentadas nos Capítulos 3, 4 e 5, já no segundo grupo, os trabalhos dos capítulos 2 e 6. Especificamente, esta classificação pode ser detalhada da seguinte forma:

Contribuições para procedimentos computacionais eficientes. O fator comum neste grupo é o fato de que o foco dos estudos está no aprimoramento das técnicas de Inteligência Computacional apresentadas, como métodos de otimização local e global, esquemas de regularização, entre outros. Para isso, a formulação e solução de diferentes problemas inversos serviram de teste para tais métodos. Capítulo por capítulo, as contribuições deste grupo são as seguintes:

- Capítulo 3: O fator de amortecimento do método Levenberg-Marquardt é atualizado através de uma abordagem com Lógica Fuzzy recentemente proposta. Para testar esta técnica, um problema inverso de transferência de calor por condução e radiação simultaneamente foi proposto. Este estudo mostrou a primeira vez que a Regularização de Tikhonov foi utilizada com este esquema de atualização com Lógica Fuzzy. Os resultados foram competitivos com o clássico Levenberg-Marquardt, porém mais investigações para avaliar seu desempenho devem ser realizadas.
- Capítulo 4: A técnica conhecida como Otimização Global Topográfica é testada com dois métodos de inicialização diferentes e dois métodos de busca local diferentes, resultando em quatro combinações distintas. Três problemas inversos de transferência de calor foram testados e apontaram as vantagens e desvantagens de cada um por meio do teste estatístico de Wilcoxon.
- Capítulo 5: Uma técnica para estimar o parâmetro ótimo da Regularização de Tikhonov é desenvolvida, onde uma versão com uma dimensão menor do problema

original é resolvida. Os resultados obtidos mostram a viabilidade da técnica em reduzir o custo computacional de obtenção do parâmetro com um método automático, como a Iteração de Ponto Fixo. Investigações futuras devem testar essa abordagem com problemas inversos de duas ou três dimensões.

Contribuições para aplicações científicas e de engenharia em transferência de calor. Neste grupo, o foco principal foi aprimorar ou desenvolver problemas inversos de transferência de calor com a aplicação em mente. Em outras palavras, o objetivo não era o método em si, mas o propósito final do problema inverso. Dito isso, foram apresentados dois capítulos que trataram de problemas diferentes, são eles:

- Capítulo 2: Uma Rede Neural Artificial com Autoencoders foi modelada como um problema inverso de transferência de calor para caracterizar a qualidade de junção entre dois materiais. Com esta abordagem, um procedimento de estimativa computacionalmente rápido foi desenvolvido, onde os dados experimentais de temperatura da superfície do meio exposto servem como entrada para a rede neural, que por sua vez retorna as propriedades termofísicas da camada de ligação.
- Capítulo 6: Estudou-se o aumento de temperatura no cérebro causado por um eletrodo de Estimulação Cerebral Profunda e um problema inverso considerando um sensor de temperatura no interior do eletrodo foi formulado e resolvido. Com essa abordagem, os médicos podem ter acesso à informações sobre o funcionamento do eletrodo e até mesmo a estimativa de parâmetros do tecido cerebral. Outras investigações podem lidar com esquemas de eletrodos de DBS mais complexos, como os direcionais, por exemplo.

Por fim, vale ressaltar aqui que a aplicação de técnicas de Inteligência Computacional em problemas inversos é um enorme campo da Engenharia e Matemática Computacional Aplicada. De fato, esta tese pretende apresentar uma coleção organizada - e relativamente pequena - dos quatro principais Conceitos de Inteligência Computacional: Redes Neurais, Metaheurísticas, Modelos Probabilísticos e Lógica Fuzzy. Além de todos os avanços e resultados obtidos em cada um dos trabalhos apresentados, esta tese é também uma forma despretensiosa de celebrar mais de 60 anos de pesquisa e aplicação da Inteligência Computacional em ciência e engenharia.

CONSIDERACIONES FINALES

Esta tesis presentó una colección de cinco estudios de casos en los que se utilizan métodos de Inteligencia Computacional para resolver problemas inversos de transferencia de calor. Las contribuciones de tales estudios se pueden resumir en dos categorías principales: (i) prueba y desarrollo de rutinas computacionales eficientes, y (ii) desarrollo y mejora de aplicaciones científicas y de ingeniería de transferencia de calor. En el primer grupo se encuentran las investigaciones presentadas en los Capítulos 3, 4 y 5, mientras que en el segundo grupo, los trabajos de los Capítulos 2 y 6. En concreto, esta clasificación se puede detallar de la siguiente manera:

Contribuciones a rutinas computacionales eficientes. El factor común en este grupo es que el foco de los estudios está en la mejora de las técnicas de Inteligencia Computacional presentadas, tales como métodos de optimización local y global, esquemas de regularización, entre otros. Para ello, la formulación y solución de diferentes problemas inversos sirvió como prueba para tales métodos. Capítulo por capítulo, las contribuciones de este grupo son las siguientes:

- Capítulo 3: El factor de amortiguamiento del método Levenberg-Marquardt se actualiza utilizando lógica difusa recientemente propuesto. Para probar esta técnica, se propuso un problema inverso de transferencia simultánea de calor por conducción y radiación. Este estudio mostró la primera vez que se utilizó la Regularización de Tikhonov con este esquema de actualización de Fuzzy Logic. Los resultados fueron competitivos con el clásico Levenberg-Marquardt, pero se deben realizar más investigaciones para evaluar su desempeño.
- Capítulo 4: La técnica conocida como Optimización Topográfica Global se prueba con dos métodos de inicialización diferentes y dos métodos de búsqueda local diferentes, lo que da como resultado cuatro combinaciones diferentes. Se probaron tres problemas inversos de transferencia de calor y se señalaron las ventajas y desventajas de cada uno mediante la prueba estadística de Wilcoxon.
- Capítulo 5: Se desarrolla una técnica para estimar el parámetro óptimo de la Regularización de Tikhonov, donde se resuelve una versión con más baja dimensión

del problema original. Los resultados obtenidos muestran la viabilidad de la técnica en la reducción del costo computacional de la obtención del parámetro con un método automático, como es la Iteración de Punto Fijo. Las investigaciones futuras deberían probar este enfoque con problemas inversos de dos o tres dimensiones.

Contribuciones a aplicaciones científicas y de ingeniería en transferencia de calor. En este grupo, el enfoque principal fue mejorar o desarrollar problemas de transferencia de calor inversa con la aplicación en mente. En otras palabras, el objetivo no era el método en sí mismo, sino el propósito último del problema inverso. Dicho esto, se presentaron dos capítulos que trataron diferentes problemas, ellos son:

- Capítulo 2: Se modeló una red neuronal artificial con codificadores automáticos como un problema de transferencia de calor inversa para caracterizar la calidad de la unión entre dos materiales. Con este enfoque, se desarrolló un procedimiento de estimación computacionalmente rápido, donde los datos experimentales de temperatura de la superficie del medio expuesto sirven como entrada a la red neuronal, que a su vez devuelve las propiedades termofísicas de la capa de unión.
- Capítulo 6: Se estudió el aumento de temperatura en el cerebro causado por un electrodo de Estimulación Cerebral Profunda y se formuló y resolvió un problema inverso considerando un sensor de temperatura dentro del electrodo. Con este enfoque, los médicos pueden acceder a información sobre el funcionamiento de los electrodos e incluso a la estimación de los parámetros del tejido cerebral. Otras investigaciones pueden tratar con esquemas de electrodos DBS más complejos, como los direccionales, por ejemplo.

Finalmente, vale la pena mencionar aquí que la aplicación de técnicas de Inteligencia Computacional en problemas inversos es un campo enorme de Ingeniería y Matemática Computacional Aplicada. De hecho, esta tesis pretende presentar una colección organizada -y relativamente pequeña- de los cuatro Conceptos principales de la Inteligencia Computacional: Redes Neuronales, Metaheurísticas, Modelos Probabilísticos y Lógica Difusa. Además de todos los avances y resultados obtenidos en cada uno de los trabajos presentados, esta tesis es también una manera sin pretensiones de celebrar más de 60 años de investigación y aplicación de la Inteligencia Computacional en la ciencia y la ingeniería.

REFERENCES

1. Wichmann B, Wade D. Islamic Design: A mathematical approach. Springer; 2017.
2. Jardim LCS, Knupp DC, Sacco WF, Silva Neto AJ. Solution of a Coupled Conduction–Radiation Inverse Heat Transfer Problem with the Topographical Global Optimization Method. In: Computational Intelligence in Emerging Technologies for Engineering Applications. Springer; 2020. p. 53-71.
3. Silva Neto AJ, Özışık MN. An inverse problem of estimating thermal conductivity, optical thickness, and single scattering albedo of a semi-transparent medium. In: Proceedings of the 1st Inverse Problems in Engineering Conference: Theory and Practice, Florida, USA; 1993. p. 267-73.
4. Knupp DC, Naveira-Cotta CP, Ayres JV, Cotta RM, Orlande HR. Theoretical–experimental analysis of heat transfer in nonhomogeneous solids via improved lumped formulation, integral transforms and infrared thermography. International Journal of Thermal Sciences. 2012;62:71-84.
5. Neto FDM, Silva Neto AJ. An introduction to inverse problems with applications. Springer Science & Business Media; 2013.
6. Özışık MN, Orlande HRB. Inverse Heat Transfer: Fundamentals and Applications. New York, NY: Taylor & Francis; 2000.
7. Özışık MN, Orlande HR, Colaço MJ, Cotta RM. Finite difference methods in heat transfer. CRC press; 2017.
8. Ern A, Guermond JL. Theory and practice of finite elements. vol. 159. Springer; 2004.
9. Zienkiewicz OC, Taylor RL, Zhu JZ. The finite element method: its basis and fundamentals. Elsevier; 2005.
10. Cotta RM. Integral transforms in computational heat and fluid flow. CRC Press; 1993.
11. Zadeh LA. Soft computing and fuzzy logic. In: Fuzzy Sets, Fuzzy Logic, and Fuzzy Systems: Selected Papers by Lotfi a Zadeh. World Scientific; 1994. p. 796-804.
12. Verdegay JL, Yager RR, Bonissone PP. On heuristics as a fundamental constituent of soft computing. Fuzzy sets and systems. 2008;159(7):846-55.

13. Li X, Ruan D, van der Wal AJ. Discussion on soft computing at FLINS'96. *International Journal of Intelligent Systems*. 1998;13(2-3):287-300.
14. Bergman TL, Incropera FP, Dewitt DP, Lavine AS. *Fundamentals of heat and mass transfer*. John Wiley & Sons; 2011.
15. Engl HW, Hanke M, Neubauer A. *Regularization of inverse problems*. vol. 375. Springer Science & Business Media; 1996.
16. Knupp DC, Abreu LA. Explicit boundary heat flux reconstruction employing temperature measurements regularized via truncated eigenfunction expansions. *International Communications in Heat and Mass Transfer*. 2016;78:241-52.
17. Haykin SS. *Neural networks and learning machines*. 3rd ed. Upper Saddle River, NJ: Pearson Education; 2009.
18. Abiodun OI, Jantan A, Omolara AE, Dada KV, Mohamed NA, Arshad H. State-of-the-art in artificial neural network applications: A survey. *Heliyon*. 2018;4(11):e00938.
19. Dave VS, Dutta K. Neural network based models for software effort estimation: a review. *Artificial Intelligence Review*. 2014;42(2):295-307.
20. Zadeh L. Fuzzy Sets. *Information and Control*. 1965;(8).
21. Li Y, Wang G, Chen H, Zhu Z, Zhang D. A decentralized fuzzy inference method for the inverse geometry heat conduction problem. *Applied Thermal Engineering*. 2016;106:109-16.
22. Osman IH, Laporte G. Metaheuristics: A bibliography. *Annals of Operations Research*. 1996;63:513-623.
23. Boussaïd I, Lepagnot J, Siarry P. A survey on optimization metaheuristics. *Information sciences*. 2013;237:82-117.
24. Storn R, Price K. Differential evolution—a simple and efficient heuristic for global optimization over continuous spaces. *Journal of global optimization*. 1997;11(4):341-59.
25. Kennedy J, Eberhart R. Particle swarm optimization. In: *Proceedings of ICNN'95-international conference on neural networks*. vol. 4. IEEE; 1995. p. 1942-8.
26. Kirkpatrick S, Gelatt CD, Vecchi MP. Optimization by simulated annealing. *science*. 1983;220(4598):671-80.

27. Kaipio J, Somersalo E. Statistical and computational inverse problems. vol. 160. Springer Science & Business Media; 2006.
28. Knupp DC, da Silva LG, Belivacqua L, Galeão AC, Silva Neto AJ. Inverse analysis of a new anomalous diffusion model employing maximum likelihood and bayesian estimation. *Mathematical Modeling and Computational Intelligence in Engineering Applications*. 2016:89-104.
29. Danes F, Garnier B, Dupuis T. Predicting, measuring, and tailoring the transverse thermal conductivity of composites from polymer matrix and metal filler. *International Journal of Thermophysics*. 2003;24(3):771-84.
30. Su J, Cerqueira DR, Wang SZ. Thermal design of multi-layered composite pipelines for deep water oil and gas production. *International journal of computer applications in technology*. 2012;43(3):248-59.
31. Sarkar D, Haji-Sheikh A, Jain A. Temperature distribution in multi-layer skin tissue in presence of a tumor. *International Journal of Heat and Mass Transfer*. 2015;91:602-10.
32. Jayaseelan DD, Xin Y, Vandeperre L, Brown P, Lee WE. Development of multi-layered thermal protection system (TPS) for aerospace applications. *Composites Part B: Engineering*. 2015;79:392-405.
33. Abreu LA, Orlande HR, Kaipio J, Kolehmainen V, Cotta R, Quaresma JNN. Identification of contact failures in multilayered composites with the Markov chain Monte Carlo method. *Journal of Heat Transfer*. 2014;136(10).
34. Abreu LA, Colaço MJ, Orlande HR, Alves CJ. Thermography detection of contact failures in double layered materials using the reciprocity functional approach. *Applied Thermal Engineering*. 2016;100:1173-8.
35. Mascouto FS, Knupp DC, Abreu LA, Sanches EL, Sphaier LA. Detection of contact failures employing combination of integral transforms with single-domain formulation, finite differences, and Bayesian inference. *Numerical Heat Transfer, Part A: Applications*. 2020;77(6):599-618.
36. Beck JV, Blackwell B, Clair Jr CRS. *Inverse heat conduction: Ill-posed problems*. John Wiley & Sons; 1985.
37. Kaipio JP, Fox C. The Bayesian framework for inverse problems in heat transfer. *Heat Transfer Engineering*. 2011;32(9):718-53.
38. Orlande HR. Inverse problems in heat transfer: new trends on solution methodologies and applications. *Journal of Heat Transfer*. 2012;134(3).

39. Orlande HRB, Dulikravich GS, Neumayer M, Watzenig D, Colaço MJ. Accelerated Bayesian inference for the estimation of spatially varying heat flux in a heat conduction problem. *Numerical Heat Transfer, Part A: Applications*. 2014;65(1):1-25.
40. Vakili S, Gadala MS. Effectiveness and efficiency of particle swarm optimization technique in inverse heat conduction analysis. *Numerical Heat Transfer, Part B: Fundamentals*. 2009;56(2):119-41.
41. Garcia S, Guynn J, Scott EP. Use of genetic algorithms in thermal property estimation: part II-simultaneous estimation of thermal properties. *Numerical Heat Transfer, Part A Applications*. 1998;33(2):149-68.
42. Imani A, Ranjbar A, Esmkhani M. Simultaneous estimation of temperature-dependent thermal conductivity and heat capacity based on modified genetic algorithm. *Inverse Problems in Science and Engineering*. 2006;14(7):767-83.
43. Soeiro F, Soares PO, Campos Velho H, Silva Neto A. Using neural networks to obtain initial estimates for the solution of inverse heat transfer problems. In: *Inverse Problems, Design an Optimization Symposium*; 2004. p. 358-63.
44. Shiguemori ÉH, Silva JDS, de Campos Velho HF. Estimation of initial condition in heat conduction by neural network. *Inverse Problems in Science and Engineering*. 2004;12(3):317-28.
45. Balaji C, Padhi T. A new ANN driven MCMC method for multi-parameter estimation in two-dimensional conduction with heat generation. *International journal of heat and mass transfer*. 2010;53(23-24):5440-55.
46. Czél B, Woodbury KA, Gróf G. Simultaneous estimation of temperature-dependent volumetric heat capacity and thermal conductivity functions via neural networks. *International Journal of Heat and Mass Transfer*. 2014;68:1-13.
47. Hu C, Duan Y, Liu S, Yan Y, Tao N, Osman A, et al. LSTM-RNN-based defect classification in honeycomb structures using infrared thermography. *Infrared Physics & Technology*. 2019;102:103032.
48. Fang Q, Maldague X. A method of defect depth estimation for simulated infrared thermography data with deep learning. *Applied Sciences*. 2020;10(19):6819.
49. Kaur K, Mulaveesala R, Mishra P. Constrained Autoencoder based Pulse Compressed Thermal Wave Imaging for Sub-surface Defect Detection. *IEEE Sensors Journal*. 2021.
50. Marani R, Palumbo D, Galietti U, D'Orazio T. Deep learning for defect characterization in composite laminates inspected by step-heating thermography. *Optics and Lasers in Engineering*. 2021;145:106679.

51. Xu L, Hu J. A Method of Defect Depth Recognition in Active Infrared Thermography Based on GRU Networks. *Applied Sciences*. 2021;11(14):6387.
52. Hinton GE, Salakhutdinov RR. Reducing the dimensionality of data with neural networks. *science*. 2006;313(5786):504-7.
53. Jardim LCSJ, Knupp DC, Domingos RP, Abreu LAS, Corona CC, Silva Neto AJ. Contact Failure Identification in Multilayered Media via Artificial Neural Networks and Autoencoders. *Anais da Academia Brasileira de Ciências*. 2022;94.
54. Knupp DC, Naveira-Cotta CP, Orlande HR, Cotta RM. Experimental identification of thermophysical properties in heterogeneous materials with integral transformation of temperature measurements from infrared thermography. *Experimental Heat Transfer*. 2013;26(1):1-25.
55. de Queiroz Mendes R, Ribeiro EG, dos Santos Rosa N, Grassi Jr V. On deep learning techniques to boost monocular depth estimation for autonomous navigation. *Robotics and Autonomous Systems*. 2021;136:103701.
56. Chollet F. *Deep learning with Python*. New York, NY: Manning Publications; 2017.
57. Sacadura JF. Radiative heat transfer in fire safety science. *Journal of Quantitative Spectroscopy and Radiative Transfer*. 2005;93(1-3):5-24.
58. Baillis D, Sacadura JF. Thermal radiation properties of dispersed media: theoretical prediction and experimental characterization. In: *Radiative Transfer II. Proceedings of the Second International Symposium on Radiation Transfer*. Begel House Inc.; 1997. .
59. Baillis D, Raynaud M, Sacadura J. Spectral radiative properties of open-cell foam insulation. *Journal of thermophysics and heat transfer*. 1999;13(3):292-8.
60. Zhang K, Li W, Eide H, Stamnes K. A bio-optical model suitable for use in forward and inverse coupled atmosphere–ocean radiative transfer models. *Journal of Quantitative Spectroscopy and Radiative Transfer*. 2007;103(2):411-23.
61. Bate MR, Keto ER. Combining radiative transfer and diffuse interstellar medium physics to model star formation. *Monthly Notices of the Royal Astronomical Society*. 2015;449(3):2643-67.
62. Mohan S, Saxena A, Singh S. Heat loss analysis from a trapezoidal cavity receiver in LFR system using conduction-radiation model. *Solar Energy*. 2018;159:37-43.
63. Sukumar S, Kar SP. A combined conduction–radiation model for analyzing the role of radiation on freezing of a biological tissue. *Journal of Thermal Science and Engineering Applications*. 2020;12(1).

64. Kaemmerlen A, Asllanaj F, Sallée H, Baillis D, Jeandel G. Transient modeling of combined conduction and radiation in wood fibre insulation and comparison with experimental data. *International Journal of Thermal Sciences*. 2010;49(11):2169-76.
65. Baillis D, Sacadura JFo. Directional spectral emittance of a packed bed: influence of the temperature gradient in the medium. *J Heat Transfer*. 2002;124(5):904-11.
66. Sacadura JF, Al Abed A. A Monte Carlo-finite difference method for coupled radiation-conduction heat transfer in semitransparent media. *ASME Journal of Heat Transfer*. 1983;105:931-3.
67. Ruperti J N J, Raynaud M, Sacadura JF. A Method for the Solution of the Coupled Inverse Heat Conduction-Radiation Problem. *Journal of Heat Transfer*. 1996;118(1):10-7.
68. Li H. Estimation of thermal properties in combined conduction and radiation. *International Journal of Heat and Mass Transfer*. 1999;42(3):565-72.
69. Verma S, Balaji C. Multi-parameter estimation in combined conduction–radiation from a plane parallel participating medium using genetic algorithms. *International Journal of Heat and Mass Transfer*. 2007;50(9-10):1706-14.
70. Lobato F, Steffen V, Silva Neto AJ. Solution of the coupled inverse conduction-radiation problem using multi-objective optimization differential evolution. In: 8th World Congress on Structural and Multidisciplinary Optimization, Lisbon, Portugal; 2009. .
71. Lobato F, Steffen Jr V, Neto AS. Estimation of space-dependent single scattering albedo in a radiative transfer problem using differential evolution. *Inverse Problems in Science and Engineering*. 2012;20(7):1043-55.
72. Stephany S, Becceneri J, Souto R, de Campos Velho H, Neto AS. A pre-regularization scheme for the reconstruction of a spatial dependent scattering albedo using a hybrid ant colony optimization implementation. *Applied Mathematical Modelling*. 2010;34(3):561-72.
73. Levenberg K. A method for the solution of certain non-linear problems in least squares. *Quarterly of Applied Mathematics*. 1944;2(2):164-8.
74. Marquardt DW. An algorithm for least-squares estimation of nonlinear parameters. *Journal of the Society for Industrial and Applied Mathematics*. 1963;11(2):431-41.
75. Sajedi R, Faraji J, Kowsary F. A new damping strategy of Levenberg-Marquardt algorithm with a fuzzy method for inverse heat transfer problem parameter estimation. *International Communications in Heat and Mass Transfer*. 2021;126:105433.

76. Tikhonov AN. On the solution of ill-posed problems and the method of regularization. In: Doklady Akademii Nauk. vol. 151. Russian Academy of Sciences; 1963. p. 501-4.
77. Özışık MN. Radiative Transfer and Interactions with Conduction and Convection. New York NY: John Wiley & Sons Inc; 1973.
78. Chandrasekhar S. Radiative transfer. New York, NY: Dover Publications; 1960.
79. Knupp DC, Silva Neto AJ, Sacco WF. Radiative properties estimation with the Particle Collision Algorithm based on a sensitivity analysis. High Temperatures–High Pressures. 2009;38(2).
80. Wolfram Documentation Center;. Accessed: July 11th, 2020. <https://reference.wolfram.com/>.
81. Knupp DC, Canato JVM, Silva Neto AJ, Soeiro FJ. Radiative Properties Estimation and Construction of Confidence Regions with a Combination of the Differential Evolution Algorithm and the Likelihood Method. Proceeding Series of the Brazilian Society of Computational and Applied Mathematics. 2017;5(1).
82. Hansen PC. Analysis of discrete ill-posed problems by means of the L-curve. SIAM review. 1992;34(4):561-80.
83. Hansen PC, O’Leary DP. The use of the L-curve in the regularization of discrete ill-posed problems. SIAM journal on scientific computing. 1993;14(6):1487-503.
84. Bazán FSV. Fixed-point iterations in determining the Tikhonov regularization parameter. Inverse Problems. 2008;24(3):035001.
85. Morozov VA. Methods for solving incorrectly posed problems. Springer Science & Business Media; 2012.
86. Doicu A, Schreier F, Hess M. Iteratively regularized Gauss–Newton method for atmospheric remote sensing. Computer physics communications. 2002;148(2):214-26.
87. Alifanov OM. Inverse Heat Transfer Problems. Springer Science & Business Media; 2012.
88. Moura Neto FD, Silva Neto AJ. An Introduction to Inverse Problems with Applications. Springer; 2012.
89. Schoen F. Two-phase methods for global optimization. In: Handbook of global optimization. Springer, Boston, MA; 2002. p. 151-77.

90. Henderson N, de Sá Rêgo M, Sacco WF, Rodrigues Jr RA. A new look at the topographical global optimization method and its application to the phase stability analysis of mixtures. *Chemical Engineering Science*. 2015;127:151-74.
91. Törn AA. Clustering methods in global optimization. In: *Preeprints of the Second IFAC Symposium on Stochastic Control*; 1986. p. 138-43.
92. Juselius C. A topographical method for global optimization. Åbo Akademi; 1989.
93. Törn AA. *Topographical Global Optimization*. Finland: Åbo Akademi; 1990.
94. Törn A, Viitanen S. Topographical global optimization. In: Floudas CA, Pardalos PM, editors. *Recent advances in global optimization*. Princeton University Press Princeton, NJ; 1992. p. 384-98.
95. Törn A, Viitanen S. Topographical global optimization using pre-sampled points. *Journal of Global Optimization*. 1994;5(3):267-76.
96. Sacco WF, Henderson N, Rios-Coelho AC. Topographical Global Optimization applied to nuclear reactor core design: Some preliminary results. *Annals of Nuclear Energy*. 2014;65:166-73.
97. Ferreira MP, Rocha ML, Silva Neto AJ, Sacco WF. A constrained ITGO heuristic applied to engineering optimization. *Expert Systems with Applications*. 2018;110:106-24.
98. Jardim LCS, Knupp DC, Silva Neto AJ, Sacco WF. Estimation Of Thermal Properties Using The Sobol Sequence And Mersenne Twister With The Topographical Global Optimization. In: *17th Brazilian Congress of Thermal Sciences and Engineering*. Águas de Lindoia, SP; 2018. .
99. Matsumoto M, Nishimura T. Mersenne twister: a 623-dimensionally equidistributed uniform pseudo-random number generator. *ACM Transactions on Modeling and Computer Simulation (TOMACS)*. 1998;8(1):3-30.
100. Sobol IM. On the distribution of points in a cube and the approximate evaluation of integrals. *Zhurnal Vychislitel'noi Matematiki i Matematicheskoi Fiziki*. 1967;7(4):784-802.
101. Nelder JA, Mead R. A simplex method for function minimization. *The Computer Journal*. 1965;7(4):308-13.
102. Törn A, Viitanen S. Iterative Topographical Global Optimization. In: *State of the art in global optimization*. Springer; 1996. p. 353-63.

103. Matsumoto M. Mersenne Twister Home Page; 2011. Accessed: July 11th, 2020. <http://www.math.sci.hiroshima-u.ac.jp/~m-mat/MT/emt.html>.
104. Joe S, Kuo F. Sobol Sequence Generator; 2010. Accessed: July 11th, 2020. <https://web.maths.unsw.edu.au/~fkuo/sobol/>.
105. Maaranen H, Miettinen K, Mäkelä MM. Quasi-random initial population for genetic algorithms. *Computers & Mathematics with Applications*. 2004;47(12):1885-95.
106. Jr EP. Mersenne Twister and Friends; 2011. Accessed: July 11th, 2020. Wolfram Demonstrations Project, <https://demonstrations.wolfram.com/MersenneTwisterAndFriends/>.
107. Lagarias JC, Reeds JA, Wright MH, Wright PE. Convergence properties of the Nelder–Mead simplex method in low dimensions. *SIAM Journal on optimization*. 1998;9(1):112-47.
108. Brent R. Algorithms for minimization without derivatives. New Jersey: Prentice-Hall; 1973.
109. Sacco WF, Alves Filho H, Henderson N, de Oliveira CR. A Metropolis algorithm combined with Nelder–Mead Simplex applied to nuclear reactor core design. *Annals of Nuclear Energy*. 2008;35(5):861-7.
110. Sacco WF, Rios-Coelho AC, Henderson N. Testing population initialisation schemes for differential evolution applied to a nuclear reactor core design. *International Journal of Nuclear Energy Science and Technology*. 2014;8(3):192-212.
111. Sharma N, Arun N, Ravi V. An ant colony optimisation and Nelder–Mead simplex hybrid algorithm for training neural networks: an application to bankruptcy prediction in banks. *International Journal of Information and Decision Sciences*. 2013;5(2):188-203.
112. Dréo J, Siarry P. An ant colony algorithm aimed at dynamic continuous optimization. *Applied Mathematics and Computation*. 2006;181(1):457-67.
113. Mehta V. Improved Nelder–Mead algorithm in high dimensions with adaptive parameters based on Chebyshev spacing points. *Engineering Optimization*. 2020;52(10):1814-28.
114. Kitaoka H, Amano Ki, Nishi N, Sakka T. Improvement of the Nelder-Mead method using Direct Inversion in Iterative Subspace. *Optimization and Engineering*. 2021:1-23.
115. Singh PR, Abd Elaziz M, Xiong S. Modified Spider Monkey Optimization based on Nelder–Mead method for global optimization. *Expert Systems with Applications*. 2018;110:264-89.

116. Wörz S, Mederle M, Heizinger V, Bernhardt H. A novel approach to piecewise analytic agricultural machinery path reconstruction. *Engineering Optimization*. 2017;49(12):2150-73.
117. Reddy RS, Arepally D, Datta AK. Estimation of heat flux in bread baking by inverse problem. *Journal of Food Engineering*. 2020;271:109774.
118. Azadeh A, Ghaderi SF, Sheikhalishahi M, Nokhandan BP. Optimization of short load forecasting in electricity market of Iran using artificial neural networks. *Optimization and Engineering*. 2014;15(2):485-508.
119. Sudiharto I, Anggriawan DO, Tjahjono A. Harmonic Load Identification Based on Fast Fourier Transform and Levenberg Marquardt Backpropagation. *Journal of Theoretical and Applied Information Technology*. 2017;95(5):1080.
120. Ye Z, Kim MK. Predicting electricity consumption in a building using an optimized back-propagation and Levenberg–Marquardt back-propagation neural network: Case study of a shopping mall in China. *Sustainable Cities and Society*. 2018;42:176-83.
121. Kumar A, Kumar R. Least square fitting for adaptive wavelet generation and automatic prediction of defect size in the bearing using Levenberg–Marquardt back-propagation. *Journal of Nondestructive Evaluation*. 2017;36(1):7.
122. Raghu S, Sriraam N. Optimal configuration of multilayer perceptron neural network classifier for recognition of intracranial epileptic seizures. *Expert Systems With Applications*. 2017;89:205-21.
123. Bejan A. *Convection Heat Transfer*. New Jersey: John wiley & sons; 2013.
124. Shah R, London A. *Laminar flow forced convection in ducts*. New York: Academic Press; 1978.
125. Bokar JC, Özisik MN. An inverse analysis for estimating the time-varying inlet temperature in laminar flow inside a parallel plate duct. *International Journal of Heat and Mass Transfer*. 1995;38(1):39-45.
126. Lobato F, Steffen V, Silva Neto AJ. Solution of the coupled inverse conduction-radiation problem using multi-objective optimization differential evolution. In: *8th World Congress on Structural and Multidisciplinary Optimization*, Lisbon, Portugal; 2009. .
127. Lienhard JH IV, Lienhard JH V. *A Heat Transfer Textbook*. 5th ed. Cambridge, MA: Phlogiston Press; 2019. Available from: <http://ahtt.mit.edu>.
128. Liu F, Özişik MN. Estimation of inlet temperature profile in laminar duct flow. *Inverse Problems in Engineering*. 1996;3(1-3):131-43.

129. Wilcoxon F. Individual Comparisons by Ranking Methods. *Biometrics Bulletin*. 1945;1(6):80-3.
130. Derrac J, García S, Molina D, Herrera F. A practical tutorial on the use of non-parametric statistical tests as a methodology for comparing evolutionary and swarm intelligence algorithms. *Swarm and Evolutionary Computation*. 2011;1(1):3-18.
131. McDonald JH. *Handbook of biological statistics*. vol. 2. Sparky House Publishing Baltimore, MD; 2009.
132. McCornack RL. Extended tables of the Wilcoxon matched pair signed rank statistic. *Journal of the American Statistical Association*. 1965;60(311):864-71.
133. Neto FDM, Silva Neto AJ. Two equivalent approaches to obtain the gradient in algorithms for function estimation in heat conduction problems. In: 2000 National Heat Transfer Conference, Pittsburgh, PA. Pittsburgh, PA; 2000. .
134. Wang J, Neto AJS, Neto FDM, Su J. Function estimation with Alifanov's iterative regularization method in linear and nonlinear heat conduction problems. *Applied Mathematical Modelling*. 2002;26(11):1093-111.
135. Hansen PC. *Rank-deficient and discrete ill-posed problems: numerical aspects of linear inversion*. Philadelphia: SIAM; 1998.
136. Bozzoli F, Cattani L, Rainieri S, Bazán FSV, Borges LS. Estimation of the local heat-transfer coefficient in the laminar flow regime in coiled tubes by the Tikhonov regularisation method. *International Journal of Heat and Mass Transfer*. 2014;72:352-61.
137. Aucejo M, De Smet O. A generalized multiplicative regularization for input estimation. *Mechanical Systems and Signal Processing*. 2021;157:107637.
138. Pennes HH. Analysis of tissue and arterial blood temperatures in the resting human forearm. *Journal of applied physiology*. 1948;1(2):93-122.
139. Khanday M, Nazir K. Mathematical and numerical analysis of thermal distribution in cancerous tissues under the local heat therapy. *International Journal of Biomathematics*. 2017;10(07):1750099.
140. Mellal I, Oukaira A, Kengene E, Lakhssassi A. Thermal therapy modalities for cancer treatment: A review and future perspectives. *Appl Sci Res Rev*. 2017;4(02):1-11.
141. Schena E, Saccomandi P, Fong Y. Laser ablation for cancer: past, present and future. *Journal of functional biomaterials*. 2017;8(2):19.

142. Elwassif MM, Kong Q, Vazquez M, Bikson M. Bio-heat transfer model of deep brain stimulation-induced temperature changes. *Journal of neural engineering*. 2006;3(4):306.
143. Cotta RM, Cotta BP, Naveira-Cotta CP, Cotta-Pereira G. Hybrid integral transforms analysis of the bioheat equation with variable properties. *International journal of thermal sciences*. 2010;49(9):1510-6.
144. Kengne E, Lakhssassi A, Vaillancourt R. Temperature distributions for regional hypothermia based on nonlinear bioheat equation of Pennes type: dermis and subcutaneous tissues. 2012.
145. Ng E, Tan H, Ooi E. Boundary element method with bioheat equation for skin burn injury. *Burns*. 2009;35(7):987-97.
146. Özen Ş, Helhel S, Cerezci O. Heat analysis of biological tissue exposed to microwave by using thermal wave model of bio-heat transfer (TWMBT). *Burns*. 2008;34(1):45-9.
147. Knupp D, Neto AS. Solution of the inverse radiative transfer problem of simultaneous identification of the optical thickness and space-dependent Albedo using Bayesian inference. *Comput Model Eng Sci*. 2013;96:339-60.
148. Knupp D, Silva Neto AJ, Sacco W. Radiative properties estimation with the luus-jaakola and the particle collision algorithm. *Computer Modeling in Engineering and Sciences (CMES)*. 2009;54(2):121.
149. Soares PO, Silva Neto AJ, de Campos Velho HF, Soeiro FJdCP. A two step inverse problem for vertical temperature profile retrieval in cloudy atmosphere using artificial neural networks. In: *Proceedings of the 22nd International Congress of Mechanical Engineering (COBEM 2013)*. Ribeirão Preto, Brazil; 2013. p. 4364-75.
150. Neto AS, Özişik M. An inverse problem of simultaneous estimation of radiation phase function, albedo and optical thickness. *Journal of Quantitative Spectroscopy and Radiative Transfer*. 1995;53(4):397-409.
151. Chalhoub E, Velho HC. Estimation of the optical properties of seawater from measurements of exit radiance. *Journal of Quantitative Spectroscopy and Radiative Transfer*. 2002;72(5):551-65.
152. Horvath H, Alados Arboledas L, Olmo F, Jovanović O, Gangl M, Kaller W, et al. Optical characteristics of the aerosol in Spain and Austria and its effect on radiative forcing. *Journal of Geophysical Research: Atmospheres*. 2002;107(D19):AAC-9.
153. Beck JV, Arnold KJ. *Parameter estimation in engineering and science*. New York, NY: John Wiley and Sons; 1977.

154. Benning M, Burger M. Modern regularization methods for inverse problems. *Acta Numerica*. 2018;27:1-111.
155. Shah R, London A. *Laminar flow forced convection in ducts*. vol. 1. Elsevier; 1978.
156. Silva Neto CA, Silva Neto AJ. Estimation of optical thickness, single scattering albedo and diffuse reflectivities with a minimization algorithm based on an interior points method. In: *Proceedings of 17th International Congress of Mechanical Engineering, ABCM*. São Paulo, Brazil; 2003. .
157. Jiang S, Ma N, Li H, Zhang X. Effects of thermal properties and geometrical dimensions on skin burn injuries. *Burns*. 2002;28(8):713-7.
158. Ke H, Tai S, Wang LV. Photoacoustic thermography of tissue. *Journal of biomedical optics*. 2014;19(2):026003.
159. Momenroodaki P, Haines W, Fromandi M, Popovic Z. Noninvasive internal body temperature tracking with near-field microwave radiometry. *IEEE Transactions on Microwave Theory and Techniques*. 2017;66(5):2535-45.
160. Jardim LCS, Knupp DC, Souza Monteiro Barros TM, Silva Abreu LA, Corona CC, Silva Neto AJ. Computational Intelligence and Tikhonov Regularization with Reduced Dimension Model: Applications in Health, Renewable Energy and Climate Heat Transfer Inverse Problems. In: *Computational Intelligence Methodologies Applied to Sustainable Development Goals*. Springer; 2022. p. 109-29.
161. Pradere C, Joanicot M, Batsale JC, Toutain J, Gourdon C. Processing of temperature field in chemical microreactors with infrared thermography. *Quantitative InfraRed Thermography Journal*. 2006;3(1):117-35.
162. Obeso JA, Olanow CW, Rodriguez-Oroz MC, P K, Kumar R, Lang AE. Deep-brain stimulation of the subthalamic nucleus or the pars interna of the globus pallidus in Parkinson's disease. *New England Journal of Medicine*. 2001;345(13):956-63.
163. Vidailhet M, Vercueil L, Houeto JL, Krystkowiak P, Benabid AL, Cornu P, et al. Bilateral deep-brain stimulation of the globus pallidus in primary generalized dystonia. *New England Journal of Medicine*. 2005;352(5):459-67.
164. Hodaie M, Wennberg RA, Dostrovsky JO, Lozano AM. Chronic anterior thalamus stimulation for intractable epilepsy. *Epilepsia*. 2002;43(6):603-8.
165. Kringelbach ML, Jenkinson N, Owen SL, Aziz TZ. Translational principles of deep brain stimulation. *Nature Reviews Neuroscience*. 2007;8(8):603-8.
166. Coffey RJ. Deep brain stimulation devices: a brief technical history and review. *Artificial Organs*. 2009;33(3):208-20.

167. Jardim LCS, Silva Abreu LA, Knupp DC, Silva Neto AJ. Brain Thermal And Electrical Properties Estimation Using Experimental Data From Deep Brain Stimulation Lead. *Revista Mundi Engenharia, Tecnologia e Gestão* (ISSN: 2525-4782). 2020;5(6).
168. Ashkan K, Rogers P, Bergman H, Ughratdar I. Insights into the mechanisms of deep brain stimulation. *Nature Reviews Neurology*. 2017;13(9):548.
169. Elwassif MM, Datta A, Rahman A, Bikson M. Temperature control at DBS electrodes using a heat sink: experimentally validated FEM model of DBS lead architecture. *Journal of Neural Engineering*. 2012;9(4).
170. Patterson T, Mark MS, Brett LN. Mechanisms of electrode induced injury. Part 2: clinical experience. *American Journal of Electroneurodiagnostic Technology*. 2007;47(2):93-113.
171. Medtronic, Inc. DBS Lead Kit for Deep Brain Stimulation, Model 3387/3389, Implant Manual. Minneapolis, MN, US; 2002.
172. Perl W. Heat and matter distribution in body tissues and the determination of tissue blood flow by local clearance methods. *Journal of Theoretical Biology*. 1962;2(3):201-35.
173. Wolfram S. *The Mathematica Book*. Cambridge: Wolfram Media; 2005.
174. Schwaab M, Biscaia JEC, Monteiro JL, Pinto J. Nonlinear parameter estimation through particle swarm optimization. *Chemical Engineering Science*. 2008;63(6):375-95.

APPENDIX - Works produced from this thesis

Journals:

- JARDIM, L. C.S.; KNUPP, D. C.; DOMINGOS, R. P.; ABREU, L. A. S.; CORONA, C. C.; SILVA NETO, A. J.: Contact Failure Identification in Multilayered Media via Artificial Neural Networks and Autoencoders. *Anais Da Academia Brasileira De Ciências*, v. 94, p. e20211577, 2022.
- JARDIM, L. C. S.; ABREU, L. A. S.; Knupp, D. C.; SILVA NETO, A. J.: Brain Thermal And Electrical Properties Estimation Using Experimental Data From Deep Brain Stimulation Lead. *Revista Mundi Engenharia, Tecnologia E Gestão*, v. 5, p. 291-01-291-15, 2020.
- JARDIM, L. C. S.; KNUPP, D. C.; PELTA, D. A.; CORONA, C. C.; LLANES-SANTIAGO, O.; SILVA NETO, A. J.: Fuzzy Levenberg-Marquardt damping factor update strategy and Tikhonov regularization applied to a coupled conduction-radiation inverse heat transfer problem. *High Temperatures-High Pressures*, Vol. 52, pp. 1–22, 2023. Accepted for publication.

Book chapters:

- JARDIM, L. C. S.; KNUPP, D. C.; BARROS, T. M. S. M.; ABREU, LUIZ A. S.; CORONA, C. C.; SILVA NETO, A. J.: Computational Intelligence and Tikhonov Regularization with Reduced Dimension Model: Applications in Health, Renewable Energy and Climate Heat Transfer Inverse Problems. In: Verdegay, J.L., Brito, J., Cruz, C.. (Org.). *Computational Intelligence Methodologies Applied to Sustainable Development Goals*. Studies in Computational Intelligence. 1ed.: Springer, Cham, 2022, v. 1036, p. 109-129.
- JARDIM, L. C. S.; KNUPP, D. C.; Sacco, W. F.; SILVA NETO, A. J.: Solution of a Coupled Conduction-Radiation Inverse Heat Transfer Problem with the Topographical Global Optimization Method. In: Orestes Llanes Santiago; Carlos Cruz Corona; Antônio José Silva Neto; José Luis Verdegay. (Org.). *Studies in Computational Intelligence*. 1ed.: Springer International Publishing, 2020, v. 872, p. 53-71.

Conference papers:

- JARDIM, L. C. S.; KNUPP, D. C.; PELTA, D. A.; CORONA, C. C.; SILVA NETO, A. J.: Levenberg-Marquardt Damping Factor Fuzzy Updating Strategy: An Illustrative Example. In: XXI Congreso de Tecnologías y Lógica Fuzzy (ESTYLF-22), 2022, Toledo/ES. Actas del XXI Congreso de Tecnologías y Lógica Fuzzy (ESTYLF-22), 2022. p. 135-136.
- JARDIM, L. C. S.; KNUPP, D. C.; CORONA, C. C.; SILVA NETO, A.J.: Estimation of the Optimal Tikhonov Regularization Parameter using Reduced Dimension Model. In: XXIII Encontro Nacional de Modelagem Computacional e XI Encontro de Ciência e Tecnologia de Materiais, 2020, Palmas, Tocantins. Anais do XXIII Encontro Nacional de Modelagem Computacional e XI Encontro de Ciência e Tecnologia de Materiais. Palmas, TO: ESMAT, 2020.
- JARDIM, L. C. S.; ABREU, L.A.S.; KNUPP, D. C.; SILVA NETO, A.J.: Brain Thermal and Electrical Properties Estimation Using Experimental Data From Deep Brain Stimulation Lead. In: XXII Encontro Nacional de Modelagem Computacional, 2019, Juiz de Fora - MG. XXII Encontro Nacional de Modelagem Computacional e X Encontro de Ciência e Tecnologia de Materiais, 2019.